Field-free Control of Magnetism in Nanostructured Materials Probed with High Resolution X-ray Microscopy

Dissertation
zur Erlangung des Grades
Doktor der Naturwissenschaften (Dr. rer. nat.)
am Fachbereich Physik
der Johannes Gutenberg-Universität Mainz

von:
Simone Finizio
geboren in Milano (Italien)
Mainz, 2015

Simone Finizio

Field-free Control of Magnetism in Nanostructured Materials Probed with High Resolution X-ray Microscopy

1. Berichterstatter: Aus Datenschutzgründen entfernt / Removed due to data privacy
2. Berichterstatter: Aus Datenschutzgründen entfernt / Removed due to data privacy
Datum der mündlichen Prüfung: 20. Juli, 2015

Johannes Gutenberg-Universität Mainz
AG Kläui
Institut für Physik
Staudingerweg 7
55128, Mainz

Contents

List of Figures

List of Tables

List of Acronyms

AMR	Anisotropic Magneto-Resistance
CA	Contrast Aperture
CCD	Charge Coupled Device
CMG	Co_2MnGa
DAC	Digital Analog Converter
DC	Direct Current
DW	Domain Wall
EBL	Electron Beam Lithography
EA	Easy Axis
ES	Exit Slit
FCS	Fe_2CrSi
FIB	Focused Ion Beam
f.u.	Formula Unit
GMR	Giant Magneto-Resistance
HV	High Voltage
ID	Insertion Device
IT	Information Technology
LEEM	Low-Energy Electron Microscope
LINAC	Linear Accelerator
LLG	Landau-Lifschitz-Gilbert
LSMO	$La_{0.7}Sr_{0.3}MnO_3$
MIT	Metal-Insulator Transition
MMA	Methyl-Methacrylate
MOKE	Magneto-Optic Kerr Effect
PEEM	Photoemission Electron Microscope
PMMA	Poly(Methyl-Methacrylate)
PMN-PT	$[Pb(Mg_{0.33}Nb_{0.66})O_3]_{(1-x)}$-$[PbTiO_3]_x$
Py	Permalloy (Ni-Fe alloy)

RF	Radio-Frequency
RHEED	Reflection High-Energy Electron Diffraction
SEM	Scanning Electron Microscope
SQUID	Superconducting Quantum Interference Device
STO	$SrTiO_3$
TW	Transverse Wall
UART	Universal Asynchronous Receiver/Transmitter
UV	Ultra-Violet
VC	Vortex Core
VW	Vortex Wall
XMCD	X-ray Magnetic Circular Dichroism
XRD	X-ray Diffraction

Abstract

Magnetic memories are a backbone of today's digital data storage technology, where the digital information is stored as the magnetic configuration of nanostructured ferromagnetic bits. Currently, the writing of the digital information on the magnetic memory is carried out with the help of magnetic fields. This approach, while viable, is not optimal due to its intrinsically high energy consumption and relatively poor scalability. For this reason, the research for different mechanisms that can be used to manipulate the magnetic configuration of a material is of interest. In this thesis, the control of the magnetization of different nanostructured materials with field-free mechanisms is investigated. The magnetic configuration of these nanostructured materials was imaged directly with high resolution x-ray magnetic microscopy.

First of all, the control of the magnetic configuration of nanostructured ferromagnetic Heusler compounds by fabricating nanostructures with different geometries was analyzed. Here, it was observed that the magnetic configuration of the nanostructured elements is given by the competition of magneto-crystalline and shape anisotropy. By fabricating elements with different geometries, we could alter the point where these two effects equilibrate, allowing for the possibility to tailor the magnetic configuration of these nanostructured elements to the required necessities.

Then, the control of the magnetic configuration of Ni nanostructures fabricated on top of a piezoelectric material with the magneto-elastic effect (i.e. by applying a piezoelectric strain to the Ni nanostructures) was investigated. Here, the magneto-elastic coupling effect gives rise to an additional anisotropy contribution, proportional to the strain applied to the magnetic material. For this system, a reproducible and reversible control of the magnetic configuration of the nanostructured Ni elements with the application of an electric field across the piezoelectric material was achieved.

Finally, the control of the magnetic configuration of $La_{0.7}Sr_{0.3}MnO_3$ (LSMO) nanostructures with spin-polarized currents was studied. Here, the spin-transfer torque effect was employed to achieve the displacement of magnetic domain walls in the LSMO nanostructures. A high spin-transfer torque efficiency was observed for LSMO at low temperatures, and a Joule-heating induced hopping of the magnetic domain walls was observed at room temperatures, allowing for the analysis of the energetics of the domain walls in LSMO.

The results presented in this thesis give thus an overview on the different field-free approaches that can be used to manipulate and tailor the magnetization configuration of a nanostructured material to the various technological requirements, opening up novel interesting possibilities for these materials.

Kurzfassung

Magnetische Speicher sind wichtige Bausteine für die heutige Informationstechnologie aufgrund der Möglichkeit, die digitale Information als Zustand der Magnetisierung eines nanostrukturierten ferromagnetischen Materials permanent zu speichern. In der aktuellen magnetischen Speichertechnologie erfolgt das Schreiben des Magnetisierungszustands durch magnetische Felder, was wegen seines hohen Energiebedarf und der begrenzten Skalierbarkeit weiterer Optimierung bedarf. Die Untersuchung neuer Methoden, welche die Kontrolle der Magnetisierung ohne magnetische Felder ermöglichen, und daher eine aussichtsreiche technologische Weiterentwicklung derzeitiger magnetischer Speicher versprechen, ist von großem Interesse.

Diese Arbeit beschäftigt sich mit der Kontrolle der Magnetisierung von nanostrukturierten ferromagnetischen Materialien mittels Methoden ohne Magnetfeld. Die Magnetisierungskonfiguration der nanostrukturierten Ferromagnete wurde durch hochauflösende Röntgenmikroskopie untersucht.

Zuerst wurde die Kontrolle der Magnetisierung in Heusler-Verbindungen durch nanostrukturierte Geometrien untersucht. Bei diesen Versuchen wurde beobachtet, dass der Magnetisierungszustand dieser Legierungen die Folge eines Wettbewerbs zwischen der magnetokristallinen und der Formanisotropie ist. Dies ermöglichte es, durch die gezielte Auswahl der Geometrie der Nanostrukturen den Magnetisierungszustand reproduzierbar zu verändern.

Weiterhin wurde die Kontrolle der Magnetisierung von Nickel-Nanostrukturen durch die magnetoelastische Kopplung analysiert. Hierbei wurden die Nanostrukturen durch eine mechanische Spannung (generiert durch ein piezoelektrisches Substrat) deformiert und die Änderungen der Magnetisierung untersucht. Für diese Materialkombination wurde eine reproduzierbare reversible Kontrolle der Magnetisierung beobachtet.

Als letztes wurde die Möglichkeit untersucht, die Magnetisierung von nanostrukturiertem $La_{0.7}Sr_{0.3}MnO_3$ (LSMO) mittels spin-polarisierten Strömen zu kontrollieren, welches auf dem Prinzip des Spin-Drehimpuls-Übertrags basiert. Für dieses Material und Methodik konnte eine hohe Übertragungseffizienz bei niedrigen Temperaturen und eine dominierende Joule'sche Erwärmung bei Raumtemperatur beobachtet werden. Zusätzlich wurde die Energie der magnetischen Domänwandzustände des LSMO untersucht.

Die Ergebnisse dieser Arbeite zeigen somit einen Überblick der unterschiedlichen Möglichkeiten einer Kontrolle der Magnetisierung ohne Magnetfeld von nanostrukturierten Materialien und eröffnen neue interessante, technologische Möglichkeiten für diese Materialien.

Introduction

Today, a vast majority of the information produced and processed is stored as digital information (i.e. as logical ones or zeros). Physically, the storage of the digital information employs materials defined as *bistable*, which exhibit two (meta-)stable states, both accessible and distinguishable from each other. Digital information is conventionally stored in either short-term or long-term memories. The short term memories commonly found in modern computing devices store the digital information as the charge state of capacitive cells (i.e. if charge is stored on the capacitor, the cell has stored a digital 1, and vice versa). On the other hand, long term memories typically function based on the magnetic configuration of ferromagnetic materials to store the digital information.

The workhorse of long-term digital data storage is represented by the magnetic hard-disk drive, which consists of a series of disks, on top of which a ferromagnetic material is deposited, where the digital information is stored as the magnetic configuration of small sections, known as *clusters*. The writing of the digital information onto the magnetic configuration of the cluster is conventionally carried out by generating a magnetic field, defined as *Oersted field*, typically fulfilled using an electromagnetic coil [1].

Using the Oersted fields, the magnetic configuration of each single cluster can be manipulated. However, using the Oersted fields is not the most efficient approach for manipulating the magnetization, as the injection of electrical currents across a magnetic coil generates, through resistive losses, a heating in the device. Tackling the resistive losses, which constitute a substantial contribution to the energy balance of IT devices, has been a major concern in the IT industry [2]. Therefore, the research on new functional materials or a combination of materials where it is possible to manipulate the magnetization without the need to apply an Oersted field (i.e. a *field-free control* of the magnetization) is currently of interest.

This thesis gives an insight on different concepts that can be utilized to manipulate the magnetization configuration of a material without the use of power-consumptive magnetic fields. The results provided in this thesis analyze the role that the different contributions to the magnetic free energy exert on the magnetic configuration of a material, and on how these single contributions to the magnetic free energy can be used to control the magnetization configuration of a material without the application of a magnetic field. The studies presented in

this thesis were concentrated on nanostructured materials, as these systems constitute a point of interest both for understanding how the confinement of the magnetization to nanometer sized structures affects the magnetic free energy, and as those structures are of deep interest for applications in micro- and nanoelectronics, where the size of the structures determines important parameters such as the data density of a magnetic memory.

The thesis is organized in the following chapters:

Chapter 1 gives a brief overview of the main theoretical background on magnetism in condensed matter necessary for reading this thesis.

Chapter 2 is an overview of the experimental techniques employed for the fabrication and characterization of the samples described in this work. The main focus is on photoemission electron microscopy employing the x-ray circular dichroism as contrast mechanism, to allow for the determination of the magnetic configuration in nanostructured samples.

Chapter 3 describes the growth and characterization of the magnetic properties of nanostructured elements of Fe_2CrSi and Co_2MnGa ferromagnetic Heusler compound thin films. The response of the magnetic configuration of the Fe_2CrSi and Co_2MnGa thin films is investigated as function of the geometry of the nanostructured elements. It is found that shape and magneto-crystalline anisotropy play an important role in the definition of the magnetic states, and that it is possible to reproducibly and reliably tailor the magnetic configurations of the nanostructured elements by selecting their geometry.

Chapter 4 describes the characterization of an artificial multiferroic system based on the magneto-elastic coupling, where a piezoelectric material is combined with a magnetostrictive material, allowing for the control of the magnetization with the application of an electric field across the piezoelectric material. The response of the magnetic configuration of nanostructured Ni elements to an applied electric was systematically analyzed. To describe the response of the magnetostrictive material, a magneto-static model was introduced and verified with the experimental observations.

Chapter 5 describes the experiments carried out on nanostructured elements of the ferromagnetic oxide $La_{0.7}Sr_{0.3}MnO_3$, where the response of the magnetic configuration upon the injection of a spin-polarized current across the nanostructured element was investigated, in order to study spin-transfer-torque effects onto this material. Low temperature transport measurements concluded that this material exhibits a high spin-transfer-torque efficiency. However, room temperature measurements concluded that Joule heating effects are a critical point for this material, due to the proximity of its Curie temperature to room temperature.

Chapter 6 summarizes the main conclusions of the projects described in this thesis. In addition, also a brief outlook is given, with some proposed further experiments based on the results obtained in this thesis.

Chapter 1

Magnetism in Condensed Matter

This chapter will provide the basic theoretical background necessary for the work of this thesis. In this chapter, a brief description of the microscopic quantum mechanical origin of magnetism will first be given. Secondly, the different contributions to the magnetic free energy (i.e. the thermodynamic function which describes, through its local minima, the stable magnetic configuration of the magnetic system) in the micromagnetic approximation will be introduced and described. Then, the Stoner-Wohlfarth model, used for the description of the magnetic configuration of materials where the magnetization can be described as a "single entity", will be introduced. Finally, the dynamical behavior of the magnetization, and its theoretical description through the Landau-Lifshitz-Gilbert (LLG) equation, will then be introduced.

A detailed description of the microscopic theory of magnetism (both static and dynamic) can be found e.g. in Refs. [3–5].

1.1 Microscopic origin of magnetism

Ferromagnetism is one of the physical phenomena that cannot be described by classical physics as, in a purely classical system, no ferromagnetic order is allowed (i.e. in the absence of a magnetic field, the magnetization of any material should, in the classical description, always relax to zero) [6]. Thus, a quantum mechanical description is necessary, in order to understand the origin behind the magnetic order.

The presence of a ferromagnetic order in a material implies the existence of a long-range interaction between the single magnetic moments of the material, aligning them along a defined direction. This long-range coupling mechanism is caused by the *exchange interaction*, a term which can only be described with a quantum mechanical treatment.

1.1.1 Exchange interaction

For the quantum-mechanical description of the exchange interaction presented in this section Ref. [3] will be followed.

Let us consider a system with two electrons, each of which is quantum mechanically described by a wave function $\psi_i(\mathbf{r}_i)$, where $i = 1, 2$ identifies the "first" and "second" electron respectively. The total system can be described by the wave function $\psi(\mathbf{r}_1, \mathbf{r}_2)$, given by the overlap of the two single-electron wave functions. Given the quantum mechanical requirement for exchange symmetry (i.e. electron "1" is indistinguishable from electron "2" in a quantum mechanical system), and the fermionic nature of the electrons, the wave function $\psi(\mathbf{r}_1, \mathbf{r}_2)$ is given by either of the following relations:

$$\psi_{\mathrm{s}}(\mathbf{r}_1, \mathbf{r}_2) \;=\; \frac{1}{\sqrt{2}} \left[\psi_1(\mathbf{r}_1)\psi_2(\mathbf{r}_2) + \psi_1(\mathbf{r}_2)\psi_2(\mathbf{r}_1)\right] \chi_{\mathrm{s}}, \tag{1.1}$$

$$\psi_{\mathrm{t}}(\mathbf{r}_1, \mathbf{r}_2) \;=\; \frac{1}{\sqrt{2}} \left[\psi_1(\mathbf{r}_1)\psi_2(\mathbf{r}_2) - \psi_1(\mathbf{r}_2)\psi_2(\mathbf{r}_1)\right] \chi_{\mathrm{t}}, \tag{1.2}$$

where $\chi_{\mathrm{s,t}}$ is the spin part of the wave-function, which is antisymmetric with respect to the exchange for the *singlet* (s) and symmetric for the *triplet* (t) states.

The energy of the singlet and triplet states can be determined by calculating the integral $\langle \psi_{\mathrm{s,t}} | \hat{H} | \psi_{\mathrm{s,t}} \rangle$. The difference between the energies of the singlet and triplet states can thus written as follows:

$$2J \;=\; E_{\mathrm{s}} - E_{\mathrm{t}} = 2 \iint \left(\psi_1^*(\mathbf{r}_2)\psi_2^*(\mathbf{r}_1)\right) \hat{H} \left(\psi_1(\mathbf{r}_2)\psi_2(\mathbf{r}_1)\right) \mathrm{d}\mathbf{r}_1 \mathrm{d}\mathbf{r}_2, \tag{1.3}$$

where it was assumed that the spin parts of the wave functions are normalized, and where J is defined as the *exchange integral* (or *exchange constant*).

The Hamiltonian of this two-electron system can also be described, with the definition of the exchange integral given in Eq. (1.3) with the following effective Hamiltonian:

$$\hat{H} \;=\; \frac{1}{4}(E_{\mathrm{s}} + 3E_{\mathrm{t}}) - (E_{\mathrm{s}} - E_{\mathrm{t}})\mathbf{S}_1 \cdot \mathbf{S}_2 \;=\; \frac{1}{4}(E_{\mathrm{s}} + 3E_{\mathrm{t}}) - 2J\mathbf{S}_1 \cdot \mathbf{S}_2 \;=\; \frac{1}{4}(E_{\mathrm{s}} + 3E_{\mathrm{t}}) - \hat{H}_{\mathrm{ex}}, \tag{1.4}$$

where $\mathbf{S}_1$ and $\mathbf{S}_2$ describe the orientation of the spin for the two electrons, and where $\hat{H}_{\mathrm{ex}}$ is defined as the *exchange Hamiltonian* [3].

From Eq. (1.4), if $J > 0$ the triplet state (i.e. parallel spin orientation) is energetically favored. Vice versa, if $J < 0$ the singlet state (i.e. anti-parallel spin orientation) is energetically favored. Thus, the sign of the exchange integral determines if the spins of the two electrons couple *ferromagnetically* (i.e. $J > 0$) or *antiferromagnetically* (i.e. $J < 0$).

The results of this simple two-electron model can be extended to the general case of N electrons, where the following spin-dependent exchange Hamiltonian, known as *Heisenberg Hamiltonian* [3], can be written:

$$\hat{H}_{\mathrm{ex}} \;=\; -\sum_{i,j} J_{i,j} \mathbf{S}_i \cdot \mathbf{S}_j, \tag{1.5}$$

being $J_{i,j}$ the exchange constant between the i-th and j-th electrons (each with a spin $\mathbf{S}_i$ and $\mathbf{S}_j$). Typically, only the exchange constant between neighboring particles is considered.

The Heisenberg Hamiltonian described in Eq. (1.5) is, despite its simplicity, very well-suited for the description of magnetic systems where the single interacting spins are localized in the material, such as e.g. rare-earths magnets (with localized $4f$ electrons) and ionic solids. The specific interactions between the localized magnetic moments are condensed into the exchange constant, which will thus assume a more complicated form with respect to the exchange integral presented in Eq. (1.3).

1.1.2 Double- and super-exchange

Oxidic materials such as Fe_3O_4, CrO_2 and $La_{0.7}Sr_{0.3}MnO_3$ exhibit a ferro- or ferrimagnetic order, and other oxidic materials such as MnO and $LaMnO_3$ exhibit an antiferromagnetic order, even though the magnetic atoms do not occupy nearest-neighbor positions in the crystal. In these materials, the exchange coupling occurs indirectly, i.e. over the non-magnetic oxygen ions, as schematically shown in Fig. 1.1. This effect, known as *super-exchange*, consists in an indirect exchange interaction between magnetic ions mediated by non-magnetic ions [3, 7].

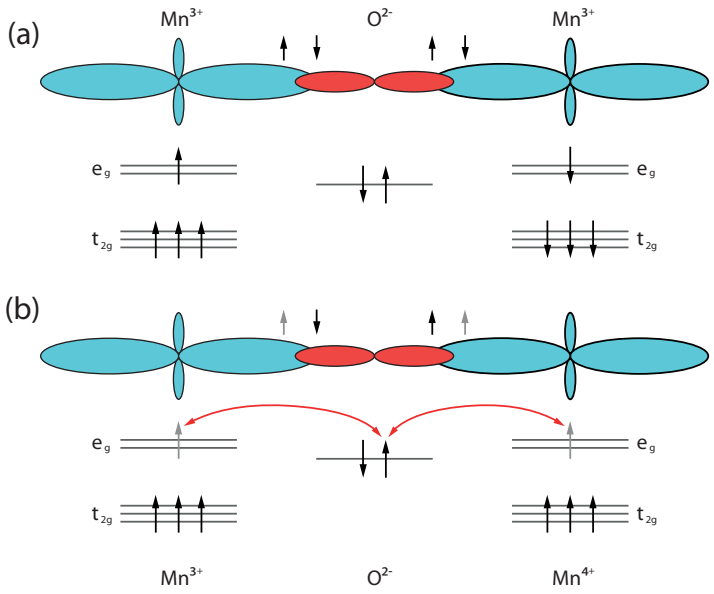

Figure 1.1: Schematic description of the super-exchange mechanism. (a) Antiferromagnetic coupling between two Mn^{3+} ions in $LaMnO_3$ mediated by the electrons in the $2p$ orbital of the O^{2-} ion. (b) Ferromagnetic coupling between Mn^{3+} and Mn^{4+} ions in $La_{0.7}Sr_{0.3}MnO_3$. In this case, the coupling is mediated by the hopping of the electron in the e_g orbital through the O^{2-} ion. As this hopping is spin-conserving, the neighboring Mn ions couple ferromagnetically.

As shown in Fig. 1.1(a), the super-exchange between magnetic ions with the same valence

in the material (in this case, $LaMnO_3$), mediated by the electrons in the $2p$ orbital of the oxygen ions, causes the occurrence of an antiferromagnetic order.

If, as in the case of $La_{0.7}Sr_{0.3}MnO_3$, the magnetic ions exhibit a different valence, as shown in Fig. 1.1(b), the oxygen ions mediate a charge transfer between the magnetic ions (leading, moreover, to a de-localized electron in the Mn-O-Mn group, which also allows one to justify the lower resistivity of $La_{0.7}Sr_{0.3}MnO_3$ with respect to the antiferromagnetic insulator $LaMnO_3$). Such charge transfer, known as *double-exchange* interaction, also favors the generation of a ferromagnetic order in the material [3, 8].

1.1.3 Itinerant ferromagnetism

As mentioned in the previous sections, the Heisenberg Hamiltonian is well-suited for the description of magnetic materials where the single magnetic moments are localized. Such description does not hold, however, for materials such as Fe, Ni and Co, for which a different contribution, caused by the interactions mediated by the itinerant conduction electrons, has to be considered.

In particular, in magnetic metals, the itinerant electrons from the s and p orbitals can interact with the more localized electrons of the d orbitals and mediate an exchange interaction. This interaction can lead to a spin-splitting of the electronic bands of the metal, leading to an asymmetry in the number of electrons with an "up" and "down" spin, which then gives rise to a net magnetic moment $\mathbf{M}$ in the material.

The two possible cases are shown in Fig. 1.2. A non magnetic metal will exhibit no splitting of the two spin sub-bands (Fig. 1.2(a)), while a magnetic metal will exhibit such splitting (Fig. 1.2(b)).

A ferromagnetic ground state mediated by the itinerant electrons in the ferromagnetic metal can be achieved if the difference between the potential and kinetic energies of the electrons at the Fermi energy is positive [3]. By introducing the material-dependent *Stoner parameter* U, an appropriate condition for the achievement of a ferromagnetic ground state is given by $U\rho(E_\mathrm{F}) > 1$, being $\rho(E_\mathrm{F})$ the density of states at the Fermi energy [3, 5]. Materials such as Fe, Ni and Co fulfill this criterion, thus exhibiting a ferromagnetic ground state.

1.2 Thermodynamical description of magnetism

To describe larger magnetic systems, where the atomistic model of magnetization based on the Heisenberg Hamiltonian would become quickly unfeasible due to the large number of electrons, a *micromagnetic* approximation is employed. Under the assumptions of the micromagnetic approximation, the single magnetic moments of the material are replaced with a magnetization function $\mathbf{M}(\mathbf{r})$, which is assumed to be continuous [4, 9].

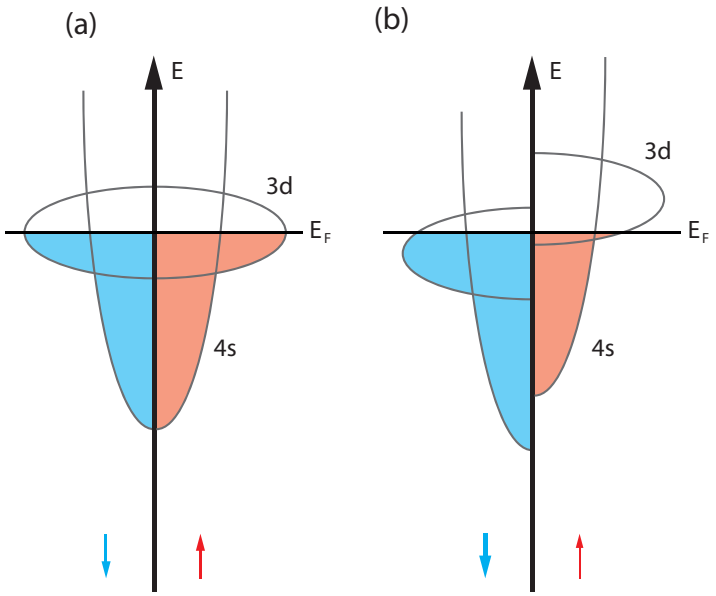

Figure 1.2: (a) Non magnetic metal, exhibiting an equal electronic population in the two spin sub-bands; (b) Ferromagnetic metal, exhibiting an energetic splitting of the two spin sub-bands, leading to a different electronic population of the two spin-sub bands and to a net magnetic moment in the material.

It is possible to give a thermodynamical description of magnetism under micromagnetic approximation by determining the magnetization energy of a magnetic system [3, 9]. The determination of the magnetic free energy (often referred to as *Landau free energy*) allows then for the calculation of the stable configurations of the magnetization by finding its local minima. It is possible to express the magnetic free energy as follows:

$$F = \int_V f(\mathbf{r})\mathrm{d}V = \int_V f_{\mathrm{ex}}(\mathbf{r}) + f_{\mathrm{str}}(\mathbf{r}) + f_{\mathrm{Z}}(\mathbf{r}) + f_{\mathrm{ani}}(\mathbf{r}) + f_{\mathrm{other}}(\mathbf{r})\,\mathrm{d}V, \tag{1.6}$$

where $f(\mathbf{r})$ is the (local) magnetic free energy density, and where $f_{\mathrm{ex}}(\mathbf{r})$ is the contribution to the magnetic free energy density due to the exchange interaction, $f_{\mathrm{str}}(\mathbf{r})$ the one due to the stray field generated by the single magnetic moments in the material, $f_{\mathrm{Z}}(\mathbf{r})$ the one due to external magnetic fields, $f_{\mathrm{ani}}(\mathbf{r})$ the one due to the magnetic anisotropies, and $f_{\mathrm{other}}(\mathbf{r})$ describes other contributions to the magnetic free energy density, such as the one arising from the magneto-elastic coupling. The integration is limited to the volume V of the magnetic material. In the next sections, each one of the terms of Eq. (1.6) will be described in detail.

1.2.1 Exchange energy

The exchange interaction between two adjacent electrons of spin $\mathbf{S}_1$ and $\mathbf{S}_2$ gives rise to an exchange energy of $\hat{H}_{\mathrm{ex}} = -2J\mathbf{S}_1 \cdot \mathbf{S}_2$, as discussed in more detail in section 1.1.1. Under

the micromagnetic approximation, it is possible to calculate the exchange energy between the single spins in the material as an integral over the entire volume of the sample, where the single spins are replaced by the local magnetization $\mathbf{M}(\mathbf{r})$ [3]:

$$F_{\text{ex}} = \frac{A}{M_s^2} \int_V |\nabla M_x(\mathbf{r})|^2 + |\nabla M_y(\mathbf{r})|^2 + |\nabla M_z(\mathbf{r})|^2 \, \mathrm{d}V, \tag{1.7}$$

where $\mathbf{M} = (M_x, M_y, M_z)$, and where the parameters $A \propto J$ and M_s are the *exchange stiffness* and the *saturation magnetization* of the material, respectively.

1.2.2 Stray field energy

The single magnetic moments in the magnetic material generate a dipolar magnetic stray field, which will interact with the other dipoles present in the material, giving rise to a contribution to the magnetic free energy. In the micromagnetic approximation, the stray field generated by a magnetic material can be calculated from the third Maxwell's equation stating, in its differential formulation, that $\nabla \cdot \mathbf{B} = 0$, where the magnetic field $\mathbf{B}$ may be expressed as $\mathbf{B} = \mu_0(\mathbf{H} + \mathbf{M})$. In the absence of external magnetic fields, the magnetic field $\mathbf{H}$ is then given only by the contribution of the stray fields $\mathbf{H}_{\text{str}}$ generated by the dipoles in the magnetic material. Thus, from the third Maxwell's equation, it is possible to write the following:

$$\nabla \cdot \mathbf{H}_{\text{str}} = -\nabla \cdot \mathbf{M}. \tag{1.8}$$

As the stray field $\mathbf{H}_{\text{str}}$ is generated by the magnetic dipoles in the sample, its curl is zero. Thus, it is possible to express Eq. (1.8) in the Poisson form as follows:

$$(\nabla \cdot \mathbf{H}_{\text{str}}) = \nabla^2 U(\mathbf{r}) = -\rho_{\text{M}}(\mathbf{r}) = (-\nabla \cdot \mathbf{M}). \tag{1.9}$$

Thus, it is possible to describe the stray field $\mathbf{H}_{\text{str}}$ as being generated by an effective *magnetic charge density* $\rho_{\text{M}}(\mathbf{r})$ (generated by the magnetic dipoles in the material), which will then interact with the magnetic dipoles, giving rise to the following contribution to the magnetic free energy [4]:

$$F_{\text{str}} = \frac{\mu_0}{2} \int_{\Re^3} |\mathbf{H}_{\text{str}}(\mathbf{r})|^2 \, \mathrm{d}V, \tag{1.10}$$

where a factor 1/2 has been included in the calculation to avoid the double counting of each volume element, and where the integration is calculated across the entire $\Re^3$ space. Given the dependence of the integral on the norm of the stray field vector, the contribution of the stray field to the magnetic free energy density is always of positive sign.

The stray field term is strongly dependent on the geometry of the sample, and it is often referred to as *shape anisotropy*. As an example, thin film magnetic materials will minimize the stray field energy by orienting their magnetization in the plane of the film, giving rise to an in-plane shape anisotropy contribution. This in-plane shape anisotropy term can be understood

with a simple schematic model, shown in Fig. 1.3, where the number (and distance) of the effective "magnetic charges" generating the stray field is minimized when the magnetization is pointing along the surface of the thin film.

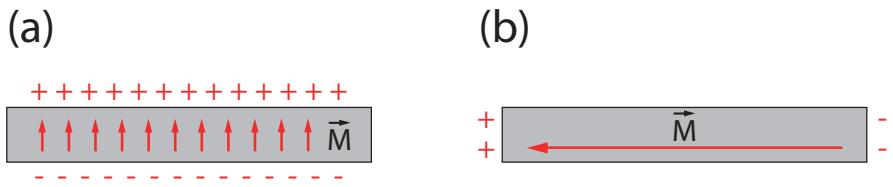

Figure 1.3: Schematic description of the motivation for the in-plane anisotropy of the magnetization in thin film magnetic materials. If the magnetization is pointing out of the plane of the film (a), a large number of magnetic charges is formed at the top and bottom surfaces of the magnetic thin film. Instead, if the magnetization is pointing along the plane of the film (b), magnetic charges form only at the edges of the film. Being the size of the side surfaces much smaller than the top surface, the stray field energy is minimized for the case shown in (b).

1.2.3 Zeeman energy

If an external magnetic field $\mathbf{H}_{\text{ext}}(\mathbf{r})$ is applied to the magnetic material, the local magnetization $\mathbf{M}(\mathbf{r})$ of the material will tend to align itself along the applied magnetic field. This response of the magnetization of the material to an external magnetic field is described by the Zeeman energy, which is written in the following integral form [4]:

$$F_{\text{Z}} = -\mu_0 \int_V \mathbf{H}_{\text{ext}}(\mathbf{r}) \cdot \mathbf{M}(\mathbf{r})\, \mathrm{d}V. \tag{1.11}$$

The Zeeman contribution to the magnetic free energy will be minimum when the local magnetization $\mathbf{M}(\mathbf{r})$ is aligned to the local external magnetic field $\mathbf{H}_{\text{ext}}(\mathbf{r})$ in the entire volume of the magnetic material.

1.2.4 Anisotropy energy

The crystalline structure of the material will also give rise to an influence on its magnetic properties. To describe this influence, an *anisotropy* contribution to the magnetic free energy has to be considered in the magnetic free energy, and such contribution is given by [4]:

$$F_{\text{ani}} = \int_V f_{\text{ani}}(\mathbf{m}(\mathbf{r}))\, \mathrm{d}V, \tag{1.12}$$

where $\mathbf{m} = \frac{\mathbf{M}}{|\mathbf{M}|}$ is the magnetization versor, and where f_{ani} is the energy density term that describes the influence of the crystalline lattice onto the orientation of the magnetization

vector $\mathbf{M}$. Being the Bravais lattice vectors a basis for $\Re^3$, it is possible to express $\mathbf{m}$ as $\mathbf{m} = (m_1, m_2, m_3)$, being $m_i = \cos(\theta_i)$, where θ_i is the angle between $\mathbf{m}$ and the i-th vector of the basis. For simplicity, this description will be limited to the case of a cubic orthonormal basis, but it can be easily extended to the general case.

The position-dependent anisotropy energy term f_{ani} that appears in Eq. (1.12) may be written as follows [4]:

$$f_{\text{ani}} = f_0 + \sum_{i,j} B^{(2)}_{i,j} m_i m_j + \sum_{i,j,k,l} B^{(4)}_{i,j,k,l} m_i m_j m_k m_l + ... \tag{1.13}$$

where $B^{(i)}$ is the i-th order tensor of the anisotropy parameters. Only even order tensors are allowed in the calculation due to the inversion center symmetry of the anisotropy energy (i.e. $f_{\text{ani}}(-\mathbf{m}) = f_{\text{ani}}(\mathbf{m})$).

The materials presented in this thesis exhibit primarily *uniaxial* and *cubic* magneto-crystalline anisotropies. Thus, the discussion will be limited, for simplicity, to these two cases. A uniaxial anisotropy is described, in Eq. (1.13), by the diagonal terms of the $B^{(i)}$ tensors. For example, if the material exhibits a uniaxial anisotropy along the x direction, it is possible to write Eq. (1.13) as follows:

$$f_{\text{ani,u}} = f_0 + B^{(2)}_{11} m_1^2 + B^{(4)}_{1111} m_1^4 + ... = f_0 + K_{1,\text{u}} m_1^2 + K_{2,\text{u}} m_1^4 + ... \tag{1.14}$$

where $K_{i,\text{u}} = B^{(2i)}_{1111}$ was defined as the i-th order uniaxial anisotropy constant. As, typically, the higher orders of the anisotropy constant are neglected, the sign of the first order anisotropy constant $K_{1,\text{u}} = K_{\text{u}}$ determines whether the direction $m_1 = 1$ (i.e. the x axis is defined as the *easy* axis, with a negative anisotropy constant) or $m_1 = 0$ (i.e. the x axis is defined as the *hard* axis, with a positive anisotropy constant) is favored.

To describe a cubic anisotropy, the $B^{(i)}$ tensors of the fourth order and above have to be considered. The calculations will be limited here, for simplicity, to the fourth order of $B^{(i)}$. Moreover, as the materials analyzed in this thesis were fabricated in the thin film form and exhibit an in-plane anisotropy, the calculations here will be limited to the case of an in-plane cubic anisotropy. Under these assumptions, it is possible to describe the anisotropy as follows:

$$f_{\text{ani,c}} = f_0 + (B^{(4)}_{1,1,2,2} + B^{(4)}_{1,2,1,2} + ... + B^{(4)}_{2,2,1,1}) m_1^2 m_2^2 + ... = f_0 + K_{1,\text{c}} m_1^2 m_2^2 + ... \tag{1.15}$$

where $K_1 = K_{1,\text{c}} = (B^{(4)}_{1,1,2,2} + ...)$ is the (first-order) cubic anisotropy constant of the material. Similarly as with the case of the uniaxial anisotropy, the sign of K_1 determines whether the directions $(m_1, m_2) = (1, 0)$ and $(m_1, m_2) = (0, 1)$ (for a negative value of the anisotropy constant) or the directions $(m_1, m_2) = (\sqrt{2}/2, \sqrt{2}/2)$ and $(m_1, m_2) = (-\sqrt{2}/2, \sqrt{2}/2)$ (for a positive value of the anisotropy constant) are favored. An in-plane cubic anisotropy has thus two *easy* axes (oriented at 90° with respect to each other) and two *hard* axes (oriented at 90° with respect to each other and at 45° with respect to the easy axes).

1.2.5 Magneto-elastic anisotropy

As will be described in further detail in chapter 4, the application of a strain to a magnetic material gives rise to an additional contribution F_S to the magnetic free energy. Such effect is known as *magneto-elastic* effect (or *magnetostriction*), and the magneto-elastic contribution to the magnetic free energy can be described as follows:

$$F_S = \int_V f_S(\mathbf{r}) \mathrm{d}V, \tag{1.16}$$

where f_S is the magneto-elastic free energy density of the material. In the following, the description will be limited, for simplicity, to the case of a position-independent free energy density (i.e. $f_S(\mathbf{r}) = f_S$). The description can however be easily extended to the general case.

Considering the coordinate system given in Fig. 1.4, it is possible to write the magneto-elastic free energy density as follows [10]:

$$\begin{aligned} f_S = & B_1 \left[\varepsilon_{xx} \left(\cos^2 \theta_x - \frac{1}{3} \right) + \varepsilon_{yy} \left(\cos^2 \theta_y - \frac{1}{3} \right) + \varepsilon_{zz} \left(\cos^2 \theta_z - \frac{1}{3} \right) \right] + \\ & + \frac{1}{2} B_2 \left(\varepsilon_{yz} \cos\theta_y \cos\theta_z + \varepsilon_{xz} \cos\theta_x \cos\theta_z + \varepsilon_{xy} \cos\theta_x \cos\theta_y \right), \end{aligned} \tag{1.17}$$

where ε_{ii} indicates the direct strain in the $i \in \{x, y, z\}$ direction, ε_{ij} with $i \neq j$ indicates the ij shear strain, θ_i indicates the angle between the magnetization vector $\mathbf{M}$ and the i-th axis, and $B_{1,2}$ indicate the magnetoelastic coupling coefficients [10, 11].

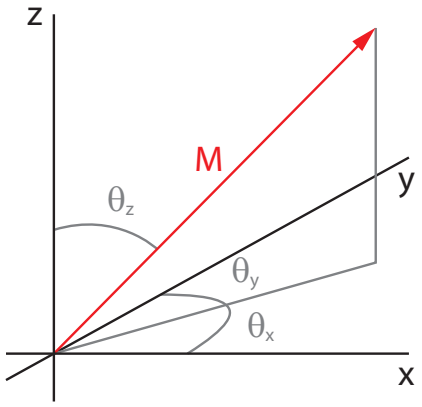

Figure 1.4: Schematic view of the coordinate system employed for the calculations of the magnetoelastic anisotropy, where θ_i, with $i \in \{x, y, z\}$, indicates the angle between the magnetization vector $\mathbf{M}$ and the i-th axis.

Equation (1.17) describes the general case of a magnetostrictive material under a generic strain $\underline{\underline{\varepsilon}}$, and with the magnetization vector $\mathbf{M}$ pointing along a generic direction in space. As the model presented in this section will be used to analyze the experimental results presented in chapter 4, the calculations for the magneto-elastic free energy density will be limited to the

case of a thin polycrystalline magnetic film, where the magnetization vector lies within the xy plane, such as the one of the samples analyzed in chapter 4. With such considerations, it is possible to re-write Eq. (1.17) as follows:

$$f_{\mathrm{S}} = B_1 \left[\varepsilon_{xx} \left(\cos^2 \theta_x - \frac{1}{3} \right) + \varepsilon_{yy} \left(\cos^2 \theta_y - \frac{1}{3} \right) - \frac{1}{3} \varepsilon_{zz} \right] + \frac{1}{2} B_2 \varepsilon_{xy} \cos\theta_y \cos\theta_x. \quad (1.18)$$

For the experiments described in chapter 4, the effects due to the shear strain ε_{xy} can be considered negligible compared to the contribution of the direct strain ε_{xx} and ε_{yy} [12]. Thus, the second term in Eq. (1.18) can be neglected. Moreover, from Fig. 1.4, it is possible to express θ_x as function of θ_y (i.e. $\theta_x = \pi/2 - \theta_y$), and it is then possible to write Eq. (1.18) as follows:

$$f_{\mathrm{S}} = B_1 \left[(\varepsilon_{xx} - \varepsilon_{yy}) \cos^2 \theta_x - \frac{1}{3} (\varepsilon_{xx} - 2\varepsilon_{yy} + \varepsilon_{zz}) \right]. \quad (1.19)$$

Thus, it is possible to express the magneto-elastic free energy as the sum of a volume term and of a term dependent from $\cos^2 \theta_x$, which then gives rise to a uniaxial anisotropy induced by the application of a strain to the magnetostrictive material. The term in Eq. (1.19) constant with respect to the orientation of the magnetization vector can be left out of the calculation, thus leading to the following formulation for the magneto-elastic free energy density:

$$f_{\mathrm{S},\theta_{\mathrm{x}}} = K_{\mathrm{ME}} \cos^2 \theta_x = B_1 (\varepsilon_{xx} - \varepsilon_{yy}) \cos^2 \theta_x. \quad (1.20)$$

The magnetoelastic coupling coefficient B_1 can be expressed as function of the magnetostrictive constant λ_s of the material and of its Young modulus Y [11–13], allowing one to express the magnetoelastic anisotropy term K_{ME} as follows:

$$K_{\mathrm{ME}} = -\frac{3}{2} \lambda_s Y (\varepsilon_{xx} - \varepsilon_{yy}). \quad (1.21)$$

The formulation of the *magneto-elastic anisotropy* K_{ME} given in Eq. (1.21) will be employed for the analysis of the experimental results presented in chapter 4.

1.3 Brown's equation for the static equilibrium

Under the assumptions of the micromagnetic model, the equilibrium magnetization $\mathbf{M}_{\mathrm{eq}}$ of the magnetic material can be found by minimizing the magnetic free energy F introduced in section 1.2 with respect to the magnetization $\mathbf{M}$.

The condition for the equilibrium magnetization has been calculated by Brown, who expressed the equilibrium condition as function of an effective magnetic field $\mathbf{H}_{\mathrm{eff}}$ arising from the magnetic free energy F. Such effective field can be written, considering only the first four terms of Eq. (1.6), as follows [9]:

$$\mathbf{H}_{\mathrm{eff}} = \frac{2A}{M_{\mathrm{s}}^2} \nabla^2 \mathbf{M} + \mathbf{H}_{\mathrm{str}} + \mathbf{H} - \frac{1}{\mu_0} \nabla_{\mathbf{M}} f_{\mathrm{ani}}. \quad (1.22)$$

With the effective magnetic field $\mathbf{H}_{\text{eff}}$ defined from Eq. (1.22), it is possible to express the equilibrium condition for the magnetization as follows [9]:

$$\mathbf{M}_{\text{eq}} \times \nabla_{\Sigma}\mathbf{M}_{\text{eq}} = 0, \tag{1.23}$$

$$\mathbf{M}_{\text{eq}} \times \mathbf{H}_{\text{eff}} = 0, \tag{1.24}$$

where $\nabla_{\Sigma}\mathbf{M}$ identifies the gradient of $\mathbf{M}$ along the surface Σ of the magnetic material. The solution of these equations along the entire volume of the magnetic material will allow for the determination of the equilibrium magnetization.

1.4 Stoner-Wohlfarth model

The micromagnetic model introduced in the previous section allows for the description of a magnetic material with a general magnetization $\mathbf{m}(\mathbf{r})$. Some magnetic materials can, however, also be described with a simpler model, known as the *Stoner-Wohlfarth model* [14], where the magnetization of the material is described as a single magnetic entity (*macro-spin*) that rotates coherently to align itself along an external magnetic field (i.e. it is assumed that the exchange energy in the material is strong enough that all of the microscopic spins of the material are always aligned). Within the Stoner-Wohlfarth model, it is possible to express the magnetic free energy density f of a magnetic material with the following relation:

$$f = f_{\text{Z}} + f_{\text{ani}} + f_{\text{other}}, \tag{1.25}$$

where the total magnetic free energy F_{tot} is expressed as $F_{\text{tot}} = Vf$, being V the volume of the magnetic material (i.e. it is assumed that the free energy density f is not dependent on the position within the material). For the following description it will be assumed, for simplicity, that $f_{\text{other}} = 0$.

This model can be used for the determination of the magnitude of the magnetic anisotropy constants of a magnetic material, and will be employed in this work (see chapter 3) for the determination of the magnetic anisotropy of thin ferromagnetic Heusler compound films. As the materials which will be analyzed with this model (see chapter 3) exhibit a magneto-crystalline anisotropy given by the combination of an uniaxial and a cubic term, the description given in this section will be limited, for simplicity, only to the case of a material exhibiting a combination of an uniaxial and cubic anisotropy. Under these assumptions, it is possible to write the magnetic free energy density as follows:

$$f = -\mu_0 H_{\text{ext}} M_s \cos(\theta) + K_u \sin^2(\theta - \phi_u) + K_1 \sin^2(\theta - \phi_c)\cos^2(\theta - \phi_c), \tag{1.26}$$

where H_{ext} identifies the magnitude of the external magnetic field, M_s the saturation magnetization of the material, K_u and K_1 the first order uniaxial and cubic anisotropy constants

respectively, and where the angles θ and ϕ_u are defined according to the convention sketched in Fig. 1.5. The formulation shown in Eq. (1.26) does not represent the general case of an material exhibiting a combination of an uniaxial and a cubic anisotropy: the calculations will be, for simplicity, limited to the case of a magnetic thin film with an in-plane magnetization, which corresponds to the case analyzed in chapter 3. In the case that the easy axis of the uniaxial anisotropy is not parallel to one of the easy axes of the four-fold cubic anisotropy, a different angle ϕ_c for the cubic anisotropy (which can always be expressed as $\phi_c = \phi_u + \xi$, where ξ is a fixed angle) has to be included in the calculations. For the following calculations, the case $\phi_u = \phi_c = \phi$ will be considered for simplicity. The calculations can however be easily extended to the general case of $\phi_u \neq \phi_c$.

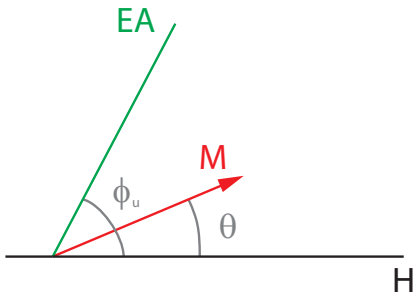

Figure 1.5: Schematic view of the coordinate system employed for the calculations of the magnetic anisotropy within the Stoner-Wohlfarth model, where the externally applied magnetic field is coincident with the x axis, and where EA indicates the uniaxial anisotropy axis. The 4-fold cubic anisotropy axes are coincident with the uniaxial anisotropy axis and its perpendicular axis.

The orientation of the macro-spin in the Stoner-Wohlfarth model can be determined by finding the angle $\theta = \theta_0$ that minimizes the magnetic free energy density. The condition at which the magnetic free energy density is minimum are given by the following relations:

$$\left.\frac{\partial f}{\partial \theta}\right|_{\theta=\theta_0} = \mu_0 H_{\text{ext}} M_s \sin(\theta_0) + K_u \sin(2(\theta_0 - \phi)) + \frac{1}{2} K_1 \sin(4(\theta_0 - \phi)) = 0, \tag{1.27}$$

$$\left.\frac{\partial^2 f}{\partial \theta^2}\right|_{\theta=\theta_0} = \mu_0 H_{\text{ext}} M_s \cos(\theta_0) + 2K_u \cos(2(\theta_0 - \phi)) + 2K_1 \cos(4(\theta_0 - \phi)) > 0. \tag{1.28}$$

The projection of the magnetization vector $\mathbf{M}$ along the applied field direction, given by $M_{\mathbf{H}} = M_s \cos(\theta)$, can then be determined by solving Eq. (1.27) and Eq. (1.28) as a function of the applied field $\mathbf{H}_{\text{ext}}$ (and for a given orientation ϕ of the anisotropy axis). Due to the periodicity of the sinusoidal function, the solutions of Eq. (1.27) and Eq. (1.28) give rise to two curves for $\theta_0 = \theta_0(H)$. By combining these two curves, the magnetic hysteresis loop of the macro-spin can then be determined. An example of some hysteresis loops determined by solving Eq. (1.27) and Eq. (1.28) as function of the applied magnetic field H for different

angles ϕ between the applied magnetic field and the magnetic anisotropy axes is shown in Fig. 1.6.

By solving Eq. (1.27) and Eq. (1.28) for different material parameters, it is possible to model the magnetic response of the material. This model can then be used to fit the experimentally-acquired hysteresis loops to estimate, e.g., the magnitude of the magnetic anisotropy constants.

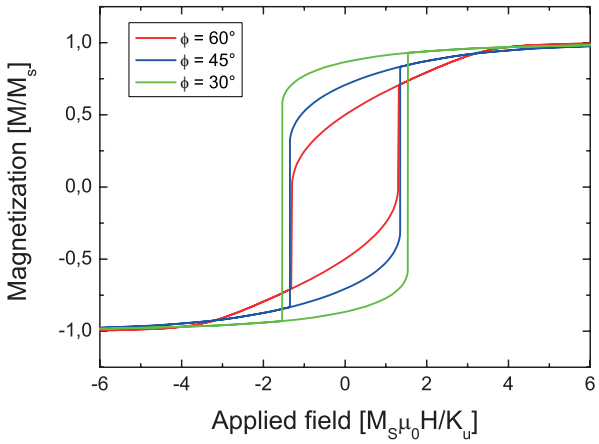

Figure 1.6: Example of hysteresis loops calculated with the Stoner-Wohlfarth model for a material with both uniaxial and cubic anisotropy contributions, for the case of an external magnetic field applied at various angles ϕ with respect to the easy axis of the uniaxial anisotropy. A value of $K_u = K_1$ and $\phi_c = \phi_u = \phi$ have been assumed for simplicity, and the hysteresis cycle is plotted as function of $\mu_0 H M_s/K_u$ for the x axis and the projection of the magnetization vector $\mathbf{M}$ along the direction of the applied magnetic field normalized with respect to M_s.

The Stoner-Wohlfarth model presented in this section allows for the estimation of the uniaxial and cubic anisotropy terms by fitting the hysteresis loops acquired at different orientations of the external magnetic field $\mathbf{H}$ to the loops calculated with the model. However, as this model treats the whole magnetic material as a single macro-spin, more complex switching mechanisms such as the creation (and expansion/reduction) of magnetic domain walls are not included. Thus, the Stoner-Wohlfarth model here described is valid only when the assumption of treating the material as a single macro-spin reasonably holds. Due to the generation and expansion of magnetic domains, the region of the hysteresis loops around the coercive field and, in general, along the magnetic easy axes of the material cannot be well described by the Stoner-Wohlfarth model [15]. The Stoner-Wohlfarth model can however be reasonably employed for the description of the *reversible* part of the hysteresis loop, i.e. when a magnetic field between zero and the saturation condition is applied to the material (after that the material has been saturated once) [15, 16], as the material does not tend to break into domains

in the high magnetic field region. The reversible part of the hysteresis loop, which will be employed in chapter 3 for the determination of the magnetic anisotropies of ferromagnetic thin Heusler compound films, is schematically shown in Fig. 1.7.

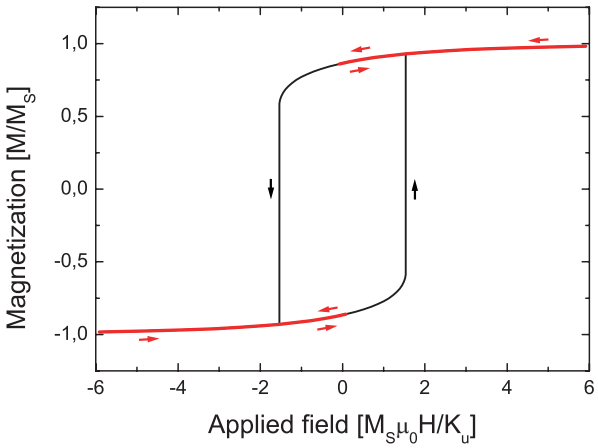

Figure 1.7: Schematic representation of the reversible part of a magnetic hysteresis loop, marked in red in the image. After the saturation in one defined direction of a magnetic material (and the relaxation to zero of the applied magnetic field), the application of a magnetic field in the same direction of the saturating field will give rise to a "reversible" response of the magnetization of the material, as marked in the image.

1.5 Magnetization dynamics

The description of the magnetic configuration of a material under the micromagnetic approximation introduced in Sections 1.2 and 1.3 allows for the determination of the static equilibrium condition. However, this thermodynamical model does not provide any information on the dynamical process that leads to the equilibrium condition.

The dynamics of the magnetization in a material can be described by the *Landau-Lifshitz-Gilbert* (LLG) equation, given by the following differential equation [17, 18]:

$$\dot{\mathbf{M}} = -\gamma \mathbf{M} \times \mathbf{H}_{\text{eff}} + \frac{\alpha}{M_{\text{s}}} \mathbf{M} \times \dot{\mathbf{M}}, \tag{1.29}$$

where $\dot{\mathbf{M}}$ is the total time derivative of $\mathbf{M}$, γ the gyromagnetic ratio, and where the parameter α is defined as the *Gilbert damping*.

The LLG equation describes the combination of an un-damped precession of the magnetic moment $\mathbf{M}$ around the effective magnetic field $\mathbf{H}_{\text{eff}}$, described by $-\gamma \mathbf{M} \times \mathbf{H}_{\text{eff}}$, with a damping term, described by $\frac{\alpha}{M_{\text{s}}} \mathbf{M} \times \dot{\mathbf{M}}$, which allows for the achievement of the equilibrium position (i.e. $\mathbf{M} \parallel \mathbf{H}_{\text{eff}}$) in a finite time. The effect of the two terms of the LLG equation are schematically shown in Fig. 1.8.

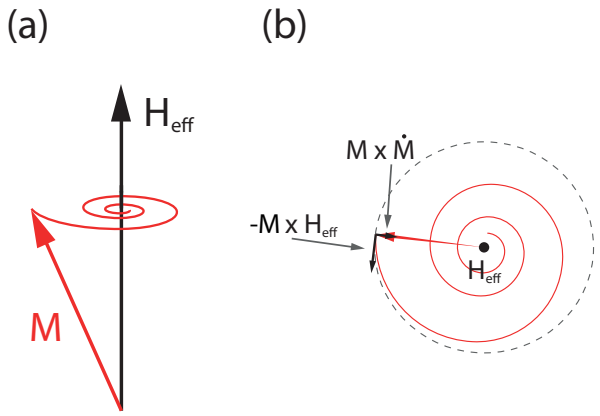

Figure 1.8: Schematic description of the damped precession of a magnetic moment around the effective applied field as described by the LLG equation. (a) Damped precession of a magnetic moment $\mathbf{M}$ around the applied effective field $\mathbf{H}_{\text{eff}}$; (b) Top view of the precession shown in (a), illustrating the contributions to the LLG equations arising from the precession and the damping terms.

1.6 Spin-torque effect

Due to the interactions between the spin of the electrons and the local magnetization, the flow of a current in a magnetic material is affected by its magnetic configuration, leading to a magnetization-dependent response of the electrical properties of a material, such as e.g. its resistivity. A typical example of this magnetization-dependent response of a material are magneto-resistance effects such as, e.g., the giant magneto-resistance (GMR) effect [19]. Due to the same interactions, also the local magnetization can be affected by a flow of spin-polarized electrons. This effect, known as *spin-torque*, was first suggested in 1984 [20], and has been since then observed in a variety of systems [21]. The spin-torque effect can be described by two additional terms in the LLG equation (see section 1.5), which can then be written as follows [21–23]:

$$\begin{aligned}\dot{\mathbf{M}} &= -\gamma\mathbf{M}\times\mathbf{H}_{\text{eff}} + \frac{\alpha}{M_s}\mathbf{M}\times\dot{\mathbf{M}} + \dot{\tau}_{\text{adia}} + \dot{\tau}_{\text{non-adia}} = \\ &= -\gamma\mathbf{M}\times\mathbf{H}_{\text{eff}} + \frac{\alpha}{M_s}\mathbf{M}\times\dot{\mathbf{M}} - (\mathbf{u}\cdot\nabla)\mathbf{M} + \beta\mathbf{M}\times(\mathbf{u}\cdot\nabla)\mathbf{M},\end{aligned} \tag{1.30}$$

where γ is the gyromagnetic ratio, $\mathbf{M}$ is the magnetization vector, $\mathbf{H}_{\text{eff}}$ the effective applied magnetic field (see section 1.3), α and β are, respectively, the Gilbert damping constant and the non-adiabaticity parameter, and $\mathbf{u}$ is defined as follows:

$$\mathbf{u} = \frac{gP\mu_B}{2eM_s}\mathbf{j}, \tag{1.31}$$

being P the spin-polarization of the material, and where $\mathbf{j}$ is the current density vector.

As shown in (1.30), the spin-torque effect can be described as two additional terms in the LLG equation, namely the *adiabatic* spin-torque $\dot{\tau}_{\text{adia}}$ and the *non-adiabatic* spin-torque $\dot{\tau}_{\text{non-adia}}$ contributions.

The adiabatic spin-torque contribution describes the effect of the flowing spin-polarized electrons on the magnetic configuration of a magnetic material when it is assumed that the spin of the flowing electrons aligns itself *adiabatically* (and instantly) to the local magnetization of the material. As schematically shown in Fig. 1.9, when the electrons flow into an area with a gradient of the local magnetization, the spin of these electrons aligns itself with the local magnetization vector. However, due to the conservation of angular momentum, the alignment of the electronic spin gives rise to a torque on the local magnetization, which will lead to a rotation of the local magnetization of the material.

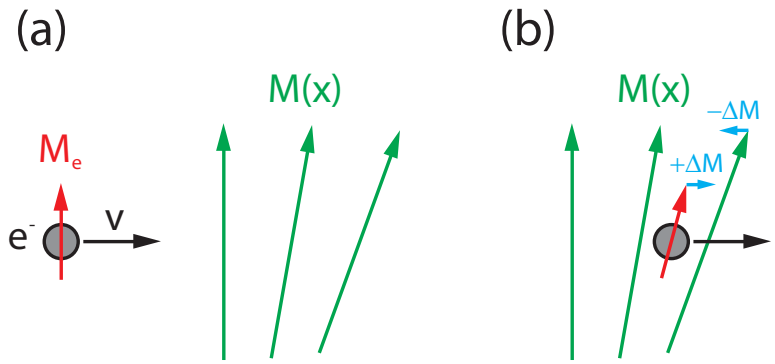

Figure 1.9: Adiabatic spin-transfer-torque effect. (a) An electron flowing through a magnetic material will align its spin with the direction of the magnetization; (b) Once the electron flows in a region with a gradient of the local magnetization, the electronic spin will align adiabatically to the direction of the local magnetization, giving rise, due to the conservation of angular momentum, to a torque on the local magnetization.

The contribution of the adiabatic spin-torque effect can be described as an additional term to the LLG equation, given by [22, 23]:

$$\dot{\mathbf{M}}_{\text{adia}} = -(\mathbf{u} \cdot \nabla)\mathbf{M}.$$

The adiabatic spin-torque contribution assumes that the spin of the flowing electrons aligns itself instantly with the local magnetization vector of the material. However, if the electrons flow into a region of the material with a large gradient of the local magnetization, it is possible that the spin of the electrons does not fully align to the local magnetization. This effect gives rise to the second contribution to the LLG equation [22]:

$$\dot{\mathbf{M}}_{\text{non-adia}} = \beta \mathbf{M} \times (\mathbf{u} \cdot \nabla)\mathbf{M},$$

where the non-adiabaticity parameter β describes the strength of this additional, non-adiabatic spin-torque term (i.e. a value of $\beta = 0$ implies that the electronic spin aligns itself instantly with the local magnetization term).

This model will be employed in chapter 5 to describe the current-induced domain wall motion effects in nanostructured ferromagnetic oxidic materials.

1.7 Micromagnetic simulations

The LLG equation introduced in the previous sections cannot, in general, be solved analytically. It is however possible to calculate a numerical solution of the LLG, which can then be employed to *simulate* the magnetic state of a given material. Given that the LLG equation is valid in the micromagnetic approximation, the simulation of the magnetic configuration of a material through the numerical solution of the LLG equation is often referred to as *micromagnetic simulations*.

These simulations are often carried out using a finite-difference method to solve the LLG equation, where specific software solutions such as OOMMF [24] or the *MicroMagnum* framework [25] have been developed. To determine the size of the numerical discretization to be used in the micromagnetic simulations, it is necessary to determine the exchange length of the simulated material. The size of the cells employed in the numerical discretization of the finite-difference method has to be smaller than the exchange length of the magnetic material, as the simulation of under-resolved structures can lead to unreliable results [26]. The magneto-static exchange length of a magnetic material is given by:

$$l_{\mathrm{ex}} = \sqrt{\frac{2A}{\mu_0 M_s^2}}, \tag{1.32}$$

where A is the exchange stiffness and M_s is the saturation magnetization of the magnetic material. The exchange length is thus dependent on the specific parameters of the analyzed material and needs, thus, to be determined prior to the beginning of the simulation.

In chapters 4 and 5 of this thesis, micromagnetic simulations of the analyzed materials were carried out to allow for a better interpretation of the experimental results.

Chapter 2

Experimental Methods

In this chapter, the experimental methods employed to carry out the experiments described in the next chapters will be presented. First, the lithographical techniques that allowed for the fabrication of the samples will be introduced, with a focus on the description of electron and ion-beam lithography, as those techniques are of vital importance for the fabrication of nanostructured samples with good resolutions. After an introduction on the sample fabrication, the technique of x-ray photoemission electron microscopy, employed to determine the magnetic configuration of nanostructured elements will be described, along with the magneto-optic Kerr effect, used to characterize the magnetic properties of the analyzed samples.

2.1 Lithographical patterning of magnetic samples

The fabrication of structures with geometrical dimensions down to the nm range requires the use of specific patterning technologies, which fall under the name of *lithographical fabrication techniques*. For the work presented in this thesis, various nanostructures have been lithographically patterned from different materials. The employed techniques, which will be discussed in detail in this section, are *electron beam lithography* for defining the structures, and *wet chemical etching* and Ga^+ *focused-ion-beam* lithography for the actual fabrication of the structures. The films used in the work described in this thesis were fabricated by various deposition techniques, including sputter-assisted deposition, molecular beam epitaxy and pulsed laser deposition.

2.1.1 Electron beam lithography

Electron beam lithography (EBL) is a technique that allows for defining the nanostructures with a spatial resolution down to 10 nm [27]. The general operating principle of EBL consists of coating a sample with an electron sensitive polymeric *resist*, by spinning a solution of the polymeric resist on the surface of the sample followed by the evaporation of the solvent, and

then exposing certain areas of the resist using a focused electron beam [27]. Depending on the chemical and physical properties of the resist (which are defined as *positive* and *negative* tone resists), the interaction of the electron beam with the polymer molecules renders the exposed material either soluble or insoluble to a specific chemical, called *developer*, for positive and negative tone resists respectively. Once the resist film on the sample surface has been exposed with the electron beam, and developed with the developer, it can be processed further, for example through an etching step (either chemical or ion-beam) or a material deposition step.

In EBL, a focused electron beam is scanned across the sample with a pre-defined pattern, which, by exposing the polymeric resist, transfers a pre-defined pattern onto the sample. The focused electron beam is scanned across the sample employing the same working principle as scanning electron microscopy (SEM), and it is in fact possible to convert many SEM systems to perform lithographical exposures. The maximum deflection of the electron beam, achieved by applying an electric field perpendicular to the beam axis, defines the stitching field of the lithographical exposure, while the minimum deflection of the electron beam that can be achieved defines, along with the resist employed for the lithographical processing, the resolution of the lithographical system. Both the stitching field and the spatial resolution of the lithographical process may be modified (by the same factor) by changing the zoom factor of the electron optics, resulting in a better spatial resolution (at the cost of the dimension of the stitching field) for larger zoom factors.

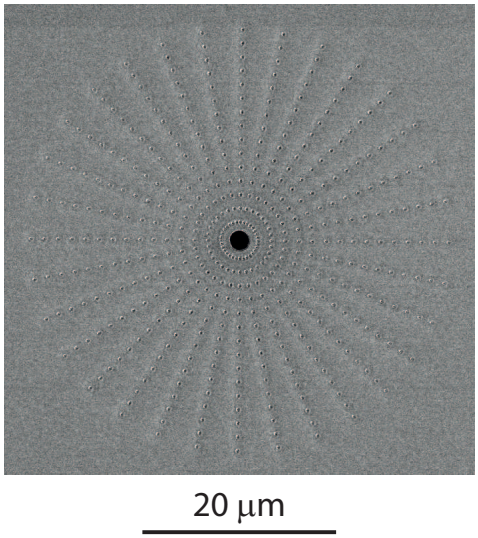

Figure 2.1: SEM micrograph of a series of 20 nm thick Ni nanostructures fabricated on a GaAs substrate. The smallest features in the image are nanostructured ellipses with major and minor semi-axes of 400 and 200 nm respectively.

If the dimensions of the pattern that is going to be exposed are larger than the dimensions of the stitching field, the exposure will occur in several single exposure steps, dividing the total

area of the pattern in several *stitching fields*. In this mode, the system will move the sample stage after each exposure, and the final exposure will be composed of a *stitching* of different single exposures. Clearly, the precision in the movement of the sample stage is one of the crucial factors determining the quality of the overall lithographical exposure. Therefore, the lithographical exposures are typically carried out in dedicated EBL systems equipped with a laser-interferometer stage, and the presence of this high-precision stage is typically one of the main factors weighing in favor of a dedicated EBL system instead of a converted SEM system.

For the fabrication of the samples analyzed in this thesis a Raith Pioneer dedicated EBL system has been employed, which facilitated the fabrication of nanostructures down to about 100 nm, an example of which is shown in Fig. 2.1. The definition mask were modulated using the software provided by the manufacturer of the EBL system, and then imported onto the control program of the EBL system, where additional parameters such as the exposure dose are inserted prior to the exposure of the resist with the electron beam.

2.1.2 Focused ion beam lithography

As described in the previous section, using the EBL technique, a focused electron beam is employed to expose a chemical resist in order to transfer a pre-defined pattern onto the sample surface. An alternative approach to EBL for the fabrication of nano-structured samples is the use of focused ion beam (FIB) lithography. In FIB lithography, a focused Ga^+ ion beam is scanned over the surface of the sample, depositing a given dose on the scanned areas. Depending on the magnitude of the deposited dose (and on other parameters such as the kinetic energy of the Ga^+ ion beam), the properties of the exposed material can be strongly modified, ranging from the implantation of Ga^+ ions to the complete removal of the material by sputtering.

As the implantation of Ga^+ ions can strongly influence the magnetic properties of a magnetic material [28], the complete removal of the magnetic material is often not necessary to fabricate magnetically insulated structures. However, as also shown in Chapter 4, the choice of the exposure dose is of key importance in the fabrication of magnetic nanostructures by FIB lithography.

The system employed to fabricate samples by FIB lithography is a dual-beam FEI Helios NanoLab 600i SEM/FIB microscope. In this dual-beam SEM/FIB system, the ion column is oriented at 52° with respect to the electron column, and the two beams intersect in one point of the chamber, defined as *eucentric point*. By aligning the sample so that the sample surface is at the eucentric point, it is possible to set the ion beam position operating only with the SEM column, thus preventing any unwanted damage from the ion beam to the sample. The Ga^+ ion beam is generated by a Tungsten needle set at a high voltage in contact with a liquid Gallium bath, which wets the Tungsten needle. The strong electric field at the tip of

the Gallium-wetted needle ionizes and field-emits the Ga^+ ions, which are then collected and focused onto the eucentric point by electron optics.

The exposure was carried out by designing a lithographical mask in the same operating principle as EBL, and then by importing the mask to the control program of the SEM/FIB system (with additional parameters such as the exposure dose and the beam energy). The exposure of the sample was then handled automatically by the FIB system. An example of a typical FIB exposure employed to fabricate magnetic nanostructures is shown in Fig. 2.2.

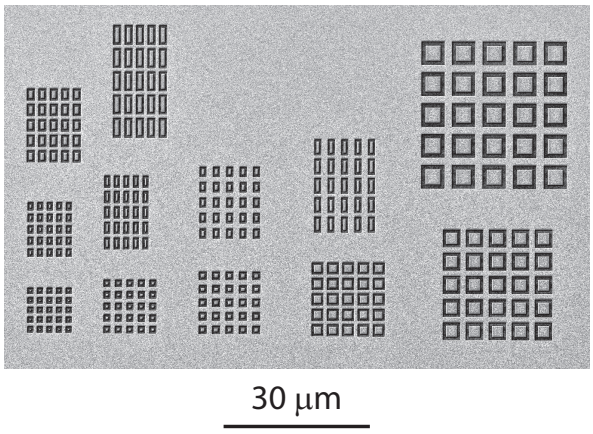

Figure 2.2: Scanning electron micrograph of a series of nanostructures fabricated with FIB lithography on a Co_2MnGa Heusler compound sample. The depth of the FIB etching is about 30 nm, equal to the thickness of the Co_2MnGa film.

2.2 Imaging of magnetic samples with x-ray PEEM

In order to detect the magnetic configuration of a material, it is necessary to find a probing technique that is sensitive to the magnetization of the material. Circularly polarized x-rays provide, thanks to the magnetic circular dichroism effect, a probing mechanism sensible to the magnetic configuration of the material. For the experiments described in this thesis, the x-ray magnetic circular dichroism effect has been combined with photoemission electron microscopy to obtain images of the magnetic configuration of a materials with sub-μm spatial resolutions. In this section, the x-ray magnetic circular dichroism effect will be introduced, followed by a description of photoemission electron microscopy.

2.2.1 X-ray magnetic circular dichroism

Circularly polarized photons carry a magnetic angular momentum of either $+1$ or -1 in units of $\hbar$ (hereafter defined as circularly positive and circularly negative polarized photons respectively). When a photon is absorbed by a material, it is known that the probability of a

transition $T_{i\to f}$ of an electron between an initial state $|i\rangle$ and a final state $|f\rangle$ is given by the following relation, known as Fermi's Golden Rule [29]:

$$T_{i\to f} \propto \langle f|\hat{H}|i\rangle\, \delta(E_f - E_i - \hbar\omega)\, \rho(E_f), \tag{2.1}$$

where E_i and E_f identify the energies of the initial and final state respectively, $\hbar\omega$ the energy of the incoming photon, $\langle f|\hat{H}|i\rangle$ the transition matrix element, where $\hat{H}$ is the Hamiltonian that describes the interaction between the photon and the electron, and $\rho(E_f)$ is the density of free states at the final energy E_f.

As a consequence of the terms in (2.1), the absorption of a photon of energy $\hbar\omega$ occurs with high probability only if certain conditions, defined as *dipole selection rules*, are simultaneously satisfied. According to the selection rules, a transition e.g. from a $2p$ core level to a $3d$ level is allowed. For the materials presented in this thesis, the attention will be focused on the $2p \to 3d$ transition, as the Fermi energy for these materials lies within the $3d$ band. The typical photon energies at which the $2p \to 3d$ transition occurs (for the materials analyzed in this thesis) lie within the soft x-ray range. Thus, from now on, unless noted, by "photon", a soft x-ray photon will be intended.

From the dipole selection rules, it is possible to observe that the electron spin orientation cannot change during the transition. Thus, it can be stated that the magnetic properties of the material do not influence the probability of a photon absorption by the material. However, many materials, including those analyzed in this thesis, exhibit a $2p$ core level splitting by spin-orbit coupling into two different levels, defined as $2p_{1/2}$ and $2p_{3/2}$, leading to two different absorption energies for the $2p \to 3d$ transition, defined as L_2 ($2p_{1/2} \to 3d$) and L_3 ($2p_{1/2} \to 3d$) absorption edges (or transitions). An example of L_2 and L_3 absorption edges is given in Fig. 2.3, where an x-ray absorption spectrum of a thin Ni film (measured in total electron yield) is shown.

By calculating the matrix element $\langle i|\hat{H}|f\rangle$ for the L_2 and L_3 transitions, it is possible to observe that the coupling of the spin and orbital moments leads to transition probabilities dependent on the photon polarization [30]. The spin polarization values for the L_2 and L_3 transitions are given in Table 2.1, and were calculated according to the procedure explained in Ref. [30].

	L_3: $2p_{3/2} \to 3d$		L_2: $2p_{1/2} \to 3d$	
	up	down	up	down
spin +1	0.25	0.75	0.625	0.375
spin -1	0.75	0.25	0.375	0.625

Table 2.1: Spin polarization for the L_2 and L_3 transitions when excited with photons of spin +1 or -1 (circularly polarized). The calculations have been taken from Ref. [30].

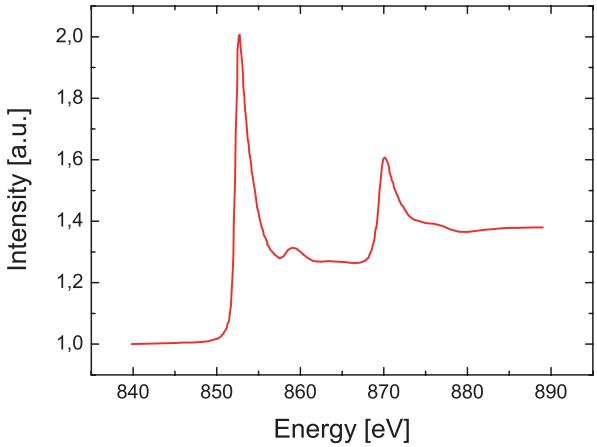

Figure 2.3: X-ray absorption spectrum of Ni for photon energies between 840 and 890 eV. The absorption peaks can be observed for energies of about 852.6 and about 870.1 eV, corresponding to the Ni L_3 and L_2 absorption edges respectively.

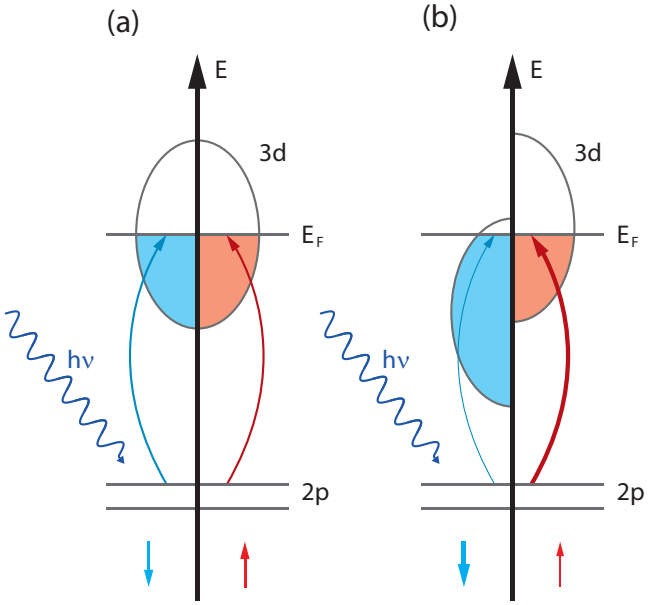

Figure 2.4: (a) L_3 transition for a non-magnetized material, showing an equal transition probability for the two spin sub-bands; (b) L_3 transition for a magnetized material, where the density of states at the Fermi energy for the two spin sub-bands is asymmetric, thus leading to a different transition probability for the two spin sub-bands.

For ferromagnetic materials such as Ni and Heusler alloys, it is possible to describe the magnetization by employing an itinerant ferromagnetic model [3], where an asymmetry in the conduction band for different orientation of the electron spin is observed (i.e. an asymmetry for the two spin *sub-bands* is observed). An imbalance in the density of free states at the

Fermi energy for the two spin sub-bands gives rise to an asymmetric absorption of circularly polarized x-rays, as schematically shown in Fig. 2.4. Thus, the circularly polarized x-rays act as a filter for the spin, as only transitions in one spin sub-band for a given photon polarization are allowed by (2.1), and the asymmetric spin-dependent density of states (i.e. asymmetries between the two spin sub-bands) at the Fermi energy acts as a further filter for the spin. By changing the relative orientation of those two spin filters (i.e. by inverting the chirality of the incoming photons or by magnetizing the material in the opposite direction), the number of electrons excited by the interaction with the circularly polarized photons (i.e. the total electron yield) can be changed. Thus, from the conditions arising from (2.1) and the aforementioned observations, it is possible to state that the magnetic contribution to the x-ray absorption is proportional to $\mathbf{M} \cdot \mathbf{k}$, being $\mathbf{M}$ the local magnetization of the magnetic material, and $\mathbf{k}$ the wave vector of the circularly polarized photons. By defining θ as the angle between $\mathbf{M}$ and $\mathbf{k}$, it is possible to observe that the magnetic contribution to the absorption of circularly polarized photons is proportional to $\cos(\theta)$.

In Fig. 2.5, an x-ray absorption spectrum in total electron yield for circularly polarized photons of both chiralities on a magnetized Ni thin film is shown. It is possible to observe that, by inverting the chirality of the x-ray photons, the electron yield at the L_2 and L_3 edges changes substantially. Such effect does not occur for a non-magnetized material (or a magnetized material where the magnetic vector is perpendicular to the photon wave vector).

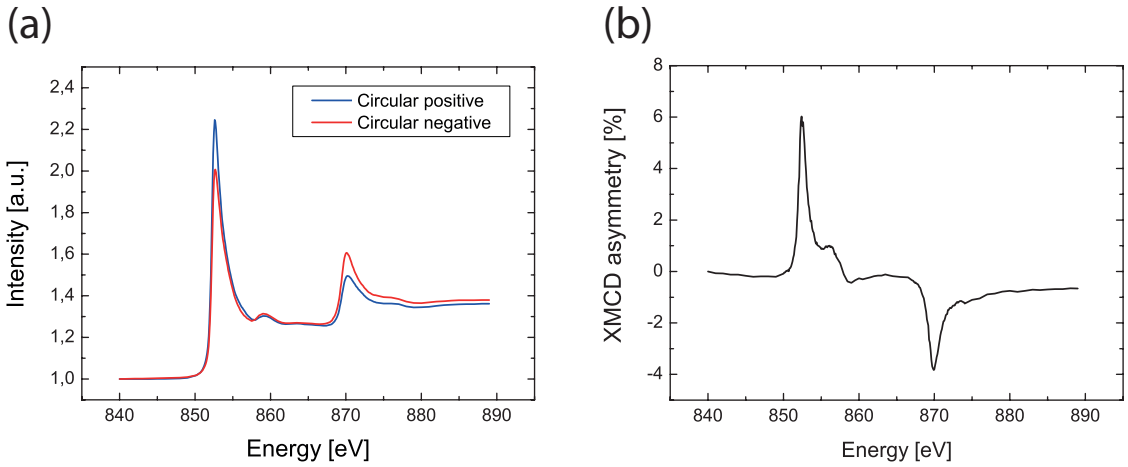

Figure 2.5: X-ray absorption spectrum for a magnetized Ni thin film with $\mathbf{M} \parallel \mathbf{k}$ as function of the photon chirality (red and blue curves). The black curve shows the resulting XMCD signal.

Therefore, the magnetic contribution can be extracted from the photon absorption (thus from the total electron yield), by calculating the so-defined *x-ray magnetic circular dichroic*

(XMCD) signal with the following relation:

$$I_{\mathrm{XMCD}} = \frac{I_+ - I_-}{I_+ + I_-}, \tag{2.2}$$

where I_+ and I_- identify the absorption yield of circularly polarized photons of positive and negative chiralities respectively. A typical XMCD signal calculated according to (2.2) is shown in Fig. 2.5, where the XMCD signal exhibits an opposite sign for the L_2 and L_3 absorption edges. This effect arises from the different sign of the spin orbit coupling for the two transitions (i.e. $j = l + s$ for the L_3 edge, while $j = l - s$ for the L_2 edge).

2.2.2 Synchrotron light

To carry out the imaging of magnetic samples based on the XMCD effect as contrast mechanism, a source of monocromatic and highly brilliant x-rays is required. Synchrotron light sources are x-ray sources that satisfy such experimental requirements, providing collimated and monochromatic x-ray beams with high brilliance.

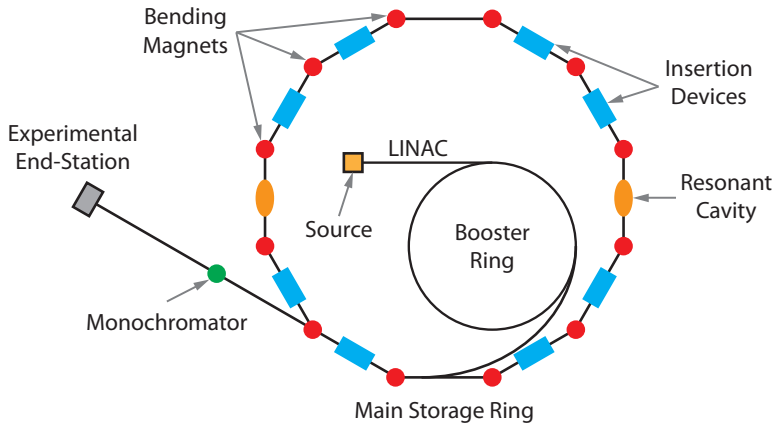

Figure 2.6: Sketch of a synchrotron light source. The electrons employed to generate the x-ray radiation are generated by an electron source, and accelerated to their nominal velocity by a combined linear accelerator (LINAC) and a booster ring. The electron bunches are then injected into the storage ring, where they will be employed to generate the x-ray radiation. The storage ring is composed of several linear sections, with bending magnets at their ends. Those magnets deflect the electron bunches into the following linear section. In the linear sections of the storage ring, insertion devices such as undulators and wigglers are employed to generate x-ray radiation with high brilliance, which is then employed at the experimental end-stations for the measurements. The energy lost by the electrons due to the Bremsstrahlung emission is re-integrated to the electron bunches by resonant cavities installed in the storage ring.

A synchrotron light source is an electron storage ring, where electron bunches are stored

in a closed orbit with typical orbital energies in the order of 1-2 GeV for third generation synchrotron light sources. As shown in Fig. 2.6, the storage ring of a synchrotron light source is composed of several straight sections, where periodic magnetic structures, called *insertion devices* (IDs) are positioned. The straight sections of the main storage ring are connected to each other by curved sections where dipolar magnets, called *bending magnets*, are positioned. By applying a magnetic field perpendicular to the velocity vector of the electrons orbiting in the storage ring, it is possible, thanks to the effect of the Lorentz force on the electrons, to accelerate the electrons towards the center of the storage ring and bend their orbit into the next linear section of the storage ring.

As the relativistic electrons experience, inside the bending magnets, an acceleration (perpendicular to their velocity vector), they emit photons along the direction tangential to their velocity vector. Every charged particle under acceleration emits dipole radiation (known as *Bremsstrahlung*), but this effect is significantly stronger for relativistic particles. For electrons orbiting in the storage ring of a synchrotron light source, the total irradiated power can be described by the following relation [31]:

$$P = \frac{\mathrm{e}^2\gamma^4\dot{v}^2}{6\pi\varepsilon_0\mathrm{c}^3}, \tag{2.3}$$

where $\gamma = (1-\beta^2)^{-1/2}$ is the Lorentz factor (with $\beta = v/c$), and v the velocity of the relativistic electron.

For charged particles experiencing an acceleration at relativistic velocities, the emission of Bremsstrahlung radiation occurs, as schematically shown in Fig. 2.7, in the reference frame of the laboratory, in a small cone tangential to the electron trajectory, with an angle of a factor γ smaller with respect to normal dipole radiation (i.e. the faster the electrons, the smaller the Bremsstrahlung cone will appear in the laboratory reference frame, giving rise also to a higher brilliance inside the emission cone). This angular dependence of the intensity of the radiation emitted by an accelerated relativistic particle is defined as *searchlight effect* [32].

Albeit the Bremsstrahlung emission from the bending magnets can be, and is, employed to carry out experiments requiring high brilliance x-ray radiation (the radiation emitted by electrons crossing a bending magnet exhibits a continuous spectrum, and its brilliance is strong enough to be employed for experiments requiring x-ray radiation), the primary function of these devices is to maintain the electron bunches in a closed orbit inside the storage ring. Thus, the bending magnets are not designed for the optimal generation of synchrotron radiation, but other magnetic structures can be designed to be more efficient than the bending magnets in the generation of x-ray radiation to be employed for experimental analyses. Such IDs, inserted in the straight sections of the storage ring (see Fig. 2.6), are called *wigglers* and *undulators*, and produce, in contrast to bending magnets, no net deflection or displacement of the electron beam. Inside these IDs, the electrons follow a curved path that enables the

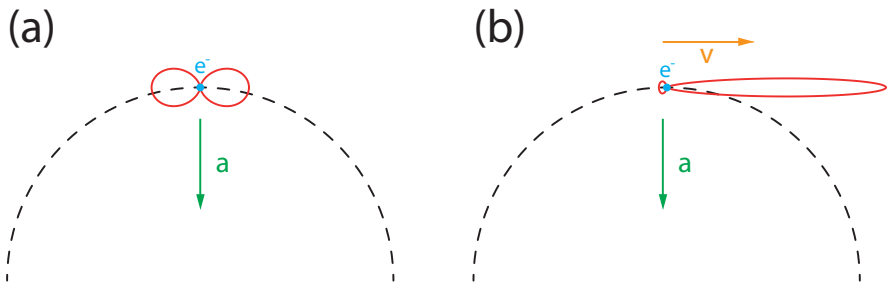

Figure 2.7: Sketch of the searchlight effect. Angular dependence of the intensity of the radiation emitted by (a) an accelerated charged particle; (b) an accelerated relativistic charged particle (where a value of $\beta = 0.99$ has been assumed). The angular amplitude of the intensity lobe is $1/\gamma$. The green arrow indicates the direction of the acceleration of the charged particle. The orange arrow in (b) indicates the direction of the velocity vector

generation of synchrotron radiation with a much higher brilliance with respect to the bending magnets and, for high field wigglers, also with a wider spectral range than the one accessible by bending magnets.

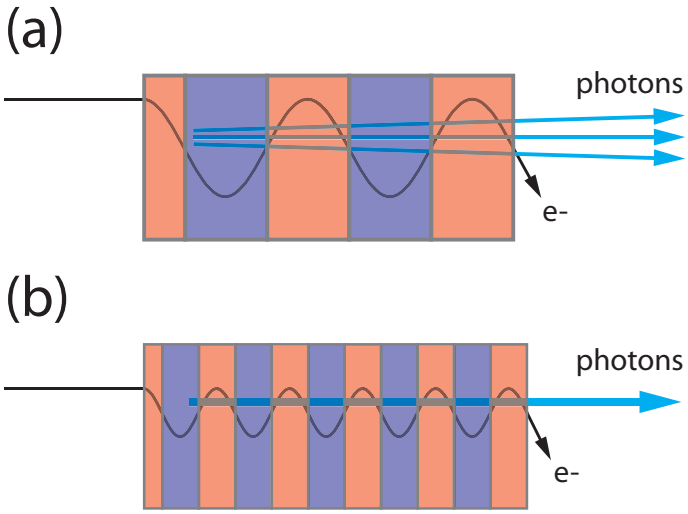

Figure 2.8: (a) Sketch of a wiggler with the electron path depicted; (b) Sketch of an undulator, with the electron path depicted. In the case of an undulator, constructive interference effects of the radiation emitted at each of the periodic deflections of the electron bunches allows for the generation of a high brilliance x-ray beam. The blue and red areas depict the magnets of the ID, oriented in the axis perpendicular to the page, and opposite directions.

As schematically shown in Fig. 2.8, both wigglers and undulators employ alternating magnetic fields to deflect the electron beam in opposite directions, causing the emission of radiation. For the experiments carried out in this thesis, the x-ray radiation generated from an

undulator ID has been employed. As the radiation emitted by the electrons crossing a bending magnet or an ID is strongly polychromatic, a grating mirror monochromator, operating on the same principle as the optical grating mirror monochromators [33], was employed to obtain a monochromatic x-ray beam.

Further details about the operating principles of a synchrotron light source and of the different typologies of IDs can be found e.g. in Refs. [31, 34].

2.2.3 Photoemission electron microscopy (PEEM)

In photoemission electron microscopy (PEEM), the electrons emitted from a sample illuminated by UV or x-ray light are detected to generate an high-resolution electron image. Moreover, low energy electrons can also be employed in this technique (defined, in this case, as low energy electron microscopy, LEEM), allowing for the acquisition of surface-sensitive images. The PEEM/LEEM technique was first developed in the 1930s [35] and, thanks to its high surface sensitivity, immediate applications in surface science were found. With the advent of synchrotron light sources, x-ray PEEM (where the electron images are generated from x-ray photoexcited electrons) has become an important technique mostly used in surface science (with an additional element sensitivity given by the illumination with monochromatic x-ray radiation) and, thanks to the magnetic dichroism effect, also in magnetic material studies.

For the experiments described in this thesis, a commercial PEEM setup fabricated by Elmitec (model LEEM III, of which a schematic sketch is shown in Fig. 2.9) was employed. The samples were illuminated by an x-ray beam oriented at an angle of 16° with respect to the sample surface, and the secondary electrons emitted from the surface of the sample following the absorption of the x-ray photons were extracted and accelerated by a 10-20 kV voltage applied between the sample and the magnetic objective lens of the microscope. As the absorption of the x-ray photons leads to the emission of secondary electrons with different kinetic energies, the microscope is also equipped with an imaging and energy analyzer section, combined with an energy slit, where the electrons that do not exhibit a defined kinetic energy do not cross the energy slit. The selection of the kinetic energy of the extracted electrons allows for an improvement of the imaging resolution thanks to the reduction of the chromatic aberration effects. After the energy analyzer section, the extracted electron beam is deflected by the projective optics to form an image onto a multiplier channel plate that, combined with a phosphor screen will amplify the electronic signal and convert the electron image into a visible image, recorded by a CCD camera.

The secondary electrons employed to form the x-ray PEEM image are emitted from the sample as a consequence of the absorption of the x-rays. As schematically shown in Fig. 2.10, when the x-ray photon is absorbed by a typical $3d$ metal, a $2p$ core electron is excited to the Fermi level, leaving a hole in the core level. Having a free core state, an electron from the

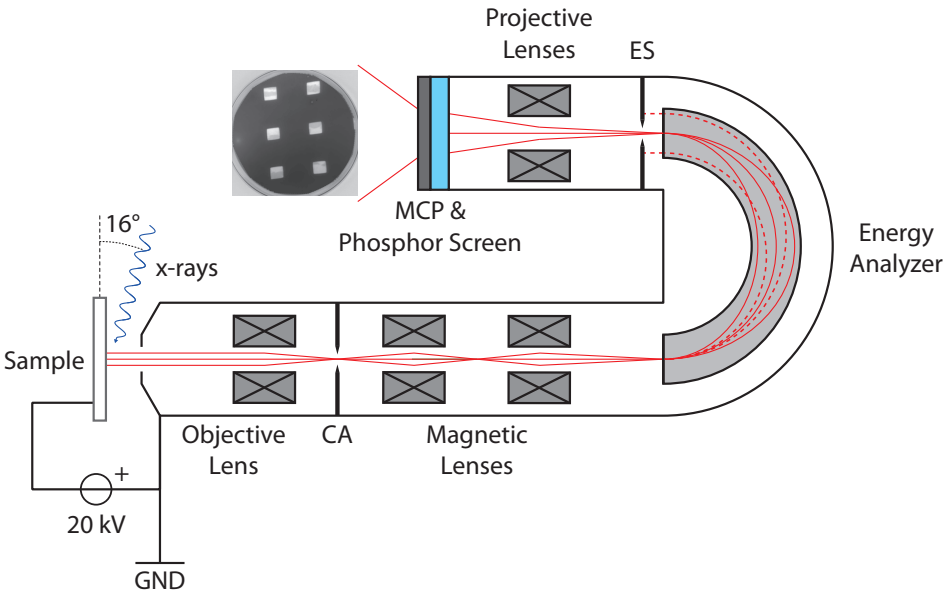

Figure 2.9: Sketch of an Elmitec PEEM setup. Electrons are emitted from the sample and collected by an objective lens, which conveys the electrons in the imaging section of the microscope. A contrast aperture (CA) in the diffraction plane of the objective lens allows for the selection of the electron angular dispersion. The electrons are then conveyed into an energy analyzer, which, in combination with an energy slit (ES), allows for the selection of the electron energy, thus reducing chromatic aberrations in the microscope. Finally, the electrons form an image on a multiplier channel plate combined with a phosphor screen, where the image is then acquired with a CCD camera.

Fermi level will relax to the core level, transferring the energy to an Auger electron, which will then thermalize via electron-electron scattering events, creating in the process a cascade of secondary electrons with a broad energy spectrum and with enough energy to overcome the vacuum energy and be emitted from the sample surface. Such electrons are then collected by the PEEM, and will form an electron image of the sample.

The typical resolution for XMCD-PEEM imaging is on the order of 20 nm, although newer PEEM setups with special aberration corrected lenses have been developed [36], promising a further increase in the spatial resolution. For the results presented in this thesis, the typical imaging resolution for PEEM was on the order of 20-50 nm [37]. All of the XMCD-PEEM imaging experiments presented in this thesis have been carried out at various synchrotron light sources across Europe. The imaging experiments were always carried out in a team of at least three people, to allow for the possibility of keeping the experiments running throughout the 24 hours.

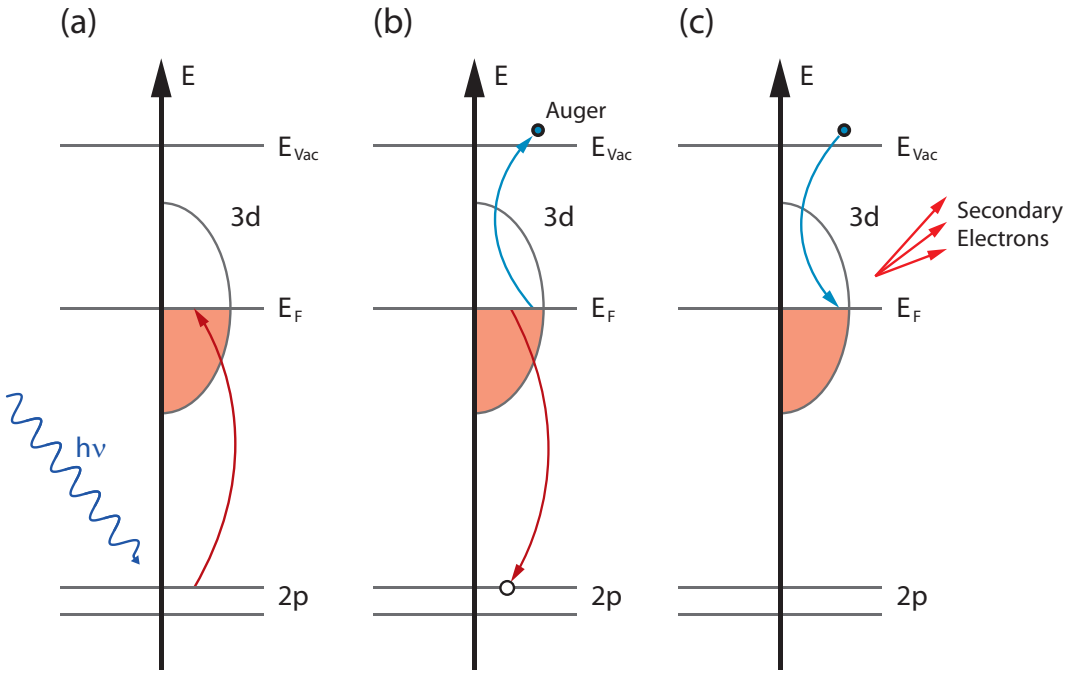

Figure 2.10: Sketch of the process that leads to the generation of the secondary electrons detected by the PEEM. (a) The interaction of the material with an energetic x-ray photon leads to the transition of one electron to the Fermi level, leaving an unoccupied state in a core level (defined as *core hole*); (b) An electron from the Fermi level recombines with the core hole, and this causes the excitation of one or more Auger electrons; (c) The Auger electrons thermalize in the material, giving rise to the emission of secondary electrons (with an energy just above the vacuum level), which will then be detected by the PEEM.

2.2.4 Image correction and analysis

There are a number of factors that can influence the quality of PEEM images, the most important given by the effect of instrument vibrations, thermal drifts and chromatic aberrations. An x-ray PEEM image is composed of a series of frames acquired in succession and averaged together. If the features in the electron image translate during the acquisition of the single frames, the quality of the averaged image can be seriously affected, as shown in Fig. 2.11(a). However, it is possible to process the acquired images and improve the image quality without losing any physical information from the images, as shown in Fig. 2.11.

A vibration of the sample stage with respect to the electron imaging optics can lead to an increase of the noise, which reflects, in the image, as blurred edges. As the typical period of these mechanical vibrations is comparable to the exposure time for the single PEEM frames (i.e. mechanical vibrations with a frequency $f > 1$ Hz), there are limited corrections that can be carried out on the final image. These are mostly given by Gaussian de-blurring filters.

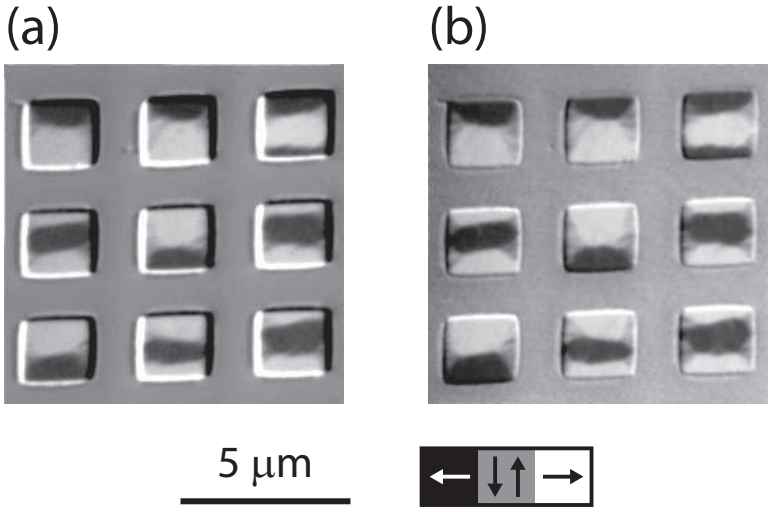

Figure 2.11: (a) XMCD-PEEM image of nanostructured Ni squares where the influence of drift and vibrations has not been corrected; (b) Same image as (a), with all corrections implemented, allowing the observation of fine features not visible in (a). The grayscale bar indicates the direction of the magnetic contrast in the images.

Instead, a reduction of the mechanical vibrations, e.g. by disabling the mechanical pumps operating on the chamber, provides a great improvement of the imaging quality.

The illumination of the sample with x-rays and/or other light sources and the cooling/heating of the sample holder lead to thermal drifts in the images, which are reflected by a rigid translation of the objects in the acquired frames. Thermal drifts occur, under normal conditions, on timescales of several minutes, thus not affecting the single x-ray PEEM images (the typical exposure time for a single x-ray PEEM image is between 1 and 10 seconds). However, as a PEEM image is comprised of many single images averaged together, the drifting of the objects in the image has to be corrected prior to the averaging of the single images, otherwise images such as the one shown in Fig. 2.11(a) will be obtained.

Assuming a rigid translation of the objects in an image, without rotation or deformation, it is possible to determine the magnitude of the vector that describes the translation of a feature in the image by calculating the bi-dimensional cross-correlation between the two images [38]. As shown in Fig. 2.12, where the calculation of the cross-correlation between a master image (Fig. 2.12(a)) and a generated drifted image (Fig. 2.12(b)) is reported (Fig. 2.12(c)), the cross-correlation exhibits a global maximum for the value corresponding to the translation vector between the two images. The drift between the two images can then be corrected by translating the drifted image by the calculated vector.

For the drift correction of the PEEM images acquired in this work, which was carried out at sub-pixel resolutions, an optimized algorithm [38] has been implemented. The operating

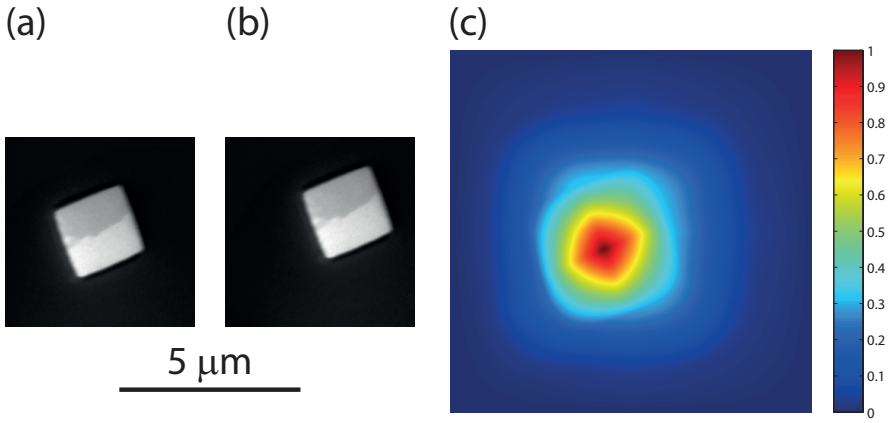

Figure 2.12: (a) Example image; (b) Same image as (a), artificially drifted; (c) Normalized cross correlation between (a) and (b), exhibiting a clear global maximum, which allows for the determination of the translation vector between (a) and (b).

principles of this image correction algorithm are described in detail in appendix A.

An additional improvement for the calculation of the drift correction can be carried out by applying edge detection filters to the images before the calculation of the cross correlation. An edge detection filter is a mathematical function that, applied to an image, allows for the recognition of *edges* in the image, where an *edge* is defined as a set of points in the image with sharp (or discontinuous) changes in the brightness.

Edges in an image can be determined with various methods, usually based on the analysis of the first and/or second derivative of the image. Edge recognition methods based on the first derivative generally calculate the gradient of the image and then search for maxima of magnitude of the gradient. Methods based on the second derivative, instead, determine the Hessian matrix of the image and then search for the zero-cross points (typically by analyzing the trace of the Hessian matrix, i.e. the Laplacian of the images).

Since the noise in the image may lead to the false detection of the edges (i.e. points in the image that are not part of an edge get recognized by the edge detection algorithm as edges), the images can be artificially blurred by a Gaussian blur filter (convolution with a Gaussian error function) to reduce the contribution of noise on the edge detection process.

Many different edge detection methods and algorithms have been developed, and are typically available as built-in functions in commercially available image processing softwares (such as ImageJ and Matlab). For the drift correction of the images presented in this thesis, the Sobel [39] and Canny [40] filters, which output is shown in Fig. 2.13, have been employed. The choice of one or the other method for the edge detection was simply based on the overall quality of the final drift correction.

The use of the images processed with an edge detection filter can simplify the drift correc-

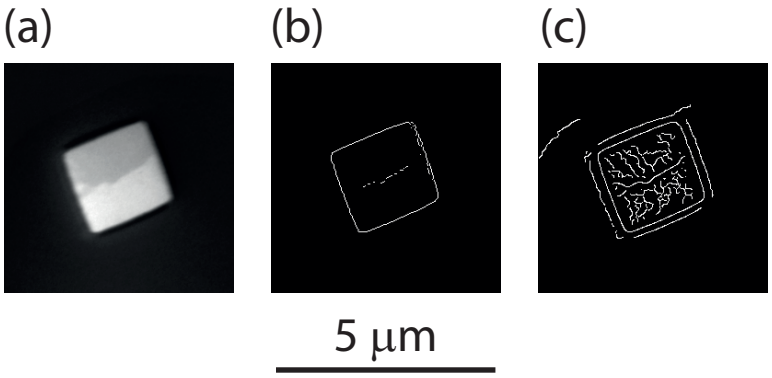

Figure 2.13: Examples of the output of different edge detection algorithms. (a) Original image; (b) Edge detection calculated with the Sobel filter; (c) Edge detection calculated with the Canny filter. The threshold of the filtering function was automatically determined by the image analysis software.

tion processing, as the calculation of the cross-correlation leads to a function where the global maximum is easier to identify, and is not influenced by the noise in the image (which can lead to secondary maxima in the cross-correlation). In Fig. 2.14, the cross-correlation between the same images shown in Fig. 2.12 is calculated. However, this time, the images were processed by a Sobel edge detection filter before the calculation of the cross-correlation, leading to a different cross-correlation function with respect to the one shown in Fig. 2.12 with a clearly detectable maximum.

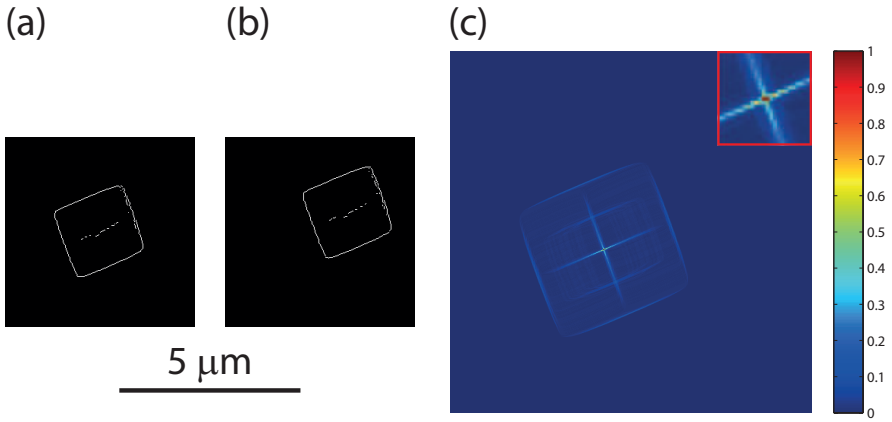

Figure 2.14: (a) Example image after the application of a Sobel edge detection filter; (b) Same image as (a), artificially drifted; (c) Normalized cross correlation between (a) and (b). The inset shows a magnified view of the region around the absolute maximum of the cross correlation function. The example image is the same as in Fig. 2.12.

For the drift correction of the PEEM images acquired in the work presented in this thesis,

the above described method has been implemented as a script in the commercial software Matlab, employing the built-in edge recognition functions for the detection of the edges in the image, and implementing the algorithm described in [38] for the drift correction of the images. Prior to the edge detection and drift correction, the acquired images were normalized by dividing them with a normalization image, acquired by de-focusing the objective lens of the PEEM. By doing so, the normalization image contains only features caused by the imaging section of the microscope (i.e. the multiplier channel plate and the phosphor screen, as described in section 2.2.3), and thus the normalization process will remove these artifacts from the images, improving both the drift correction processing and the quality of the final image.

For the analysis of the XMCD-PEEM images acquired at the Swiss Light Source, an analogous image correction program, developed by the Paul Scherrer Institut, was employed.

2.2.5 Application of voltages inside the PEEM

As further described in Chapter 4, to study the effect of an applied strain to the magnetic configuration of magnetostrictive nanostructured elements, voltages of different magnitudes have been applied *in-situ* across a piezoelectric substrate while carrying out XMCD-PEEM imaging. However, as described in section 2.2.3, the commercial Elmitec PEEM systems set the sample stage and the sample at a high voltage (typically 20 kV, with some variations depending on the specific endstation). Thus, the application of a voltage to the sample while the sample is being imaged by XMCD-PEEM requires a specially-designed setup that can operate remotely inside the high voltage rack of the PEEM.

To carry out the voltage-dependent measurements described in Chapter 4, the sample was contacted to the sample holder as shown in Fig. 2.15, where the top electrode of the sample was contacted directly with the conductive cap of the sample holder, and the bottom electrode of the sample was connected with a voltage generator inserted into the HV rack of the microscope. As changes of the voltage at the surface of the sample lead to strong changes in the PEEM images, the use of the contacting protocol shown in Fig. 2.15 allows, as the top surface of the sample is always at the same potential, for the imaging of the sample with an arbitrary voltage applied to the bottom electrode (and thus at different strain conditions applied to the nanostructured elements).

To apply the voltage to the sample, a special voltage generator unit was developed, allowing for a remote operation inside the high voltage rack of the PEEM (detailed electric schematics of the voltage generator unit are presented in appendix B). The remote controlled voltage generator was integrated on a standard 19" rack unit and installed in the PEEM high voltage rack. A schematic sketch of the unit is shown in Fig. 2.16, where the central part of the unit is an Atmel microcontroller (AT-MEGA324P), which handles the communication with

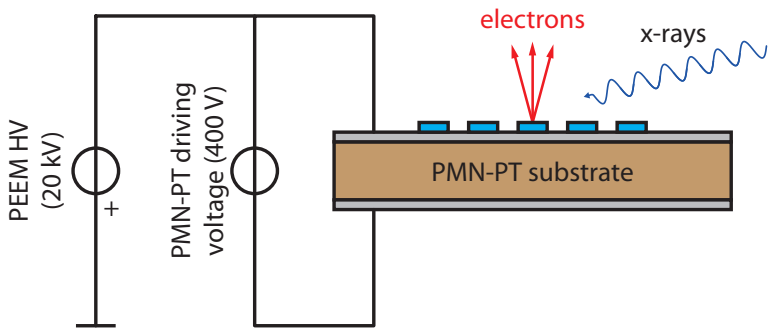

Figure 2.15: Sketch of the electrical connections employed for the application of an electric field across piezoelectric substrates inside the PEEM high voltage environment. The top electrode of the sample was always kept at the PEEM high voltage, thus allowing for imaging both with and without an electric field applied across the piezoelectric substrate.

the control computer and controls the other units.

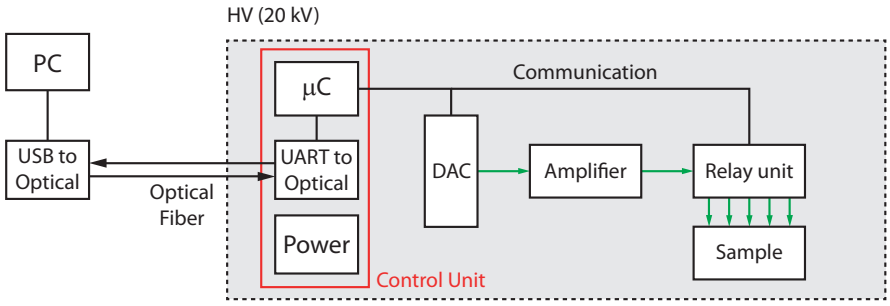

Figure 2.16: Sketch of the voltage generator inserted in the PEEM HV environment. The voltage generator is inserted into the HV environment of the PEEM, and it is controlled from outside with a computer connected via an optical fiber connection. The voltage generator itself is composed of a microcontroller unit, which handles the communications to the external computer (UART protocol) and to the DAC and relay units (SPI protocol). The DAC unit generates voltages in the range of ± 10 V, amplified to a range of ± 400 V from a commercial amplifier unit. The voltage is then applied to the sample holder with a relay unit, which can disconnect the voltage generator from the sample holder when this is not in use. The unit is protected against discharges by suppressor diodes.

The voltage to be applied to the sample is generated by a 12-bit DAC (Microchip Technology MCP4921) operating in the bipolar regime, outputting voltages in the range of ± 10 V. The generated voltage is then amplified to voltages up to ± 400 V with a commercial amplifier unit (APEX PA94), and then applied to the sample. In order to avoid damage to the electronics due to electric discharges in the PEEM, a relay unit was also implemented, allowing to disconnect the sample from the voltage generator when it is not in use. As an additional

protection, all the contacts to the sample holder were connected to the local ground of the HV rack (i.e. 20 kV) with specific electrostatic discharge protection diodes (fast suppressor diodes).

The microcontroller is equipped with a UART serial port, which is employed to communicate with the control computer located outside of the HV rack. The communication between these two devices is carried out by an optical fiber connection, allowing for the exchange of data between the two devices without an electrical connection. The microcontroller also communicates with the DAC through an serial peripheral interface, and controls directly the relay units through the general purpose input-output pins of the microcontroller. For the XMCD-PEEM measurements carried out at the Swiss Light Source, a voltage generator developed by the Paul Scherrer Institut [41], with a similar concept as the one described here, was employed.

2.3 Magneto-Optical Kerr Effect (MOKE)

To determine the magnetic properties of a continuous thin film, it is a common practice to employ the Magneto Optic Kerr Effect (MOKE), thanks to its relatively simple construction and operation, and to its relatively low costs. The MOKE was discovered after the magnetic circular dichroism effect at the end of the 19^{th} century by John Kerr [42]. The MOKE is based on the fact that, when a magnetized material is illuminated by linearly polarized light, the reflected light from the magnetized material will be polarized at a different angle with respect to the polarization of the original beam [33, 43]. By measuring the rotation angle of the polarization of the reflected light, it is then possible to determine the magnetic properties of the material illuminated by the polarized light.

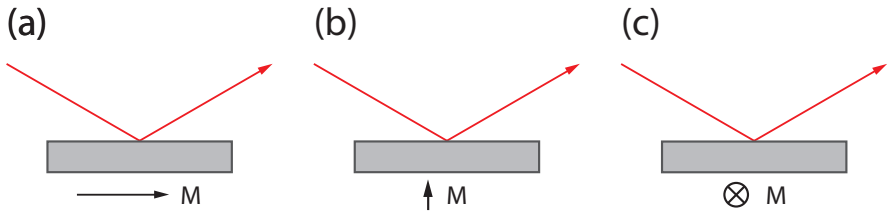

Figure 2.17: Sketch of the different operation regimes of reflective MOKE, depending on the relative orientation of the magnetic field vector **M** of the material and of the plane of incidence of the probing light (coincident with the plane of the page). (a) Longitudinal MOKE; (b) Polar MOKE; (c) Transverse MOKE.

Linearly polarized light can be described as an equal combination of left and right polarized light; the interaction between circularly polarized light and the material causes a rotation of the charges in the material. Opposite chiralities of the circular polarization will cause a rotation of the charges in the material in opposite directions. If the material is magnetized,

a spin polarization is present, giving rise, due to the spin-orbit interaction, to a different refractive index for the two opposite chiralities of the circular polarization. The interaction of the two opposite chiralities of the circular polarization that constitute the linearly-polarized light with the material will give rise to a phase difference between the two chiralities, resulting in a linearly-polarized reflected beam with a rotated polarization plane. The magnitude of the rotation of the polarization plane can then be related to the magnetization in the material [3].

As shown in Fig. 2.17, there are three different operation regimes of MOKE, defined by the different orientations of the magnetic field and the plane of incidence of the probing light [44]:

Longitudinal MOKE , where the magnetic field is parallel to the plane of incidence and parallel to the sample surface

Polar MOKE , where the magnetic field is parallel to the plane of incidence and normal to the sample surface

Transverse MOKE , where the magnetic field is normal to the plane of incidence and parallel to the sample surface

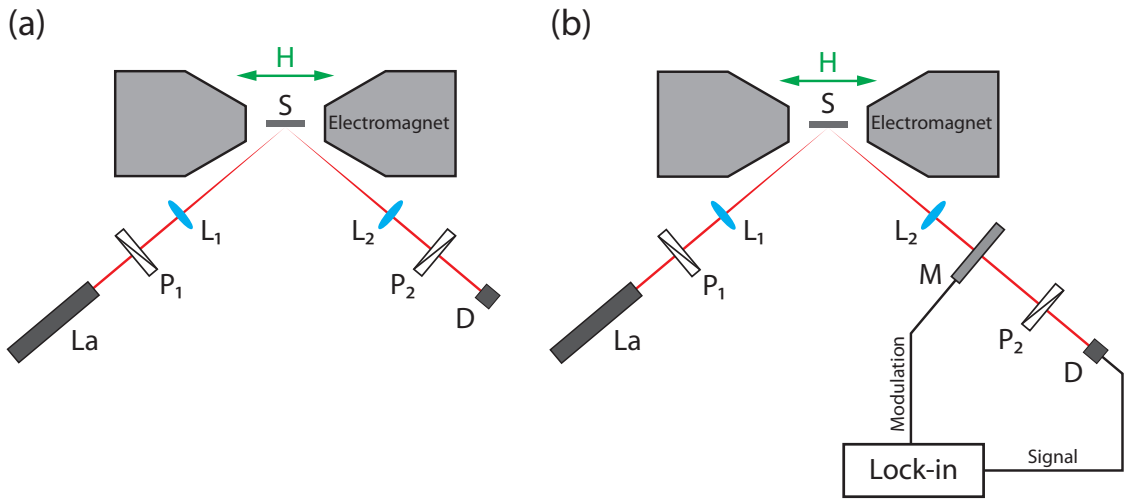

Figure 2.18: (a) Sketch of a basic longitudinal MOKE setup. La is the laser, S is the sample, P_1 and P_2 are two polarizers set at 90° with respect to each other, L_1 and L_2 are two lenses employed to focus the beam onto the sample and re-parallelize the beam after the reflection, and D is a photon detector. The polarization of the laser light lies in the direction perpendicular to the page. (b) Sketch of a longitudinal MOKE setup with an additional optical component M, which modulates the polarization of the laser beam. The modulation is driven by a lock-in amplifier, which then processes the signal acquired by the detector D.

The information depth of the reflective MOKE technique is given by $l_{\text{prob}} \simeq \lambda/(4\pi\beta)$, where λ is the wavelength of the probing light and where β is the imaginary part of the

refractive index n of the material [45]. For metallic materials, the probing depth of MOKE is on the order of 20 nm in the visible region.

For the work presented in this thesis, a longitudinal MOKE setup, a sketch of which is shown in Fig. 2.18(a), has been employed. In this setup, the magnetic field lies in the plane of incidence of the probing light, and it is possible to measure the component of the magnetization vector **M** of the material parallel (or anti-parallel) to the externally applied field **H**. By changing the orientation of the sample with respect to the applied magnetic field, it is possible to employ this technique to measure the in-plane magnetic anisotropies of the sample, as shown in Chapter 3.

2.3.1 Improvement of the signal to noise ratio by modulating the polarization

As shown in Fig. 2.19(a), the acquisition of a MOKE signal with the setup shown in Fig. 2.18(a) allows for the detection of the hysteresis loop of the material. However, the signal-to-noise ratio can be improved. Sources of noise in the acquired signal have many different origins, such as the 50 Hz noise arising from the connection of the instruments to the electrical net.

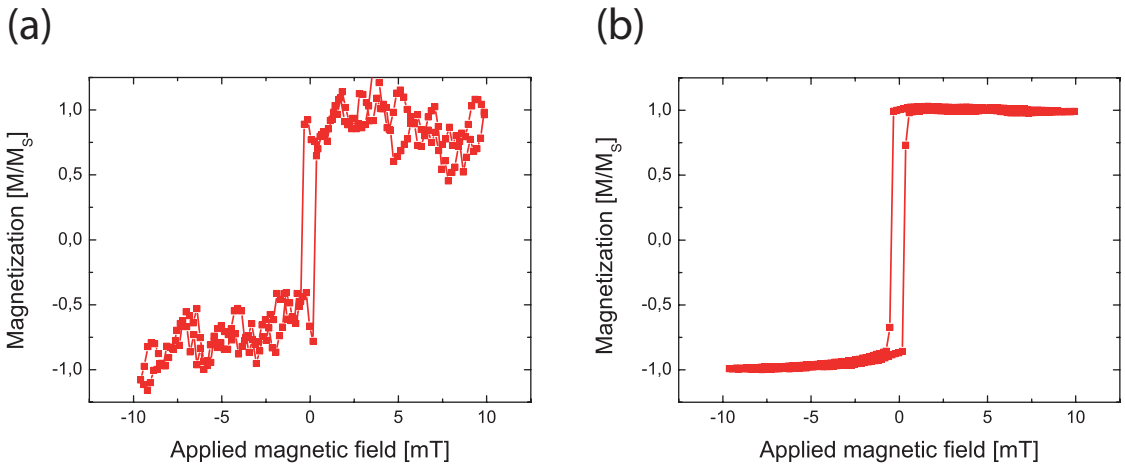

Figure 2.19: Example of a typical MOKE signal acquired with different setups on a 20 nm thick $Co_{0.2}Fe_{0.6}B_{0.2}$ continuous film. (a) Signal acquired with the setup shown in Fig. 2.18(a), with no modulation of the polarization; (b) Signal acquired with the setup shown in Fig. 2.18(b), with a modulation of the polarization combined with a lock-in amplifier.

It is possible to substantially improve the signal-to-noise ratio of the acquired MOKE signal, as shown in Fig. 2.19(b), by periodically modulating the probing light in combination with the use of a lock-in amplifier, as schematically sketched in Fig. 2.18(b).

For the work presented in this thesis, a Faraday cell modulator [46] has been employed to

modulate the intensity of the probing light. This optical element is composed of a glass tube inserted in an electromagnet, where an alternating magnetic field is applied to cause a rotation of the polarization of the probing light due to the Faraday effect [33]. As the modulation occurs, as shown in Fig. 2.18(b), before the light crosses the analyzing polarizer, the rotation of the polarization induced by the Faraday cell results in a modulation of the intensity of the light detected by the detector. By employing a lock-in amplifier to drive the Faraday cell and to filter the acquired signal, the rotation of the polarization due to the interaction of the probing light with the magnetic material can then be determined with a higher signal-to-noise ratio, as can be observed in Fig. 2.19(b) in comparison with Fig. 2.19(a).

Chapter 3

XMCD imaging of nanostructured ferromagnetic Heusler compounds

Among the various magnetic materials of interest for applications in the field of spintronics, Heusler compounds are particularly interesting due to theoretical calculations predicting a number of interesting properties, such as half-metallicity, large magneto-optical constants and shape memory effects [47]. Heusler alloys are named after Fritz Heusler, who discovered and studied this class of materials in the first decade of the 20^{th} century [48, 49]. The compound discovered by him was Cu_2MnAl, exhibiting a ferromagnetic order even though its constituent elements do not exhibit a ferromagnetic order if taken singularly [48, 49].

Two classes of Heusler compounds exist: *Half-Heusler* and *Full-Heusler* (or simply *Heusler*) compounds. Half-Heusler compounds are characterized by the chemical formula XYZ, where the X and Y atoms are typically cations, and the Z atom is an anion [47]. These materials exhibit a crystalline lattice composed of three superimposed *fcc* lattices, each occupied by the X, Y and Z atoms, with the absence of an inversion center symmetry [47, 50]. Full-Heusler compounds, which will be the focus of this chapter, are characterized by the chemical formula X_2YZ, where the X and Y atoms are transition metals, and the Z atom is a main group element [47]. Similarly to the Half-Heusler compounds, the Full-Heusler compounds exhibit, as schematically sketched in Fig. 3.1, a crystalline lattice composed of four superimposed *fcc* lattices, each occupied by the X, Y and Z atoms [47, 48].

Most of the physical properties of the Heusler compounds can be predicted by analyzing the number of valence electrons of the compound [47, 51]. This property of the Heusler compounds allows, by an appropriate selection of the constituents of the Heusler compound (i.e. the X, Y and Z atoms), one to tailor the properties of these materials to the required applications. In particular, a number of Heusler compounds exhibit magnetic properties ranging from the antiferromagnetic order (e.g. Fe_2VSi has an antiferromagnetic order [52]) to the ferromagnetic order with half-metallic behavior (e.g. Co_2MnSi has a half-metallic behavior [53]).

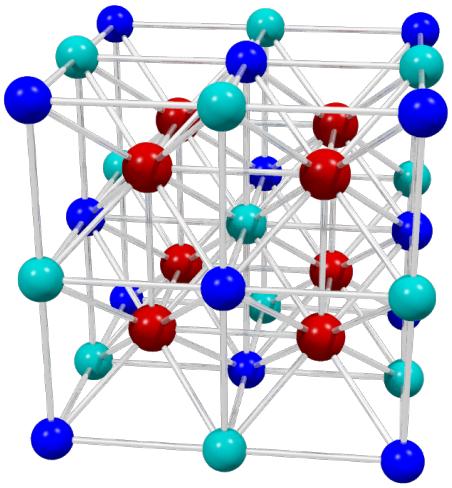

Figure 3.1: Sketch of a Heusler compound of the form X_2YZ. Image courtesy of A. Kronenberg.

This vast range of tailorable magnetic properties makes Heusler compounds of great interest for spintronic applications (e.g. for current-induced domain wall motion [54], multiferroic applications [55], and many others [47]).

The application of this intriguing class of materials for spintronic applications requires the determination of their magnetic properties in relevant conditions, such as in nanostructured thin films. In particular, the determination of magnetic properties such as the magnetic domain and domain wall configurations is of great importance to assess the prospect for use in devices.

In this chapter, the experiments aimed at the determination of the magnetic properties of nanostructured geometric elements fabricated out of thin Fe_2CrSi (FCS) and Co_2MnGa (CMG) Heusler compound films will be described.

FCS is an interesting Heusler compound for applications in spintronic devices, due to a combination of a relatively low saturation magnetization and a high spin polarization, both of which predicted by *ab-initio* calculations [56,57]. In particular, a spin polarization of $P \simeq 0.98$ and a saturation magnetization of $M_s \simeq 4 \times 10^5$ A m^{-1} (i.e. 1.98 μ_B/f.u.) were predicted. Thanks to these predicted properties, combined with a Curie temperature of 630 K [57], this compound would be particularly interesting for applications in current-induced domain wall motion systems, as the spin-torque efficiency of the material is proportional to P/M_s [58].

CMG is also an interesting Heusler compound for applications in spintronic devices. Even though this material does not exhibit half-metallic properties (i.e. a spin polarization of $P \simeq 0.44$ has been theoretically predicted [59], and a spin polarization of $P \simeq 0.55$ has been measured for this material at room temperature [59]), the use of CMG for spintronic applications has raised interest, due to the higher resistance to oxidation of CMG if compared

to other Co-based Heusler compounds (thanks to the use of Ga as the main group element in the Heusler compound) [60], and to its high crystalline order [61].

The chapter is organized as follows: first, the growth, structuring, and characterization of the magnetic properties of continuous FCS and CMG thin films will be described. Then, the results of the XMCD-PEEM imaging experiments carried out on nanostructured elements fabricated out of the FCS and CMG thin films will be presented, along with a description of the main results of the characterization of these materials.

3.1 Deposition and patterning thin FCS and CMG films

The FCS thin film samples were grown[1] with a thickness of 35 nm by DC magnetron sputtering on $MgAl_2O_4$ (001) substrates, with a 3 nm-thick Fe_2VSi buffer layer. The FCS films were then annealed at a temperature of 500 °C for 30 minutes. As shown in Fig. 3.2, x-ray diffraction (XRD) scans carried out in the $\theta - 2\theta$ and ϕ modes allow for the observation that the FCS films grow heteroepitaxially on the $MgAl_2O_4$ substrates with an $L2_1$ order (after annealing), and that they grow with an in plane orientation rotated by 45° with respect to the substrate: the [100] direction of the FCS is oriented along the [110] direction of the substrate [16]. The growth of a Fe_2VSi buffer layer between the substrate and the FCS thin films does not affect the magnetic properties at room temperature of the FCS, as Fe_2VSi is an antiferromagnetic Heusler compound with a Néel temperature between 123 and 196 K [52, 62].

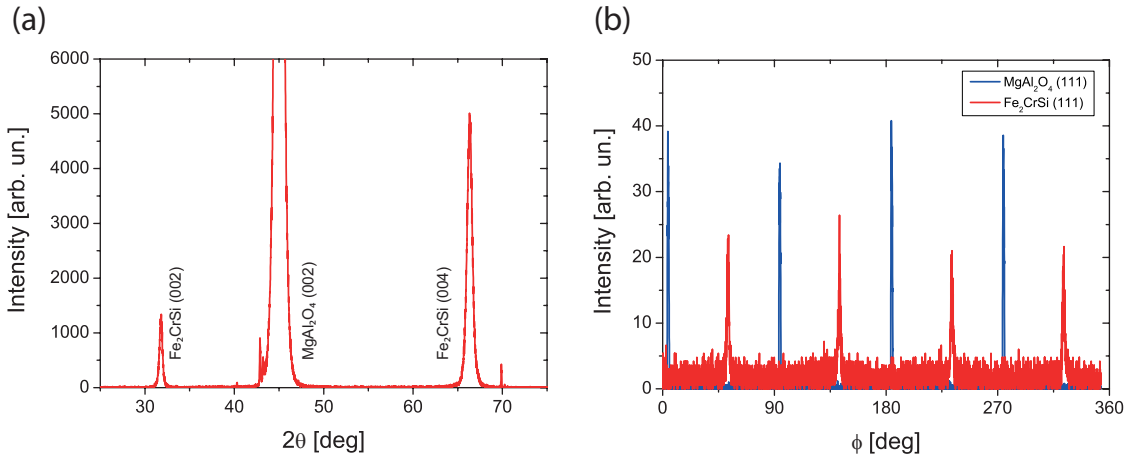

Figure 3.2: (a) θ - 2θ scan of a 35 nm thick FCS thin film sample; (b) ϕ scan acquired at the (111) peak of the FCS. It is possible to observe a clear four-fold symmetry for the FCS thin film, and an in-plane rotation of 45° of the FCS with respect to the $MgAl_2O_4$ substrate. Image adapted from Ref. [16].

[1]The FCS thin films were grown by T. Miyawaki at the University of Nagoya.

The CMG thin films were grown[2] with a thickness of 30 nm by RF sputtering directly on MgO (001) substrates. The CMG thin films exhibit a B2 crystalline order, which, after an annealing of 5 minutes at 550 °C, evolves into an $L2_1$ order [60]. This was observed by *in-situ* reflection high-energy electron diffraction measurements and by *ex-situ* XRD scans, shown in Fig. 3.3. Moreover, it is possible to observe, from the XRD scans, that the CMG crystal grows with its [100] direction along the [110] direction of the MgO (001) substrate, i.e. oriented at 45° with respect to the substrate.

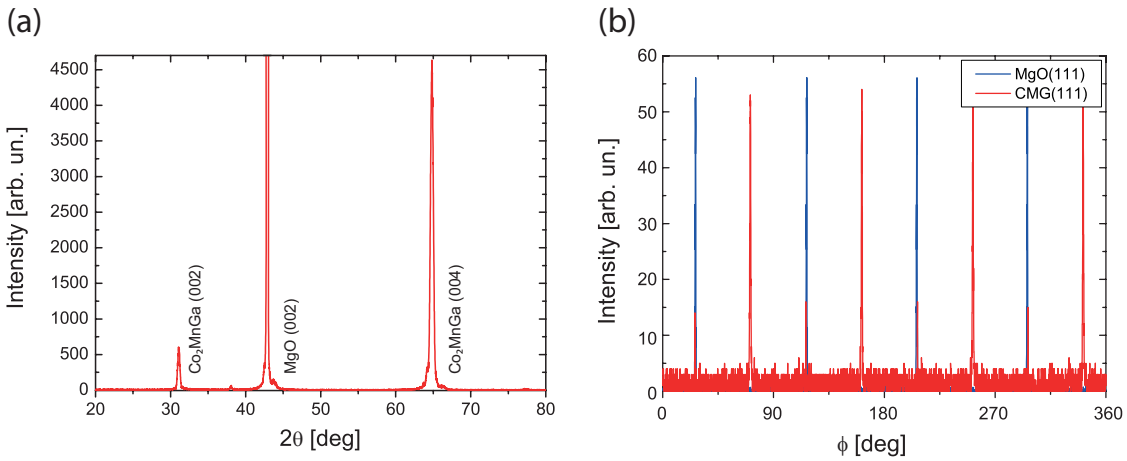

Figure 3.3: (a) θ - 2θ scan of a 30 nm thick CMG thin film sample; (b) ϕ scan acquired at the (111) peak of the CMG. It is possible to observe a clear four-fold symmetry for the CMG, and an in-plane rotation of the CMG with respect to the MgO.

Magnetometry measurements, carried out with superconducting quantum interference (SQUID) and vibrating sample magnetometry measurements allowed for the determination of the saturation magnetization of both the FCS and CMG thin film samples. The saturation magnetization for the FCS thin film samples was determined to be $M_s \simeq 4.1 \times 10^5$ A m^{-1}, while the saturation magnetization for the CMG thin film samples was measured to be $M_s \simeq 6 \times 10^5$ A m^{-1}.

After characterizing the properties of the continuous films, nanostructured elements of different sizes and geometries were fabricated on top of the FCS and CMG films by FIB lithography. This processing technique allowed, as shown in Fig. 3.4, for the fabrication of well-defined and magnetically isolated nanostructured elements.

[2]The CMG thin films were grown by A. Kronenberg at the university of Mainz.

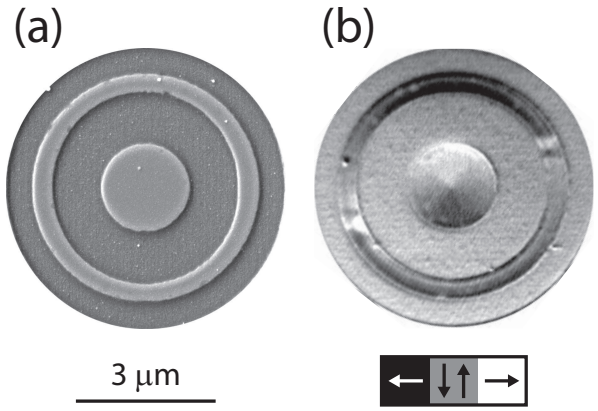

Figure 3.4: (a) SEM micrograph of a FIB nanostructured CMG Heusler alloy sample; (b) Corresponding XMCD-PEEM image, showing a clear magnetic separation between the different nanostructures. The milling depth was determined, from atomic force microscopy measurements, to be of about 30 nm.

3.2 Anisotropy characterization with MOKE

In this section, the results of the angle-dependent MOKE magnetometry measurements of the continuous FCS and CMG thin films will be presented. The Stoner-Wohlfarth model, presented in detail in section 1.4, has been employed for the estimation of the magnitude of the anisotropy constants of the two ferromagnetic Heusler compounds.

3.2.1 MOKE magnetometry of continuous FCS thin films

Angle-dependent hysteresis loops of the thin FCS films were acquired by longitudinal MOKE magnetometry at the University of Nagoya [16]. From the acquired loops, shown in Fig. 3.5, the angular dependence of the remanent magnetization M_{R} (normalized to the value of M_{S}) was determined. A qualitative analysis of this angular dependence allows for the observation that this material exhibits an in-plane magneto-crystalline anisotropy given by the combination of a four-fold anisotropy (with its easy axes along the [100] and [010] directions of the FCS) and of an uniaxial anisotropy (with its easy axis along the [110] direction of the FCS).

The Stoner-Wohlfarth model can be employed to estimate the ratio between the uniaxial and four-fold anisotropy constants by fitting the angular dependence of the coercive field (Fig. 3.5) with the magnitude of the anisotropy constants as a fitting parameter. In particular, the fitting is carried out by solving Eq. (1.27) for $\theta = \theta_0$ at no externally applied magnetic field as function of the angle ϕ between the applied magnetic field and the anisotropy axes. In the case of the FCS thin films here analyzed, the condition, at the remnant state, given by Eq.

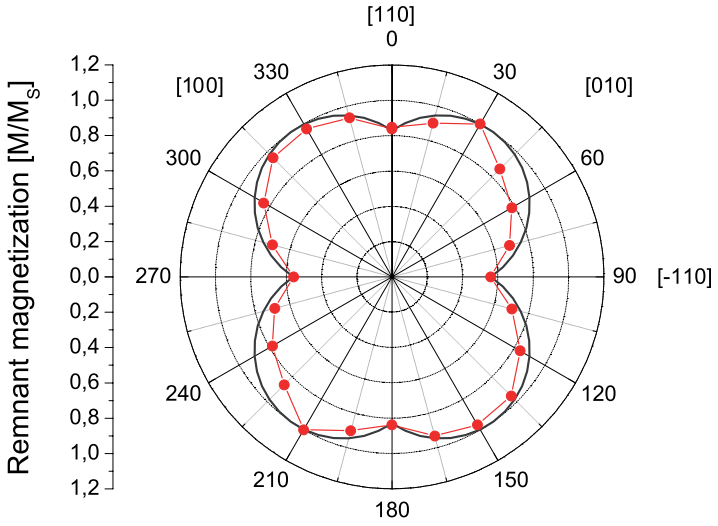

Figure 3.5: Angular dependence of the remnant magnetization (normalized to M_s) of a 35 nm thick FCS film. It is possible to observe that the FCS exhibits a four-fold magnetic anisotropy, with the easy axes along the [100] and [010] directions, and a uniaxial anisotropy, with the easy axis along the [110] direction. The points from 180° to 360° have been mirrored from the measured points from 0° to 180°. The dark gray curve indicates the result of the fitting of the remnant magnetization with the Stoner-Wohlfarth model assuming a value for the ratio between the four-fold anisotropy constant K_1 and the uniaxial anisotropy constant K_u of the FCS thin films of $K_1/K_u \simeq 2.75$. Image adapted from Ref. [16].

(1.27) may be written as follows:

$$\left.\frac{\partial f}{\partial \theta}\right|_{H=0,\,\theta=\theta_0} = K_u \sin(2(\theta_0-\phi)) + \frac{1}{2}K_1 \sin(4(\theta_0-\phi-\pi/4)) = 0. \tag{3.1}$$

The angle convention adopted in Eq. (3.1) is the same depicted in Fig. 3.5: $\phi = 0$ indicates the [110] direction, along which the easy axis of the uniaxial anisotropy is pointing, and $\phi = \pi/4$ indicates the [010] direction, along which one of the two easy axes of the four-fold anisotropy is pointing. The different orientation of the uniaxial and four-fold anisotropy axes has been taken into account in Eq. (3.1) by observing that $\phi_c = \phi + \pi/4$.

By solving Eq. (3.1) for $\theta = \theta_0(\phi)$, it is possible to fit the experimentally-determined data with the Stoner-Wohlfarth model. Being $M_\mathrm{R} = M_\mathrm{s}\cos(\theta_0)$, it is possible to fit the experimentally-determined M_R (normalized to M_s) with $\cos(\theta_0(\phi))$. As the condition $\theta = \theta_0$ that solves Eq. (3.1) depends on the parameter $K = K_1/K_u$, the fitting of the angular-dependence of M_R was carried out with K as fitting parameter. As shown by the continuous line in Fig. 3.5, a reasonable fit can be obtained for $K \simeq 2.75$. The differences between the angular dependence of the remnant magnetization determined with the Stoner-Wohlfarth model and the experimentally determined data can be attributed to the generation of magnetic

domain walls at the remnant state, which are a limiting factor for the Stoner-Wohlfarth model.

The exact magnitude of the two anisotropy constants can then be found by fitting the reversible part of the single hysteresis loops with the Stoner-Wohlfarth model, using the value of K_u as fitting parameter (where K_1 is expressed as $K_1 = KK_u$). As shown in Fig. 3.6, it is possible to fit the reversible part of the experimentally-acquired hysteresis loop if a value of $K_u = 125 \pm 20$ J m^{-3} is assumed for the uniaxial anisotropy constant. Thus, the MOKE magnetometry measurements of the continuous FCS thin films allowed for the determination of a uniaxial anisotropy $K_u = 125 \pm 20$ J m^{-3} along the [110] direction, and of a four-fold anisotropy $K_1 = 350 \pm 50$ J m^{-3} along the [100] and [010] directions.

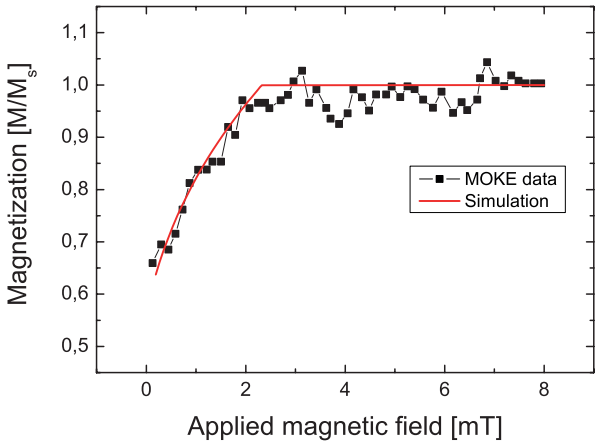

Figure 3.6: Fitting of the reversible part of the hysteresis loop of a 30 nm thick FCS film sample along the [$\bar{1}$10] direction of the FCS thin film with the Stoner-Wohlfarth model, considering the existence of a four-fold anisotropy with its easy axes along the [100]/[010] crystallographic directions of the FCS thin film and a uniaxial anisotropy with its easy axis along the [110] direction of the FCS thin film. The fitting yields a value for K_1 on the order of 350 J m^{-3} and a value for K_u on the order of 125 J m^{-3}.

As will be shown in section 3.2.2 and further explained in section 3.4.1, the direction of the four-fold anisotropy easy axes for the FCS thin films is along the [100]/[010] axes, in contrast with what was observed for Co-based Heusler compounds (such as the CMG thin films also analyzed in this work), where the four-fold anisotropy easy axes point along the [110] and [$\bar{1}$10] directions. As this difference is not due to the presence of the Fe_2VSi buffer layer (thin FCS films grown directly on $MgAl_2O_4$ substrates were analyzed as well and yielded similar results [16]), a possible explanation for such difference could be due to the fact that the Fe and Cr atoms occupy the Wyckoff 8c and 4a sites [16]. Moreover, the presence of a uniaxial anisotropy, albeit of a lower magnitude than the four-fold anisotropy, is not strictly expected from symmetry arguments. The origin of such additional uniaxial anisotropy was interpreted as being due to a miscut in the $MgAl_2O_4$ substrates [16].

3.2.2 MOKE magnetometry of continuous CMG thin films

Angle-dependent longitudinal MOKE magnetometry measurements were carried out on the continuous CMG thin films with the MOKE setup described in section 2.3. In Fig. 3.7, the angular dependence of the coercive field and of the remnant magnetization of the CMG thin films is shown. By a qualitative analysis of the data shown in Fig. 3.7, it is possible to observe that the thin CMG films exhibit a four-fold anisotropy with its easy axes pointing along the [110] and [$\bar{1}$10] directions of the CMG thin films.

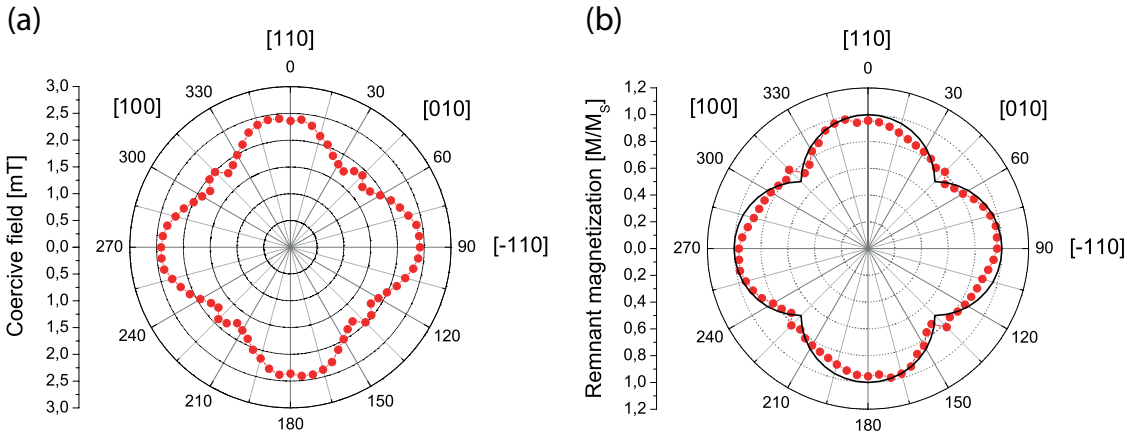

Figure 3.7: MOKE anisotropy loops of a 30 nm thick CMG film, showing the angular dependence of (a) the coercive field and (b) the remnant magnetization. The CMG exhibits a four-fold magnetic anisotropy, with the easy axes along the [110] and [$\bar{1}$10] directions. The points from 180° to 360° have been mirrored from the points between 0° and 180°. The black line in (b) indicates the fitting of the remnant magnetization with the Stoner-Wohlfarth model, assuming a four-fold magnetic anisotropy with the easy axes along the [110] and [$\bar{1}$10] directions.

As it is possible to observe from Fig. 3.7 and as expected from symmetry considerations, no uniaxial anisotropy contribution was determined from the MOKE magnetometry measurements. Thus, the fitting of the angular dependence of the remnant magnetization, shown in Fig. 3.7 , does not yield any quantitative information about the magnitude of the anisotropy constant of the CMG (i.e. for $K_u << K_1$, equation (3.1) is verified for trivial values of θ_0). Similarly to what observed for the FCS thin films, the differences between the measured angular dependence and the one predicted by the Stoner-Wohlfarth model can be attributed to the formation of magnetic domains at the remnant state.

By fitting the reversible part of the measured hysteresis loops with the Stoner-Wohlfarth model it is possible, as shown in Fig. 3.8, to obtain a reasonable fit of the experimental data for a four-fold anisotropy constant of $K_1 \simeq 1500 \pm 150$ J m^{-3}, lying within the expected values for the magneto-crystalline anisotropy of Co-based Heusler alloy thin film materials [54].

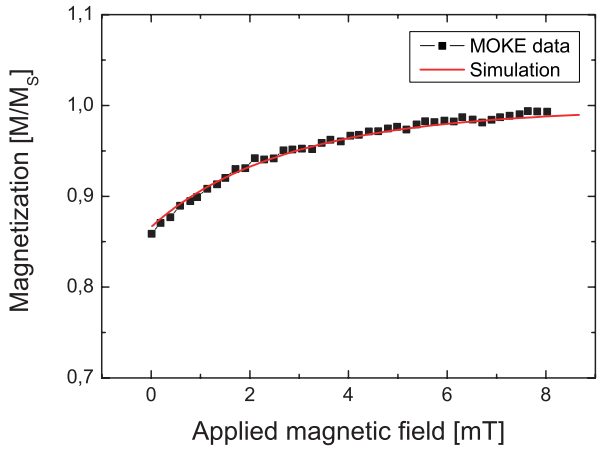

Figure 3.8: Fitting of the reversible part of the hysteresis loop of a 30 nm thick CMG film with the Stoner-Wohlfarth model, considering the existence of a four-fold anisotropy axis with its easy axes along the [110]/[$\bar{1}$10] directions of the CMG thin film. The experimental data points were acquired with MOKE magnetometry at an angle of 30° with respect to the [110] direction. It was chosen not to fit the reversible part of the hysteresis loop along the [100] (or the [010]) direction of the FCS due to the higher-than-expected value of the coercive field along the hard axes of the CMG. The fitting yields a value for K_1 on the order of 1.5 kJ m^{-3}.

It is also possible to observe, in Fig. 3.7(a), that if an external magnetic field is applied along the [100] or [010] directions of the CMG thin film, the coercive field is higher than what would be expected if only the contribution of a four-fold anisotropy term were to be considered. This is also observed for the remnant magnetization, as shown in Fig. 3.7(b). This behavior for the angular dependence of the coercive field has already been observed for other Heusler alloy materials [63,64], and was explained as being due either to a checkerboard domain configuration taking place during the reversal process of the magnetization [63], or to magnetic frustration effects taking place at certain orientations [64]. To ascertain exactly the mechanism behind the increased coercive field of the continuous CMG thin films, the spatially resolved domain configuration during the reversal process should be determined. However, this measurement is not possible with XMCD-PEEM imaging, due to the impossibility of carrying out PEEM imaging with applied magnetic fields.

3.3 Imaging of the magnetic configuration of nanostructured Heusler alloy thin films

In this section, the outcome of the XMCD-PEEM imaging of nanostructured FCS and CMG thin films will be presented.

3.3.1 Nanostructured FCS thin films

As shown in section 3.2.1, the MOKE magnetometry measurements of continuous FCS thin films reveal the existence of a four-fold anisotropy and of a uniaxial anisotropy, which will influence the magnetic configuration of nanostructured elements of this material due to the conflicting contributions of the magneto-crystalline and shape anisotropies. In this section, the results of high resolution XMCD-PEEM imaging[3] of the nanostructured elements with different geometries fabricated out of FCS continuous films will be presented.

The magnetic configuration of the nanostructures was initialized with a demagnetizing stage prior to the insertion of the samples in vacuum. Moreover, the samples were mounted on a sample holder equipped with an *in-situ* electromagnet, capable of generating magnetic fields up to about 50 mT along a single axis (either parallel or perpendicular to the direction of the probing x-rays), which allows for the *in-situ* manipulation of the magnetization of the nanostructured elements. The magnetic nanostructures were imaged at the remnant state after their saturation with a magnetic field of about 50 mT applied along the [110] direction of the FCS, chosen to be parallel to the direction of the incoming x-rays (by mounting the sample with the [100] direction of the substrate parallel to the x-ray direction) [16].

As shown in Fig. 3.9, the nanostructured FCS squares exhibit magnetic states ranging from the Landau flux-closure state to the magnetic S-state [16, 67]. In particular, as shown in Fig. 3.9(a), if the edges of the nanostructured squares are pointing along the [110] and $[\bar{1}10]$ directions of the FCS (i.e. along the hard axes of the four-fold anisotropy) shape and magneto-crystalline anisotropy are competing against each other, giving rise to Landau flux-closure states for the squares with smaller edges, where shape anisotropy is energetically dominant, and to magnetic S-states for the squares with larger edges, where the magneto-crystalline anisotropy contribution is dominant. For the square nanostructures with their edges pointing along the [110] and $[\bar{1}10]$ directions of the FCS, a critical size of 2 μm for the square edge, where the contributions of shape and magneto-crystalline anisotropy to the magnetic free energy are comparable, was found.

As shown in Fig. 3.9(b), if the nanostructured squares are fabricated with their edges parallel to the [100] and [010] directions of the FCS (i.e. along the easy axes of the four-fold anisotorpy), the magnetic configuration of the nanostructured elements falls into the Landau flux-closure state also for larger structures. Being the [100] and [010] directions of the FCS the easy axes of the four-fold anisotropy, the existence of Landau flux-closure states also for larger squares can be understood, as both shape and magneto-crystalline anisotropy favor the formation of the Landau flux-closure state.

As shown in Fig. 3.10, the nanostructured FCS disks exhibit flux-closure magnetic states,

[3]The imaging of the nanostructured FCS thin films was carried out at the SIM (X11MA) beamline at the Swiss Light Source [65, 66].

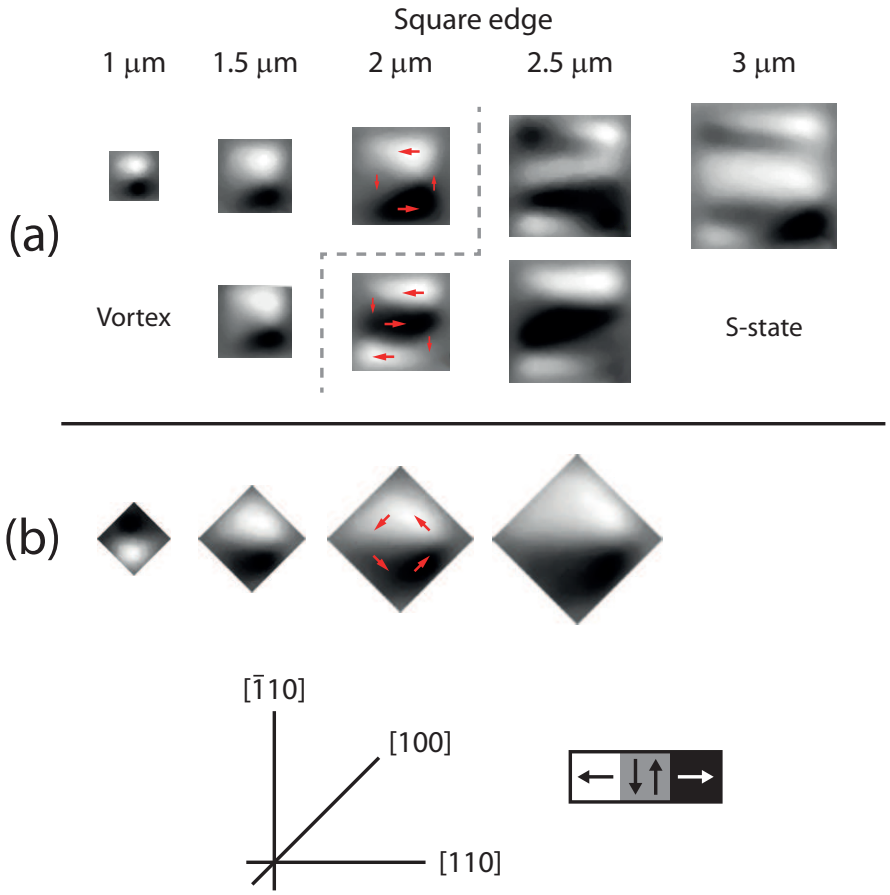

Figure 3.9: XMCD-PEEM images of nanostructured squares on a 30 nm thick FCS film, showing the interplay of the different contributions to the total magnetic energy. (a) XMCD-PEEM images of nanostructured squares of different geometric dimensions with their edges along the [110] and [$\bar{1}$10] directions of the FCS, showing Landau flux-closure states for edge dimensions below 2 μm, and magnetic S-states for edge dimensions above 2 μm; (b) XMCD-PEEM images of nanostructured squares of different geometric dimensions with their edges along the [100] and [010] directions of the FCS, showing a Landau flux-closure state. The grayscale bar indicates the direction of the magnetic contrast in the images, and the red arrows indicate the direction of the magnetization in the single domains. The gray dashed line in (a) indicates the boundary for the square geometry between the vortex and S-state regions. Image adapted from Ref. [16].

ranging from vortex states to S-states [16,67]. In particular, for small diameters of the nanostructured disks, the magnetic configuration of the FCS disks is a vortex state while, for larger disks, the magnetic S-state is observed [16].

The magnetic configuration of the nanostructured FCS disks was also analyzed at the remnant state after the application of a constant magnetic field of different intensities. As

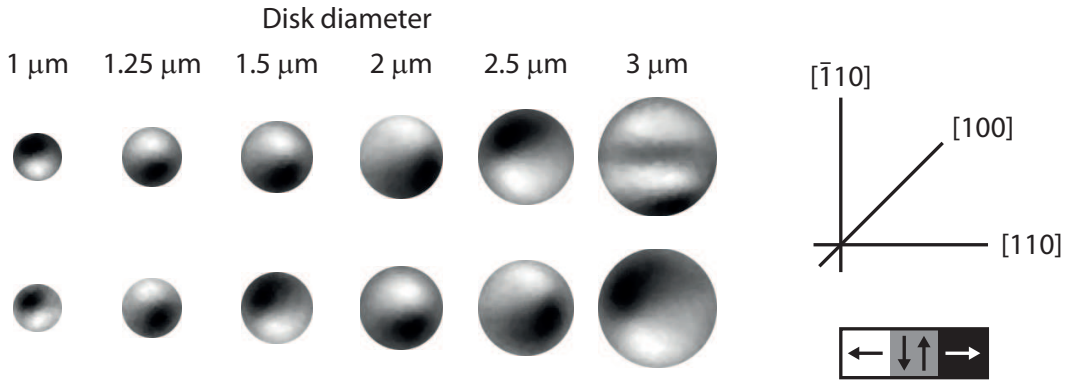

Figure 3.10: XMCD-PEEM images of nanostructured disks on a 30 nm thick FCS film, showing the interplay of the different contributions to the total magnetic energy. For disk diameters below 3 μm, a magnetic vortex state is observed, while at disk diameters of 3 μm a coexistence of vortex and S-states is observed. The grayscale arrow indicates the direction of the magnetic contrast in the images. Image adapted from Ref. [16].

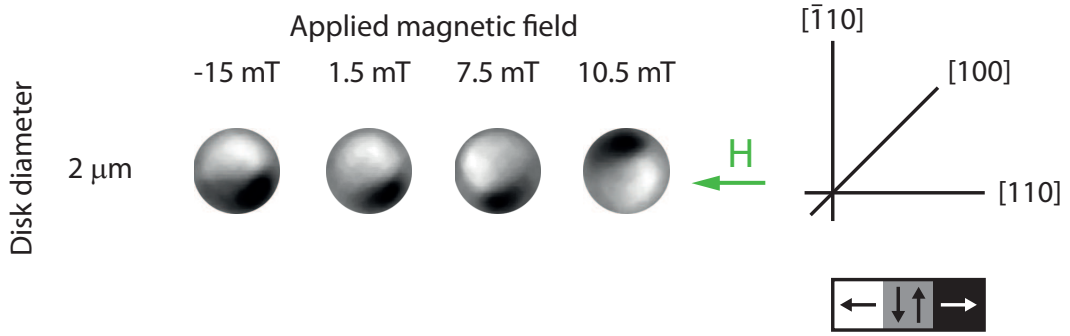

Figure 3.11: XMCD-PEEM images of a 2μm diameter disk on a 30 nm thick FCS film at the remnant state after the application of an external magnetic field (indicated by the green arrow in the figure). A reversal of the chirality of the vortex can be observed for the nanostructured disk after the application of a 10.5 mT external magnetic field. The grayscale arrow indicates the direction of the magnetic contrast in the images. Image adapted from Ref. [16].

shown in Fig. 3.11, the nanostructured disks initialized in the magnetic vortex state exhibit, after the application of magnetic fields with different magnitudes (in the direction marked by the green arrow in Fig. 3.11), a different position for the vortex core. The displacement of the vortex core, caused by the application of the magnetic field, was still detectable at the remnant state due to the presence of pinning sites on the FCS thin films, created by local variations of the magneto-crystalline anisotropy (triggered, in turn, by unavoidable variations of the local sample quality during the growth).

As it is possible to observe in Fig. 3.11, after the application of a magnetic field of 10.5 mT, the magnetic vortex state of the 2 μm wide ring reversed its chirality. This change in the

vortex chirality was interpreted, as will be further explained in section 3.4.1, with the field-induced expulsion of the vortex core from the nanostructured disk, causing the nucleation of another vortex core (of opposite chirality) upon the relaxation of the magnetic field.

3.3.2 Nanostructured CMG thin films

As shown in section 3.2.2, the MOKE magnetometry characterization of the continuous CMG thin films reveals the existence of a four-fold anisotropy. In this section, the results of XMCD-PEEM imaging[4] of nanostructured elements of different geometries fabricated out of continuous CMG thin films will be presented.

Similarly to the nanostructured FCS thin films, the magnetic configuration of the nanostructures was initialized with the help of a demagnetizing stage prior to the insertion into the vacuum, and an *in-situ* electromagnet, integrated on the PEEM sample holder, was employed to apply magnetic fields up to about 50 mT along the [110] direction of the CMG thin films. Likewise, for the FCS nanostructured thin films, XMCD-PEEM imaging was carried out at the remnant state.

As shown in Fig. 3.12, the nanostructured CMG squares fall into Landau flux closure states [67]. This occurs independently from the relative orientation of the squares with respect to the easy axes of the four-fold anisotropy.

A similar magnetic configuration was observed when imaging the nanostructured CMG disks. As shown in Fig. 3.13, the nanostructured CMG disks tend to fall into a magnetic vortex state also for larger dimensions of the nanostructured elements.

Finally, as shown in Fig. 3.14, the magnetic configuration of nanostructured CMG rings was imaged as well. In this case, the magnetic configuration of the ring nanostructures was initialized by the application of a magnetic field along the $[1\bar{1}0]$ direction. As shown in Fig. 3.14, the CMG ring nanostructures fall predominantly in the magnetic onion state [70], with a head-to-head and a tail-to-tail magnetic domain wall. The only exception was observed for wide rings with a high curvature (inner diameter of 2 μm and width of 1 μm), where the magnetic configuration of the ring fell into a vortex state [70]. For the nanostructured rings initialized in the onion state, only vortex domain walls [70] were observed, as shown in Fig. 3.14.

The XMCD-PEEM imaging experiments carried out on the nanostructured CMG thin films showed that the magnetic configuration of the nanostructured elements is dominated by shape anisotropy, as will be discussed in more detail in section 3.4.2.

Most of the analyzed CMG thin film samples exhibited the magnetic states shown in Figs. 3.12, 3.13, and 3.14. However, for some of them, a different magnetic configuration for larger

[4]The imaging of the nanostructured CMG thin films was carried out at the Nanospectroscopy beamline at Elettra [68] and at the CIRCE beamline at ALBA [69].

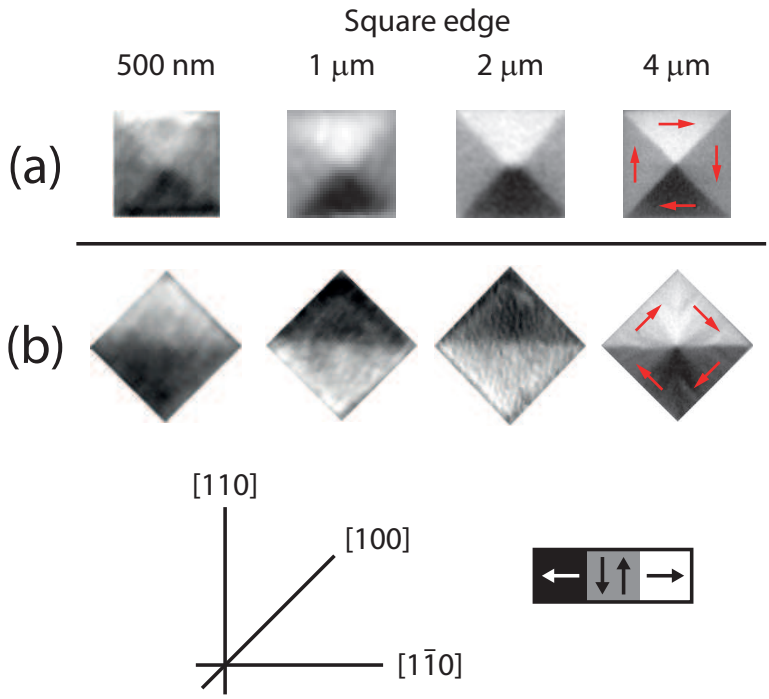

Figure 3.12: XMCD-PEEM images of nanostructured squares on a 30 nm thick FCS film, showing the interplay of the different contributions to the total magnetic energy. (a) XMCD-PEEM images of nanostructured squares with their edges along the [110]/[1$\bar{1}$0] directions of the CMG, showing simple Landau flux closure states for smaller dimensions, and the coexistence of Landau and more complicated flux-closure states for larger dimensions; (b) XMCD-PEEM images of nanostructured squares with their edges along the [100]/[010] directions of the CMG, showing Landau flux closure states both for smaller and larger dimensions of the square edge. The grayscale arrow indicates the direction of the magnetic contrast in the images, and the red arrows in the images indicate the direction of the magnetization in the single magnetic domains.

nanostructures was observed, as shown in Fig. 3.15. For these samples, the observed magnetic states are a clear signature state for the presence of an additional uniaxial anisotropy [67], with its easy axis pointing along the [1$\bar{1}$0] direction. As for the FCS thin films, the presence of this additional uniaxial anisotropy is not expected from symmetry considerations, and was related, as further explained in section 3.4.2, to a miscut of the MgO substrate.

3.4 Results and discussion

In this section, a brief interpretation of the magnetic configurations of the nanostructured FCS and CMG thin film samples imaged with XMCD-PEEM will be given.

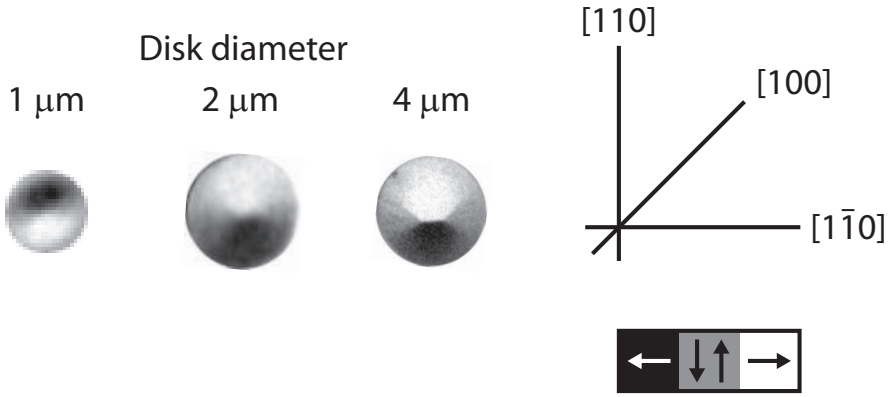

Figure 3.13: XMCD-PEEM images of nanostructured disks on a 30 nm thick CMG film, showing the interplay of the different contributions to the total magnetic energy. For disk diameters below 2 μm a magnetic vortex state is observed. For disk diameters of 2 μm and above, instead, the coexistence of distorted vortex states and flux closure states resembling the states observed for the larger CMG squares shown in Fig. 3.12 is observed. The grayscale bar indicates the direction of the magnetic contrast in the images.

3.4.1 FCS thin films

As shown in section 3.1, thin FCS films were heteroepitaxially grown on $MgAl_2O_4$ (001) substrates by DC magnetron sputtering. After growth and annealing, the thin FCS films exhibit an $L2_1$ order, as confirmed by XRD analyses, shown in Fig. 3.2. Magnetometry measurements of the continuous FCS films allowed for the determination of a saturation magnetization $M_s \simeq 4.1 \times 10^5$ A m^{-1} [16], close to the predicted value of 4×10^5 A m^{-1} [56]. Angle-dependent MOKE magnetometry measurements of the continuous FCS thin films allowed, as shown in Fig. 3.5, to observe that the FCS thin films exhibit a combination of a uniaxial and of a four-fold anisotropy [16]. With the help of the Stoner-Wohlfarth model, it was possible to estimate the magnitude of the two anisotropy constants, given by $K_1 = 350 \pm 50$ J m^{-3} for the four-fold anisotropy and $K_u = 125 \pm 20$ J m^{-3} for the uniaxial anisotropy.

As already mentioned in section 3.2.1, the four-fold anisotropy term is expected in this material from symmetry considerations. However, also a uniaxial anisotropy term, not expected from symmetry considerations, was observed for this material. This term can, however, be explained by considering the unavoidable miscut of the crystalline substrate on which the films were grown, which leads to the generation of step-edges on the surface of the substrate, which can then explain this additional uniaxial anisotropy [71, 72].

The easy axes of the cubic anisotropy point along the [100] and [010] directions of the FCS thin films, while the uniaxial anisotropy term exhibits an easy axis along the [110] direction of the FCS thin films. The direction of the anisotropy axes of the FCS thin films is different

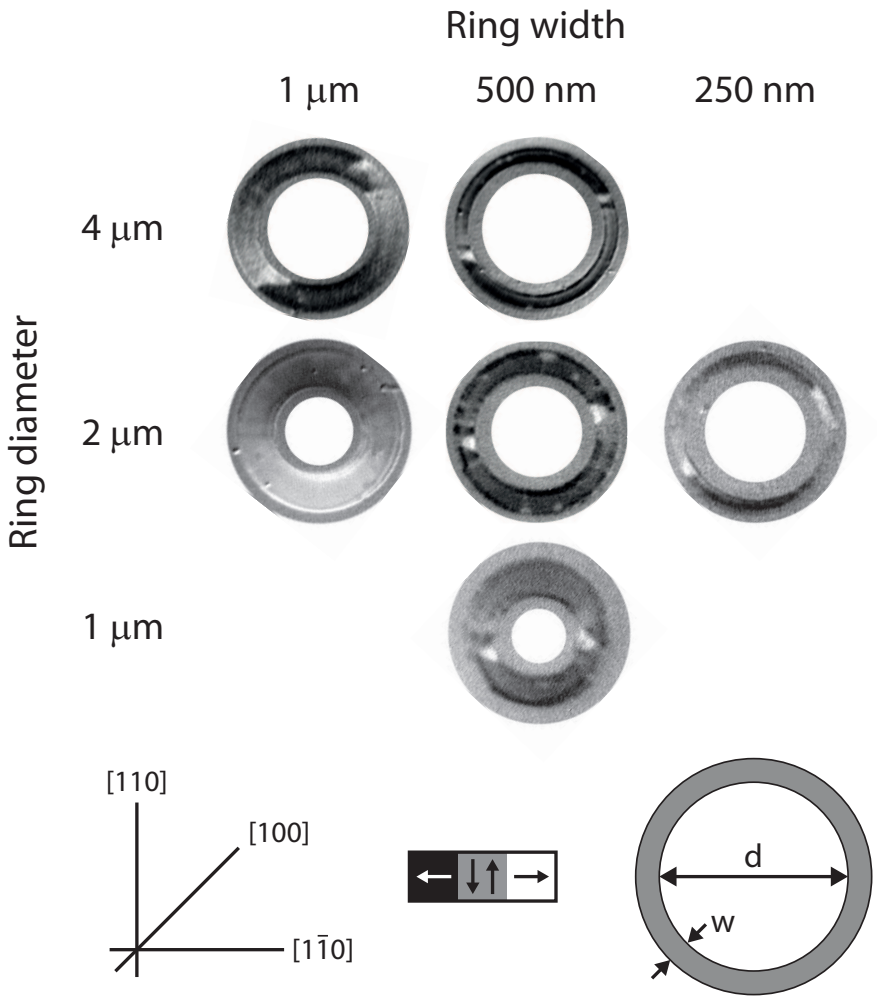

Figure 3.14: XMCD-PEEM images of nanostructured rings on a 30 nm thick CMG film with different diameters d and widths w, after initialization with a magnetic field applied along the [1$\bar{1}$0] direction of the CMG thin film. The nanostructured rings are in a magnetic onion state for smaller ring curvatures and a vortex state for larger curvatures. For the rings that fall into the onion state, the vortex domain wall is the prevalent spin structure. No preferential orientation of the domain walls with respect to the crystallographic axes of the CMG was observed. The grayscale bar indicates the direction of the magnetic contrast in the images.

with respect to what was observed for Co-based Heusler alloys (also including the CMG thin films analyzed in this work), where the direction of the easy axes lies along the [110] and [1$\bar{1}$0] directions of the Heusler alloy. Although further studies aimed at determining the origin of this different orientation of the easy axes for the cubic anisotropy term are necessary, an interpretation for the different orientation of the easy axes of the FCS cubic anisotropy (with respect to Co-based Heusler alloys) is that this different orientation could arise from the combination of Fe atoms at the Wyckoff 8c sites and of Cr atoms at the Wyckoff 4a sites [16].

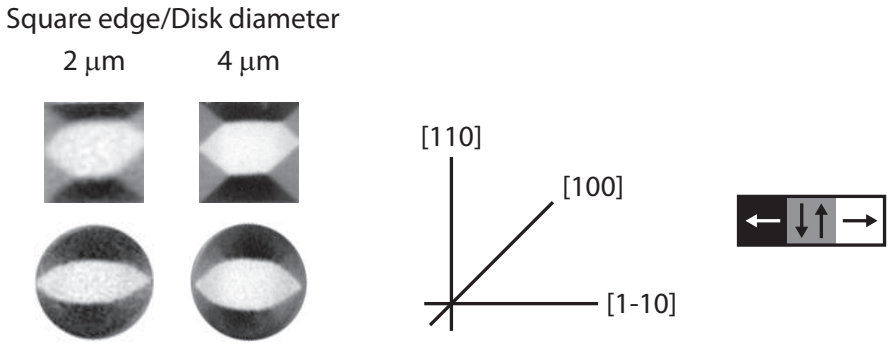

Figure 3.15: XMCD-PEEM images of nanostructured squares and disks on a 30 nm thick CMG film showing a uniaxial anisotropy contribution, which can be identified from the magnetic configuration of the nanostructured elements.

However, further analyses, which lie outside of the scope of this work, have to be carried out in order to ascertain the exact origin of this different orientation of the anisotropy axes.

As expected, the XMCD-PEEM imaging experiments, shown in section 3.3.1, reveal that the magnetic configuration of the nanostructured FCS elements is determined by the combination of the contributions arising from magneto-crystalline and shape anisotropy. In order to ascertain the relative magnitude of these contributions, different geometries, including square and disk nanostructures, were analyzed.

The imaging of the structured square elements reveals a competition between shape and magneto-crystalline anisotropy: as shown in Fig. 3.9, the orientation of the edges of the square nanostructures with respect to the directions of the easy axes of the magneto-crystalline anisotropy has a strong impact on the magnetic configuration of the structured elements. In fact, if the edges of the square nanostructures are pointing along the easy axis of the four-fold anisotropy (i.e. along the [100] and [010] directions), it is possible to observe a Landau flux-closure state for all the investigated structures. This does not occur if the edges of the square structures are pointing along the hard axes of the four fold anisotropy (i.e. along the [110] and [$\bar{1}$10] directions): in this case, the nucleation of magnetic S-states is observed for the larger squares. In particular, a "phase" boundary between the Landau flux-closure state and the magnetic S-states can be observed for a square with edge dimensions of about 2 μm (i.e. smaller squares fall into a Landau flux-closure state, while the larger squares fall into a magnetic S-state). This different behavior of the magnetic configuration of the square nanostructures depending on their orientation can be interpreted as follows: when the square edges point along the easy axes of the cubic anisotropy term, both shape and magneto-crystalline anisotropy favor a magnetization pointing along the edges of the square nanostructures. If the square edges are, instead, pointing along the edges of the hard axes of the cubic anisotropy term, the shape and magneto-crystalline anisotropy terms compete against each-other, leading to

different states when shape anisotropy (i.e. for smaller structures, where the Landau flux-closure state is observed) or the magneto-crystalline anisotropy (i.e. for larger structures, where magnetic S-states are observed) are dominant.

As shown in Fig. 3.10, the analysis of the magnetic configuration of the nanostructured FCS disks shows that the competition between magneto-crystalline and shape anisotropy also plays a role. Magnetic vortex states were observed for small disk diameters (i.e. for disk diameters smaller than about 3 μm), whereas larger disks fell into a magnetic S-state. The presence of these magnetic vortex states was not observed in other ferromagnetic Heusler compounds (such as $Co_2FeAl_{0.4}Si_{0.6}$ [73]). The first interpretation on the origin of these states could be the lower magnitude of the magneto-crystalline anisotropy of the FCS if compared to other Co-based Heusler compounds such as $Co_2FeAl_{0.4}Si_{0.6}$, exhibiting both a higher saturation magnetization and magneto-crystalline anisotropy constant [73].

The application of a magnetic field to disk nanostructures that were initialized in the vortex state causes a displacement of the vortex core. If a sufficiently high field is applied, the vortex core will be expelled from the nanostructure (i.e. a displacement larger than the radius of the disk nanostructure is induced by the application of the magnetic field). The magnitude at which the expulsion of the vortex core takes place for the nanostructured FCS thin films was determined by analyzing the magnetization configuration of the nanostructured disks after the application of a magnetic field. In particular, a vortex-expulsion field of about 9.0 ± 1.5 mT was determined for the disk nanostructures with a diameter of 2 μm.

3.4.2 CMG thin films

As shown in section 3.1, thin epitaxial CMG films were grown by RF sputtering on MgO (001) substrates. After growth and annealing, the CMG thin films exhibited an $L2_1$ order, identified by *in-situ* RHEED and *ex-situ* XRD analyses, as shown in Fig. 3.3.

Magnetometry measurements of the nanostructured CMG thin films allowed for the determination of a saturation magnetization of $M_s \simeq 6 \times 10^5$ A m^{-1}, relatively close to the theoretically predicted value of $M_s \simeq 7.8 \times 10^5$ A m^{-1} [74], while angle-dependent MOKE magnetometry measurements allowed for the determination of a four-fold anisotropy with its easy axes along the [110] and [1$\bar{1}$0] directions. The magnitude of the anisotropy constant was estimated, as shown in Fig. 3.7, with the help of the Stoner-Wohlfarth model to be $K_1 = 1500 \pm 150$ J m^{-3}, of comparable magnitude to the other Co-based Heusler compounds [54].

The magnetic configuration of the nanostructured CMG thin films appears to be dominated by the sole contribution of shape anisotropy: as can be observed in Fig. 3.12, the magnetic configuration of nanostructured CMG thin films falls into the Landau flux-closure state independently from the orientation and dimension of the nanostructured squares. A

similar behavior was observed for the nanostructured CMG disks, as shown in Fig. 3.13, where only magnetic vortex states were observed. This response of the magnetic configuration of the nanostructured CMG elements indicates an unexpected behavior, which hints to the existence of an additional contribution to the magnetic free energy which is counteracting the influence of the four-fold anisotropy. Possible interpretations for this behavior could be given by the implantation of Ga atoms in the CMG nanostructures during the FIB patterning, or damages to the surface of the nanostructures induced upon the sputtering of the protective capping layer for the PEEM imaging experiments.

As shown in Fig. 3.15, for some of the investigated CMG nanostructured samples, different magnetic states were observed for the larger nanostructured elements. In particular, the states shown in Fig. 3.15 are signature states for the contribution of a uniaxial anisotropy. The uniaxial anisotropy, with its easy axis pointing along the $[1\bar{1}0]$, could not be quantified directly with magnetometry measurements, due to the removal of the capping layer. The origin of this uniaxial anisotropy component can, however, be easily explained, similarly to the analyzed FCS thin films, as being due to a miscut of the substrate.

Finally, also CMG ring nanostructures were analyzed. The magnetic configuration of these rings was initialized in the onion state [70], allowing for the analysis of the geometrical influence (i.e. ring width and local curvature) on the domain wall configuration. All of the analyzed rings that could be initialized in the onion state exhibited, as shown in Fig. 3.14, magnetic vortex walls, providing a clear indication for the lower energy of this domain wall configuration. For different thicknesses, a different magnetic domain wall could be energetically favored, as shown e.g. in Py [75, 76]. A detailed analysis of the thickness dependence of the magnetic domain walls for the nanostructured CMG thin films, which constitutes a natural step forward from the analyses presented here, was however not carried out due to the limited beamtime available.

3.5 Conclusions and summary

In this chapter, the results of the characterization of the magnetic configuration of nanostructured FCS and CMG thin films has been presented. As shown in section 3.1, high quality heteroepitaxial thin films of the Heusler compounds FCS and CMG were fabricated. As determined by XRD analyses, both the FCS and CMG thin films exhibit an $L2_1$ order after a post-deposition annealing.

Prior to their nanostructuring, both the FCS and CMG thin films were characterized by angle-resolved magnetometry measurements, as shown in section 3.2. Both materials exhibit, as expected from symmetry considerations, a four-fold anisotropy. The magnitude of the anisotropy constant was estimated with the help of the Stoner-Wohlfarth model (described

in section 1.4). For the FCS thin films, an anisotropy constant of $K_1 = 350 \pm 50$ J m^{-3} was estimated while, for the CMG thin films, an anisotropy constant of $K_1 = 1500 \pm 150$ J m^{-3} was estimated. These angle-resolved magnetometry measurements determined that the easy axes of the four-fold anisotropy of the FCS thin films point along the [100] and [010] directions of the FCS while, for the CMG thin films, the easy axes of the four-fold anisotropy point along the [110] and [1$\bar{1}$0] directions. The different orientation of the easy axes for the FCS and for the CMG thin films was interpreted, as explained in section 3.4.1, as being due to the positions in the crystal lattice occupied by the Fe and Cr atoms of the FCS.

In addition to the expected four-fold anisotropy, also an additional uniaxial anisotropy was observed for both the FCS and the CMG thin films. For the analyzed FCS thin films, a uniaxial anisotropy of $K_u = 125 \pm 20$ J m^{-3} with its easy axis along the [110] direction was observed. For the CMG thin films, no additional uniaxial anisotropy was observed for the samples analyzed by angle-resolved magnetometry, but it was observed on some of the samples analyzed by XMCD-PEEM imaging, as shown in Fig. 3.15. The presence of this additional uniaxial anisotropy is not expected from symmetry considerations, but it can be explained, for both the FCS and CMG thin film samples, as being due to the unavoidable miscut of the substrate, leading to the formation of step-edges on the surface of the substrate, responsible for this additional uniaxial anisotropy.

Parameter	FCS	CMG
Substrate	$MgAl_2O_3$	MgO
Thickness [nm]	35	30
M_s [A m^{-1}]	4.1×10^5	6×10^5
K_u [J m^{-3}]	125 ± 20	0
EA K_u	[110]	-
K_c [J m^{-3}]	350 ± 50	1500 ± 150
EA K_c	[100]/[010]	[110]/[1$\bar{1}$0]

Table 3.1: Summary of the main parameters for the FCS and CMG thin films described in this chapter. EA indicates the directions of the easy axes of the uniaxial and cubic anisotropies in the material.

Both the FCS and CMG samples were nanostructured by FIB lithography, as shown in section 3.1, and the magnetic configuration of the fabricated nanostructures was investigated by XMCD-PEEM imaging.

XMCD-PEEM imaging on the nanostructured FCS and CMG thin films evidenced the nucleation of magnetic states given by a combination of the contributions of shape and magneto-crystalline anisotropy. For the nanostructured FCS thin film samples, magnetic configurations determined by the competing influence of shape and magneto-crystalline anisotropy were ob-

served.

In conclusion, nanostructured elements of the ferromagnetic Heusler compounds FCS and CMG were lithographically fabricated, and imaged by XMCD-PEEM, and the main results of the analyses presented in this chapter are shown in Table 3.1. The magnetic nanostructures fabricated out of these two materials exhibit magnetic states where shape anisotropy plays an important role in the definition of the magnetic state, thus allowing for the tailoring of the magnetic configuration of these materials by the sole selection of the geometry of the nanostructured elements. The possibility of reliably manipulating the magnetic configuration of these nanostructured elements is the first step towards the use of these materials in more advanced experiments, and in eventual applications in spintronics.

The results presented in this chapter regarding the characterization of the magnetic configuration of nanostructured FCS Heusler compound thin films were published in the *Journal of Applied Physics* [16], while the results regarding the characterization of the magnetic configuration of nanostructured CMG Heusler compound thin films have been collected in a manuscript which has been accepted for publication within the *New Journal of Physics* [77].

Chapter 4

Control of the magnetization in Ni nanostructures fabricated on piezoelectric substrates

As described e.g. in Ref. [78] and schematically shown in Fig. 4.1, materials such as ferromagnets or ferroelectrics, where a spontaneous order of the magnetization or of the electric polarization respectively arises, are defined as *ferroic* materials. Materials that exhibit more than one ferroic order (e.g. ferromagnetic and ferroelectric orders) coupled with each other (e.g. a modification of the magnetization of the material changes its electric polarization) are, instead, defined as *multiferroics*. The multiferroic coupling can occur, as marked by the orange arrows in Fig. 4.1, between the electric and magnetic orders (magneto-electric coupling), between the electric and elastic orders (piezoelectric coupling) and between the elastic and magnetic order (magneto-elastic coupling).

Such multiferroic materials, especially those exhibiting a magneto-electric coupling (i.e. both ferroelectric and ferromagnetic orders), are good candidates for achieving a current-less manipulation of the magnetic order, which would find numerous applications in magnetic storage devices.

A substantial amount of research has been aimed, in the last years, at discovering materials exhibiting both ferroelectric and ferromagnetic order. However, up to today, only rare cases of such magneto-electric multiferroic materials have been discovered, and for most of them, the coupling occurs only at low temperatures [79], or between the ferroelectric polarization and the (anti-)ferromagnetic order [80,81]. It is, however, possible to combine different ferroic materials into a system that, as a whole, can exhibit multiferroic properties. Such combinations of different ferroic materials showing multiferroic coupling are defined as *artificial multiferroic* materials.

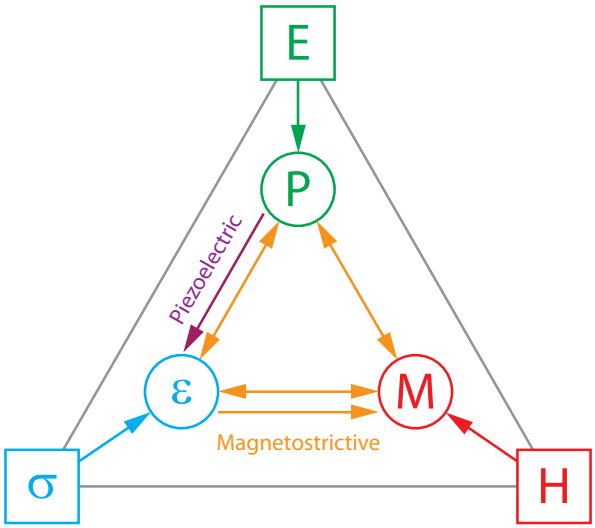

Figure 4.1: The application of an electric field E, a stress σ, or a magnetic field H can control, respectively, the ferroelectric polarization P, the strain ε and the magnetization M of a material, which form, in ferroic materials, ferroelectricity, ferroelasticity and ferromagnetism respectively. If more than one ferroic order are present and coupled with each other, the material, or combination of materials, is defined as a multiferroic [78]. If a piezoelectric and a magnetostrictive material are combined, it is possible to achieve the control of the magnetization of the magnetostrictive material through an electric field (i.e. a strain is generated by the application of an electric field across the piezoelectric material, which then influences, through the magneto-elastic coupling, the magnetic configuration of the magnetostrictive material).

In this chapter, an artificial multiferroic material exhibiting magneto-electric multiferroic properties (i.e. it is possible to manipulate the magnetization by the application of an electric field) will be presented. This artificial multiferroic system is composed of a piezoelectric material with a magnetostrictive material. As schematically shown in Fig. 4.1, by combining these two materials it would be possible, by applying an electric field across the piezoelectric material, to manipulate the magnetization of the magnetostrictive material. The coupling between the magnetic and electric orders is achieved, for this artificial multiferroic system, by employing the piezoelectric material to generate a strain (caused by the application of an electric field across the piezoelectric material), which then influences the magnetic configuration of the magnetostrictive material.

The specific artificial multiferroic system analyzed in the experiments presented in this chapter consists of Ni nanostructures fabricated on top of a piezoelectric substrate. The chapter is organized as follows: first, a brief introduction on the magnetostrictive effect will be given. Then, the fabrication process of the magnetic nanostructures will be described, followed by the presentation and discussion of the experimental results obtained by XMCD-

PEEM imaging.

4.1 Magnetostriction and magneto-elastic coupling

The magnetostrictive effect was experimentally discovered in the late 19^{th} century [82]. In these early experiments, it was observed that the application of a uniform magnetic field to ferromagnetic materials (in this particular case, iron and steel bars) causes a deformation of these materials. In the experiments described in Ref. [82], a shrinking and elongation of the Fe bars upon the application of a magnetic field were observed. Already upon its discovery, this effect was proposed for applications as actuators [82]. Some magnetostrictive materials, explicitly engineered to exhibit a strong variation of their strain state upon the application of a magnetic field (i.e. materials with a high *magnetostrictive constant*), were specifically developed for applications as actuator or sensor (e.g. $Fe_{1-x}Ga_x$, known as *Galfenol* [83]).

These materials were, thanks to their sensor and transducer applications, intensively investigated in the 1950s and 1960s. After this peak of interest in the 1950s and 1960s, research on these materials subsided, only to be recovered in recent years thanks to the new materials developments and to the new developments in sample fabrication and lithographical processing techniques, which allow for the fabrication of samples with different conditions as those available 50 years ago (e.g. nanostructured thin films) [84, 85].

The microscopic origin of the magnetostrictive effect originates from the spin-orbit coupling mechanism and from the changes in the ionic potential that the electrons experience upon the deformation of the material (i.e. the ionic potential in the Hamiltonian that describes the electrons in the material depends on the strain state of the material). A complete explanation of this effect at the microscopic scale lies beyond of the scope of this work, but it is possible to describe the effect of magnetostriction phenomenologically by introducing an additional term to the magnetic free energy density of the material, dependent from the strain condition of the magnetostrictive material, as described in more detail in section 1.2.5.

The formulation for the magnetoelastic anisotropy K_{ME} shown in Eq. (1.21) (see section 1.2.5) will be employed in the following sections for the interpretation of the experimental measurements.

4.2 Ni/PMN-PT sample fabrication

To generate the in-plane strain required to control the magnetic configuration of magnetostrictive nanostructured elements, a piezoelectric material was employed as the substrate. In particular, the relaxor ferroelectric $[Pb(Mg_{0.33}Nb_{0.66})O_3]_{(1-x)}$-$[PbTiO_3]_x$ (PMN-PT), a solid solution of two Pb-based perovskites with a composition of $x \simeq 0.32$, close to the morphotropic phase transition of PMN-PT [86], which ensures the possibility to generate sizable strains in

different directions [87], was employed as substrate. PMN-PT crystals exhibit a pseudocubic perovskite crystal structure with a lattice parameter of 4.02 Å [88], and can be employed for the generation of sizable strains in different directions by the application of an electric field across the material, depending primarily on the crystalline orientation of the substrate [87,88].

For the experiments presented in this chapter, the interest is to generate, through the magneto-elastic coupling, an uniaxial anisotropy to the magnetostrictive material with which the magnetic configuration can be manipulated. As shown in section 1.2.5, this goal can be achieved by generating a volume conserving strain variation fully lying on the surface of the magnetostrictive material. That is, it is necessary to generate an in-plane strain with one compressive component and one tensile component, perpendicular to the each other. PMN-PT can be employed as a substrate to achieve this strain configuration by cutting the crystal in the (011) orientation. In fact, for PMN-PT (011) substrates, the application of an out-of-plane electric field leads to the generation of an in-plane strain, as can be observed from the piezoelectric response curves shown in Fig. 4.2 [87].

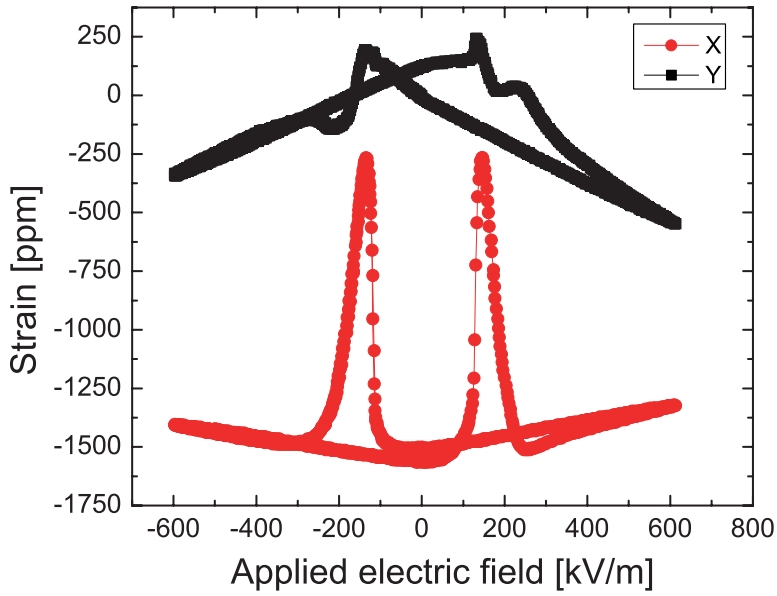

Figure 4.2: Piezoelectric response of a PMN-PT (011) crystal as function of the applied electric field. The electric field is applied across the piezoelectric crystal, in the [001] direction - defined as z - while the strain is measured along the [100] and [010] directions - defined as x and y respectively. Image adapted from Ref. [87].

As shown in Fig. 4.2, PMN-PT (011) exhibits, like other piezoelectric materials [45,88,89], an hysteretic behavior of the strain with respect to the applied electric field. Such hysteretic behavior is governed by the movement of the Ti atoms in the crystalline unit cell of the PMN-PT. For this material, there are two meta-stable positions of the Ti atom in the crystalline lattice unit cell, which can be manipulated by applying an electric field across the crystal. The

movement of the Ti atoms from one meta-stable position to the other requires the application of electric fields higher than a given threshold (defined as *coercive field* E_c), which allows for the overcoming of the potential barrier between the two meta-stable positions [89]. The crystal is *poled* when an electric field higher than the coercive field is applied to the material. The effect of the movement of the Ti atoms in the PMN-PT (011) crystal can be observed, in Fig. 4.2, as peaks in the piezoelectric response curves. It is also possible to observe in Fig. 4.2 that, once the peak in the strain-vs-electric field has been overcome (i.e. once the piezoelectric crystal has been poled in one direction), the piezoelectric response curve is linear with respect to the applied electric field, as long as the applied fields do not pole the crystal in the opposite direction (i.e. for electric fields higher than -E_c, being the crystal originally poled by the application of a "positive" electric field). Moreover, it is possible to observe that the piezoelectric response of the poled crystal is non-hysteretic, thus guaranteeing a linear and reproducible strain response of the piezoelectric crystal, which provides a simple experimental condition for determining the coupling between the applied electric field and the generated magneto-elastic anisotropy.

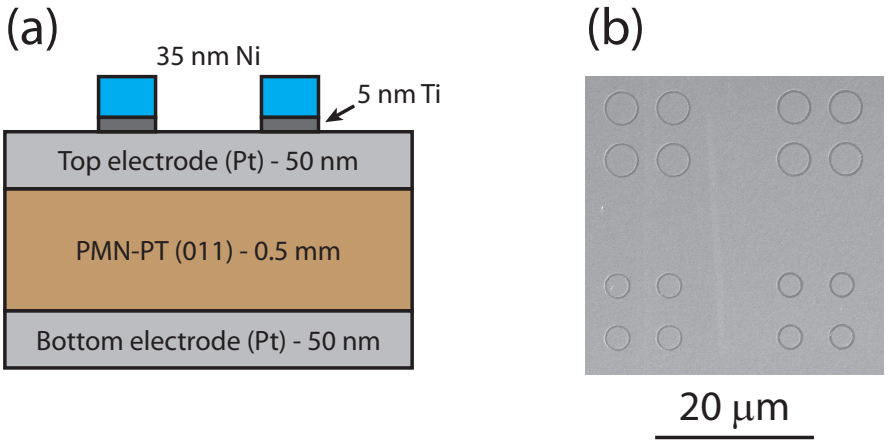

Figure 4.3: (a) Schematic overview of the sample structure, with the thickness of all the layers indicated; (b) Scanning electron micrograph of some of the Ni nanostructures fabricated on top of the PMN-PT (011) substrate. Image adapted from Ref. [90].

Nanostructured Ni elements of different geometries and sizes were fabricated on PMN-PT (011) substrates[1] by electron beam lithography followed by a lift-off step. Details about the fabrication process of the Ni nanostructured elements are given in Refs. [91, 92].

To apply the electric field along the out-of-plane direction of the PMN-PT (011) substrate, a 50 nm-thick Pt electrode was deposited on the top and bottom surfaces of the substrate prior to the fabrication of the Ni nanostructures. A sketch of the complete sample geometry

[1]The deposition and patterning of the Ni on top of the PMN-PT was carried out by a collaborating group at the University of California, Los Angeles

is shown in Fig. 4.3(a), and a scanning electron micrograph of some of the Ni nanostructures fabricated on the PMN-PT is shown in Fig. 4.3(b).

As the Ni was deposited at room temperature, i.e. well below the Curie temperature of the piezoelectric substrate, it was possible to deposit the Ni both on a virgin, un-poled substrate and on top of a substrate which had been electrically poled prior to the deposition of the Ni thin films. As will be further explained in the following sections, the choice of poling or not poling the substrate prior to the fabrication of the Ni nanostructures plays an important role in the definition of the magnetic properties of the Ni nanostructures, and on their response with respect to the application of an electric field across the piezoelectric substrate.

4.3 XMCD-PEEM imaging of Ni nanostructures on PMN-PT substrates

High resolution magnetic microscopy imaging of the Ni nanostructures fabricated on PMN-PT (011) was carried out by XMCD-PEEM imaging[2]. As can be observed in Fig. 4.4, the Ni nanostructures show a clear XMCD contrast for circularly polarized x-rays tuned at the L_3 absorption edge of Ni (i.e. an x-ray photon energy of about 852 eV).

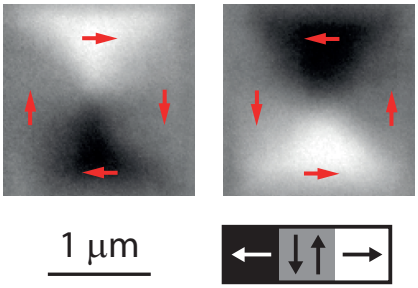

Figure 4.4: XMCD-PEEM image of 2 μm wide square Ni nanostructures fabricated on top of an un-poled PMN-PT (011) substrate acquired by tuning the circularly polarized x-rays to an energy of about 852 eV. The grayscale bar indicates the direction of the magnetic contrast in the images, and the red arrows indicate the direction of the magnetization in the single magnetic domains.

To apply the out-of-plane electric field to the PMN-PT (011) substrates, the samples were mounted onto the PEEM sample holders so that the top electrode was electrically connected with the PEEM extractor voltage (i.e. the local ground of the PEEM sample stage), while the voltage employed to drive the piezoelectric substrate was applied to the bottom electrode. The

[2]The XMCD-PEEM imaging experiments described in this chapter were performed at the SIM (X11MA) beamline at the Swiss Light Source [65, 66], and at the UE49-PGMa beamline at the synchrotron radiation facility (BESSY) of the Helmholtz Zentrum Berlin [93].

voltage employed to pole the piezoelectric substrates was generated with an *in-situ* voltage generator specifically developed for these experiments, as described in section 2.2.5.

A sketch of the sample geometry with the employed electrical connections is shown in Fig. 4.5(a), and a picture of the sample mounted on the actual sample holder is shown in Fig. 4.5(b), where it is possible to observe that the top electrode of the sample was directly contacted with the metallic cap of the PEEM sample holders.

To reset the magnetic configuration of the Ni nanostructures, an electromagnet integrated directly with the PEEM sample holder was employed to generate *in-situ* magnetic fields up to 50 mT. The Ni nanostructures were initialized in the flux-closure state with a demagnetization cycle.

In the following sections, the main results of the XMCD-PEEM imaging experiments carried out on nanostructures of various sizes and geometries fabricated both on virgin un-poled and pre-poled PMN-PT (011) substrates will be presented.

4.3.1 Ni nanostructures fabricated on un-poled PMN-PT substrates

As shown in Fig. 4.6, upon the application of a piezoelectric strain to the Ni nanostructures fabricated on un-poled PMN-PT (after an initial poling of the substrate to access the linear strain response regime), it is possible to observe a clear change of the magnetic configuration of the Ni. In particular, by comparing Fig. 4.6(a) with Fig. 4.6(c), it is possible to observe that the application of a piezoelectric strain gives rise, qualitatively, to an uniaxial anisotropy contribution (i.e. upon the application of a strain, the Ni structure switches into a single-domain state).

To interpret the experimental results with the theoretical model described in section 1.2.5, the experiments were concentrated onto the imaging of simple geometric structures, where it is also possible to easily carry out micromagnetic simulations. For this reason, the imaging experiments were carried out primarily onto 2 μm wide square Ni nanostructures such as the one shown in Fig. 4.7.

After the initialization of the nanostructures with a de-magnetization cycle, the magnetic configuration of the nanostructured Ni squares was imaged as function of different voltages applied across the piezoelectric substrate. As shown in Fig. 4.8, it is possible to observe an evolution of the magnetic configuration of the nanostructured Ni squares as function of the electric field applied across the piezoelectric substrate. In particular, the Ni nanostructured squares were initialized in a magnetic flux-closure state comparable to the Landau state [67].

As was observed in Fig. 4.6, also for the 2 μm wide Ni nanostructures the application of an electric field across the piezoelectric substrate leads to strong changes of their magnetic configuration. In particular, as can be observed in Fig. 4.8, the application of a piezoelectric strain to the Ni squares leads to a growth of the magnetic domains pointing along the

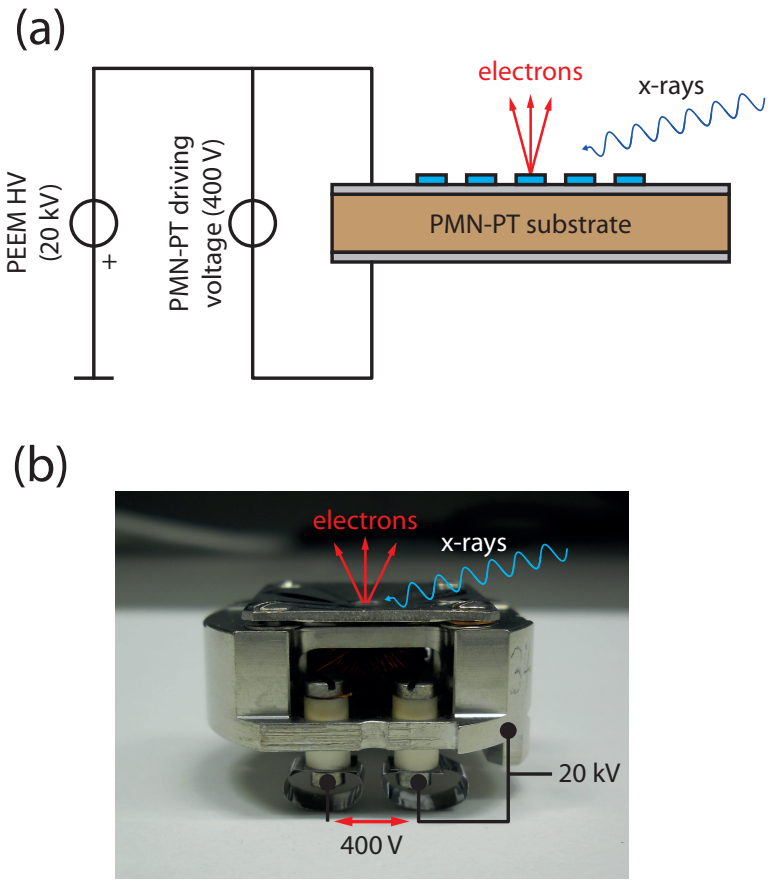

Figure 4.5: (a) Sketch of the electrical connections employed for the application of an electric field across the PMN-PT substrates inside the PEEM. The top electrode of the sample is directly contacted with the PEEM extractor voltage, while the voltage employed to drive the PMN-PT substrate was applied to the bottom electrode. This choice for the sample geometry allows for PEEM imaging both with and without an electric field applied across the piezoelectric substrate; (b) Picture of the PEEM sample holder with a Ni/PMN-PT sample mounted. The top electrode of the sample was glued with a silver colloidal solution to the metallic cap of the PEEM sample holder (electrically connected with the sample holder cartridge), while the bottom electrode was connected with one of insulated electrical connections of the PEEM sample holder. It is also possible to observe the *in-situ* electromagnet employed for initializing the magnetic configuration of the Ni nanostructures.

compressive strain direction (marked by the blue arrows in Fig. 4.8), at the expense of the domains pointing along the tensile strain direction (yellow arrows in Fig. 4.8)

Analyzing Figs. 4.6 and 4.8, it is possible to conclude that the application of a volume-conserving in-plane strain to the Ni nanostructures allows for the growth of the magnetic domains pointing along the compressive strain direction, at the expense of the domains point-

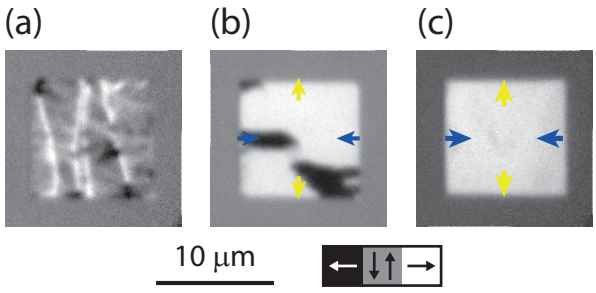

Figure 4.6: XMCD-PEEM images of a 10 μm wide Ni square as function of the electric field across the piezoelectric substrate. (a) No applied voltage. It is possible to observe a complex multidomain structure; (b) Applied electric field of 200 kV m^{-1}; (c) Applied electric field of 400 kV m^{-1}. It is possible to observe substantial changes in the magnetization of the Ni square. The grayscale bar indicate the direction of the magnetic contrast in the images, and the blue and yellow arrows indicate the direction of the compressive and tensile strain on the Ni square respectively.

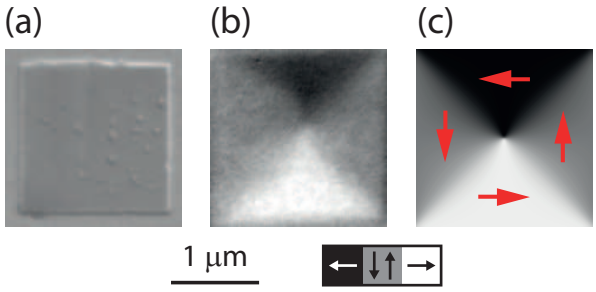

Figure 4.7: (a) SEM micrograph of a 2 μm wide nanostructured Ni square; (b) XMCD-PEEM image of the same square shown in (a), exhibiting a magnetic flux-closure state at an applied electric field of 300 kV m^{-1} across the piezoelectric substrate; (c) Micromagnetic simulation of a 2 μm wide Ni square (calculated with the parameters given in section 4.4.1), showing a good agreement with the experimental image. The red arrows indicate the orientation of the magnetic domains in (c). The grayscale bar indicates the direction of the magnetic contrast in images (b) and (c).

ing along the tensile strain direction. This provides a clear signature of the presence of a strain-induced uniaxial anisotropy contribution, with its easy axis pointing along the compressive strain direction. This qualitative observation is in agreement with the negative sign of the magnetostrictive constant of Ni [11,12,94], which implies (from Eq. (1.21)) that the uniaxial anisotropy axis points along the compressive strain direction (i.e. the contribution from the magneto-elastic free energy is minimized when the magnetization is pointing along the compressive strain axis). This agreement with the theoretical description given in Eq. (1.21), as will be shown in section 4.4.2, is also quantitative, proving that the fabrication of multi-

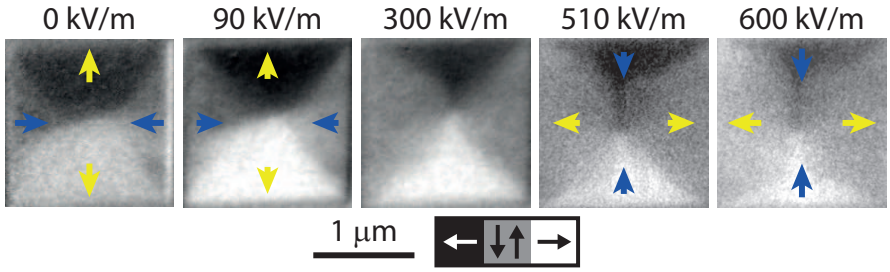

Figure 4.8: XMCD-PEEM images of a 2μm wide nanostructured Ni square as function of the electric field applied to the piezoelectric substrate (in the range from 0 to 600 kV m^{-1}). The blue and yellow arrows indicate the direction of the compressive and tensile strain on the Ni square respectively. The grayscale bar indicates the direction of the magnetic contrast in the images. Image adapted from Ref. [91].

domain nanostructures on the Ni does not appear to give rise to substantial modifications of its magnetostrictive properties with respect to bulk Ni.

By measuring different Ni squares fabricated on different un-poled PMN-PT (011) substrates, it was possible to determine the behavior of the magnetic structure of the Ni nanostructures as function of the applied strain. In order to compare the experimental results with the micromagnetic simulations (see section 4.4.1 for a description of the micromagnetic simulations carried out in this work), the area of the magnetic domains in the square Ni nanostructures pointing along either the compressive or tensile axes of the applied strain was determined as function of the electric field applied across the piezoelectric substrate. The results of such analysis, normalized to the total area of the nanostructured Ni square, are shown in Fig. 4.9. The samples were oriented so that the compressive strain was applied either parallel or perpendicular to the direction of the probing x-rays. The observed results were reproducible over all the cycles that were attempted, and the magnetic configuration for the Ni nanostructures was observed to be stable in time (at least in a timescale of about 3 months).

As can be observed in Figs. 4.8 and 4.9, the magnetic configuration of the nanostructured Ni squares falls into a symmetric Landau magnetic flux-closure state for an applied electric field of about 300 kV m^{-1} across the piezoelectric substrate. As can be further observed in Fig. 4.8(a), when the electric field applied across the piezoelectric substrate is relaxed to zero, the magnetic configuration of the Ni square nanostructures falls into a non-symmetric flux-closure state, hinting for the existence of an additional uniaxial anisotropy contribution.

The behavior of the Ni nanostructured squares fabricated on pre-poled PMN-PT shown in Figs. 4.8 and 4.9, along with an explanation of the additional anisotropy term introduced in the last paragraph will be discussed in detail in section 4.4.2, where also a comparison of the experimental results with micromagnetic simulations will be given.

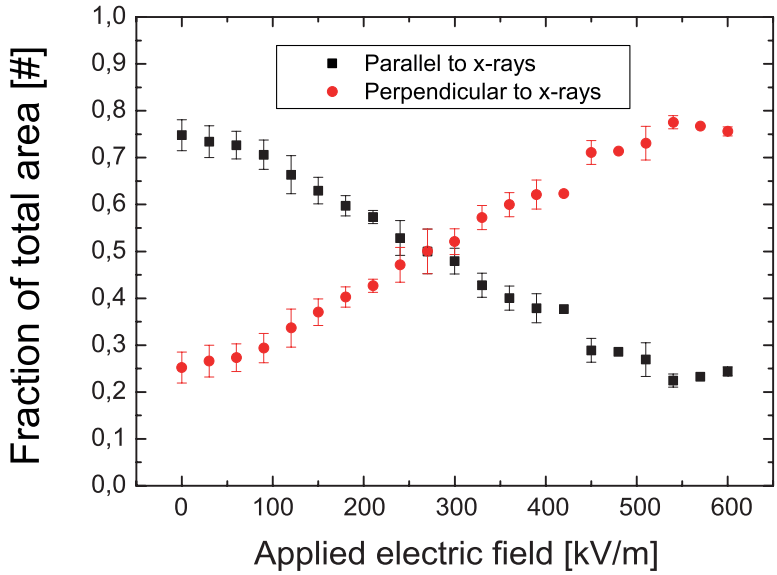

Figure 4.9: Normalized area of the magnetic domains in 2 μm wide nanostructured Ni squares pointing parallel or perpendicular to the x-rays as function of the electric field applied across the piezoelectric substrate. Refer to Fig. 4.8 for an example of the magnetic configuration of the Ni nanostructures as function of the applied field. Image adapted from Ref. [91].

4.3.2 Ni nanostructures fabricated on pre-poled PMN-PT substrates

As already explained in the previous sections, both pre-poled and un-poled PMN-PT (011) substrates were employed for the experiments described in this chapter. As already mentioned above, and as will be shown in this section, the choice of a pre-poled or un-poled PMN-PT (011) substrate for the growth of the Ni film plays an important role in the definition of the magnetic properties of the Ni, and on the response of the magnetization with respect to an electric field applied across the piezoelectric substrate [90, 91]. As shown in Fig. 4.10, the magnetic state of a nanostructured Ni square of the same thickness and geometry depends on whether the Ni was deposited on top of a pre-poled or un-poled PMN-PT substrate. In particular, by comparing Fig. 4.10(a) with Fig. 4.10(b), it is possible to observe that the nanostructured Ni square grown on top of the pre-poled PMN-PT exhibits a strong contribution to its magnetic configuration arising from an uniaxial anisotropy term (of stronger magnitude than the one observed for the Ni nanostructures fabricated on un-poled PMN-PT substrates).

This discrepancy between the behavior of the magnetic configurations of the nanostructured Ni is also observed upon the application of an electric field across the piezoelectric substrate. In particular, as shown in Figs. 4.8 and 4.9, the Ni nanostructures fabricated on un-poled PMN-PT exhibit a magnetic configuration with a "continuous" variation on the applied strain (i.e. no sudden changes of the magnetic configuration of the nanostructured elements are observed). Instead, if the Ni nanostructures are fabricated onto a pre-poled

PMN-PT substrate, as shown in Fig. 4.11, a different behavior is observed.

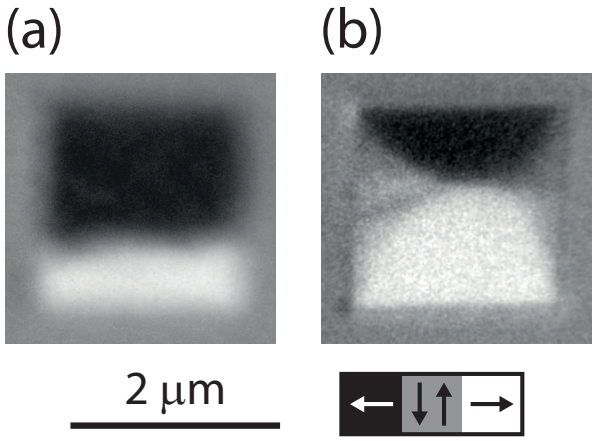

Figure 4.10: Comparison between the magnetic configuration of nanostructured Ni squares fabricated on (a) pre-poled and (b) un-poled PMN-PT substrates. The grayscale bar indicates the direction of the magnetic contrast in the images. Image adapted from Ref. [90].

The application of an electric field across the piezoelectric substrate of a magnitude less than about 340 kV m^{-1} leads, as shown in Fig. 4.11(a) and (b) to a similar behavior as what was observed for the Ni nanostructures fabricated on un-poled PMN-PT: domains pointing along the compressive strain axis grow at the expense of those pointing along the tensile strain axis. However, if an electric field with a magnitude above about 340 kV m^{-1} is applied across the pre-poled PMN-PT substrate, the magnetic configuration of the nanostructured Ni squares switches from a Landau-like flux closure pattern into a more complicated multi-domain structure, as shown in Fig. 4.11(c). These changes were, however, fully reversible with respect to the applied electric field, as shown in Fig. 4.11(d), where the relaxation of the electric field "restores" the original magnetic configuration of the nanostructured Ni squares.

This strong uniaxial anisotropy contribution arising from the growth of the Ni nanostructures on top of a pre-poled PMN-PT substrate was also observed for other geometries, as shown in Fig. 4.12. In Fig. 4.12(a), it is possible to observe a high-resolution XMCD-PEEM image of a nanostructured Ni ring of 4 μm diameter and 350 nm width, obtained after the initialization of the nanostructures with an applied magnetic field. Without additional anisotropy contributions, the initialization of the nanostructured Ni rings with a magnetic field should result in a magnetic onion state [70], as shown in Fig. 4.12(b), where a micromagnetic simulation of the expected configuration is shown. By observing the magnetic configuration shown in Fig. 4.12(b), it is also possible to observe that the magnetization of the simulated nanostructured ring follows the curvature of the ring. Instead, as can be observed in Fig. 4.12(a), this is not the case for the nanostructured Ni ring fabricated onto a pre-poled PMN-PT substrate. In fact, it is possible to observe that, due to a strong uniaxial anisotropy contribution, the

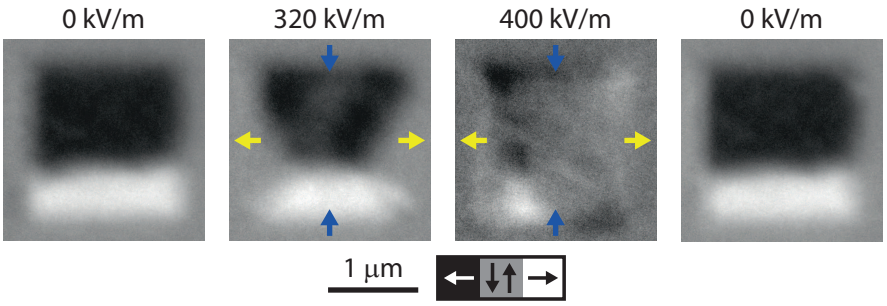

Figure 4.11: XMCD-PEEM images of 2 μm wide nanostructured Ni squares as function of the electric field applied across the piezoelectric substrate. A growth of the domains pointing along the compressive axis is observed, and a strong change in the magnetic configuration of the Ni nanostructure is observed when applying electric fields above 340 kV m^{-1} across the piezoelectric substrate. The changes are reversible, as shown in the last image, where the electric field was relaxed. The blue and yellow arrows respectively indicate the direction of the compressive and tensile axes and the grayscale bar indicates the direction of the magnetic contrast in the images. Image adapted from Ref. [90].

magnetization configuration of the nanostructured Ni ring exhibits a state not favoured by shape-anisotropy (i.e. the magnetization does not follow the curvature of the ring).

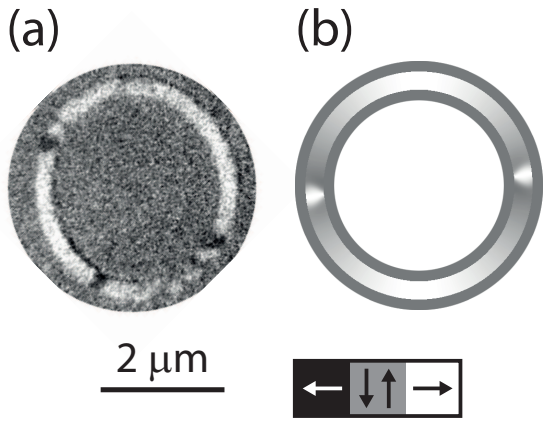

Figure 4.12: High resolution XMCD-PEEM image of a Ni ring fabricated on top of a pre-poled PMN-PT (011) substrate. (a) XMCD-PEEM image of the Ni ring; (b) Micromagnetic simulation of a Ni ring of the same geometry as (a), calculated without considering the contribution from anisotropy terms (the calculations were carried out with the parameters given in section 4.4.1). The grayscale bar indicates the direction of the magnetic contrast in the images.

The behavior of the magnetization of the nanostructured Ni rings fabricated on pre-poled PMN-PT (011) as function of the ring geometry and of the magnitude of the electric field applied across the piezoelectric substrate was also analyzed. As shown in Fig. 4.13, applying an

electric field across the piezoelectric substrate causes the nucleation of magnetic domains with their magnetization pointing in the opposite direction with respect to the original magnetic configuration of the nanostructured Ni rings (e.g. see Fig. 4.13(b)). The "reversed" magnetic domains nucleated through this effect are irreversible, i.e. once the electric field is relaxed, the original magnetic configuration of the magnetic nanostructures does not recover, as can be observed by comparing Fig. 4.13(a) with Fig. 4.13(c). The original magnetic configuration of the nanostructured Ni rings could only be recovered upon the re-application of the initialization field.

Upon the appplication of an electric field across the piezoelectric substrate, it was possible to observe, as marked in Fig. 4.13(e), that the nucleation of the "reverse" magnetic domains occurs at well-defined preferential sites, oriented at 45° with respect to the directions of the applied strain axes. As will be described in section 4.4.3, this behavior was observed only for the nanostructured Ni rings grown on pre-poled PMN-PT, and was interpreted as shear-strain effects.

The study of the response of the magnetic configuration of a set of nanostructured Ni rings fabricated on pre-poled PMN-PT as function of the electric field applied across the piezoelectric substrate was carried out. Different ring geometries were analyzed, in order to determine the influence of geometry (in particular, of the local curvature of the Ni nanostructures) on the behavior of the magnetization of the rings when a strain is applied. As the application of a strain to the nanostructured Ni rings leads, as shown in Fig. 4.13, to the nucleation of "reverse" domains, the influence of the ring geometry on these nucleation events was analyzed. The result of such analysis is presented in Table 4.1, where the number of "reverse" domains (normalized to the total number of available "nucleation sites" per ring - i.e. four sites per ring) nucleated for given ring geometries and applied electric fields is shown.

As shown in Table 4.1, the probability that a "reverse" domain will be nucleated at a given electric field is dependent on the geometry of the nanostructured ring elements. In particular, a dependency of the nucleation probability on the curvature of the nanostructured rings was observed, as rings with a larger diameter exhibit a higher probability of nucleation of a "reverse" domain (i.e. rings with a larger diameter exhibit a higher probability of nucleating an opposite domain with respect to the ring nanostructures with a smaller diameter) and, for ring nanostructures with the same diameter, narrower rings exhibit a higher probability of nucleating an opposite domain in comparison to the wider structures.

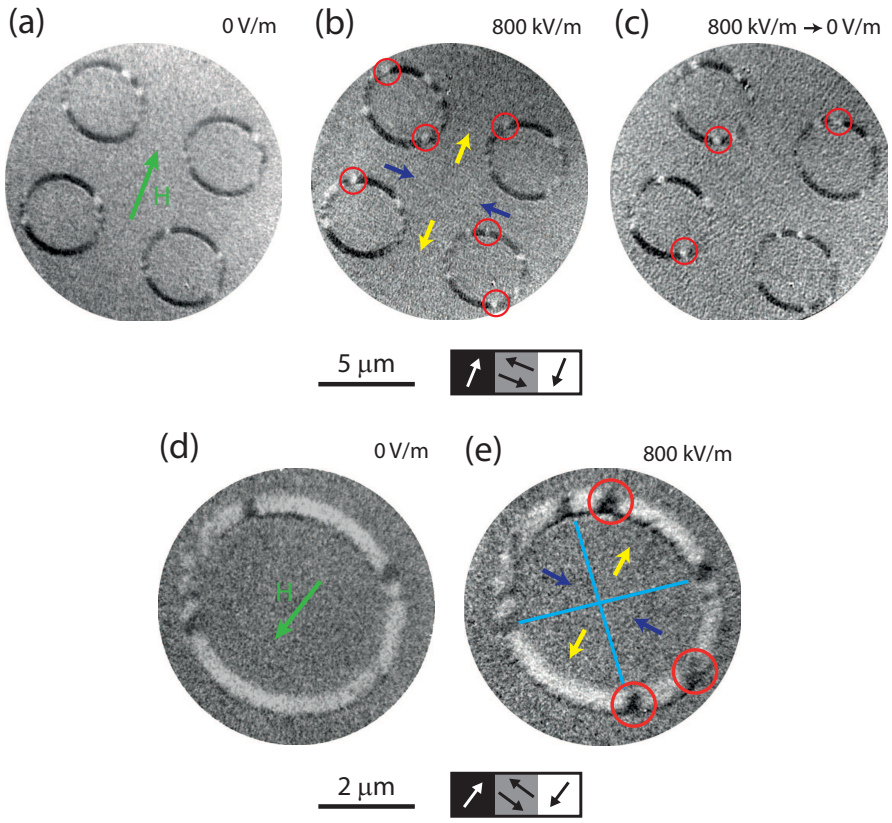

Figure 4.13: XMCD-PEEM images of nanostructured Ni rings fabricated on top of a pre-poled PMN-PT (011) substrate as function of the applied strain. (a) Ni rings (4 μm diameter, 350 nm width) after the initialization of the sample with an external magnetic field; (b) Magnetic configuration of the Ni rings during the application of an electric field of 800 kV m^{-1} across the piezoelectric substrate; (c) Magnetic configuration of the Ni rings after the relaxation of the electric field to 0 V m^{-1}; (d) Detail of a nanostructured Ni ring (4 μm diameter, 350 nm width) after the initialization of the sample with an external magnetic field; (e) Magnetic configuration of the Ni ring during the application of an electric field of 800 kV m^{-1} across the piezoelectric substrate. The green arrows denote the direction of the initialization field, the blue and yellow arrows denote the direction of the compressive and tensile axes respectively, and the red circles indicate the positions where a nucleation of domains with their magnetization pointing along the opposite direction with respect to the initialization field. The grayscale bar indicates the direction of the magnetic contrast in the images. Image adapted from Ref. [90].

4.4 Results and discussion

4.4.1 Micromagnetic simulations

As shown in section 4.3.1, the magnetic configuration of the Ni nanostructures fabricated on un-poled PMN-PT (011) substrates can be reproducibly and reversibly manipulated by the

D (μm)	W (nm)	Init	500 kV m^{-1}	800 kV m^{-1}
2	200	0.44	0.66	0.88
2	300	0.22	0.38	0.81
3	250	0.38	0.81	0.88
3	300	0.44	0.75	0.81
4	250	0.50	0.88	1.00
4	350	0.56	0.88	0.88

Table 4.1: Number of magnetic domains (normalized to the total number of "nucleation sites" per ring where these opposite domains form) with orientation opposite to the initialization field for nanostructured Ni rings fabricated on pre-poled PMN-PT (011) as function of the ring geometry (i.e. ring diameter D and ring width W) and of the applied piezoelectric strain. The determination was carried out by determining the number of opposite domains in the nucleation sites marked in Fig. 4.13(e) after the application of an electric field across the piezoelectric substrate. The ring structures were initialized by applying a magnetic field along the direction indicated in Fig. 4.13(d). In the table, a value of 1.00 indicates that a magnetic domain with opposite orientation is present in all four nucleation sites marked in Fig. 4.13(e).

application of an electric field across the piezoelectric substrate. As shown in Figs. 4.8 and 4.9, it is possible to qualitatively determine that the Ni nanostructures exhibit, as expected from the available literature on bulk and thin film Ni [11, 12, 94], a negative magnetostrictive coefficient, as the magnetic domains pointing along the compressive strain axis grow at the expense of the magnetic domains pointing along the tensile strain axis. While the qualitative observations agree with the theoretical model introduced in section 1.2.5, a quantitative analysis of the magnitude of the magneto-elastic anisotropy term still needs to be carried out, in order to verify whether the model introduced in section 1.2.5, based on a continuous thin film description, holds also for nanostructured materials. To perform this quantitative comparison between the experimental results introduced in section 4.3.1 and the theoretical model presented in section 1.2.5, micromagnetic simulations[3] (using the MicroMagnum framework [25]) of the nanostructured Ni squares under different strain conditions (see section 1.7 for more details on the micromagnetic simulations) were carried out.

For the simulation of the nanostructured Ni squares, an exchange stiffness of $A \simeq 10^{-11}$ J m^{-1} and a saturation magnetization of $M_s \simeq 2.1 \times 10^5$ A m $^{-1}$ were employed. The value of the exchange stiffness was determined by simulating a Ni nanostructure for different values of the exchange stiffness and comparing the simulations with the experimentally determined magnetic configuration of the same Ni nanostructure. The value of the saturation magneti-

[3]The micromagnetic simulations presented in this chapter were carried out by B. Krüger at the University of Mainz.

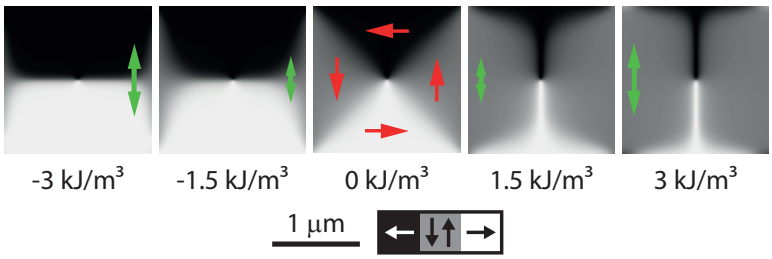

Figure 4.14: Micromagnetic simulations of 2 μm wide nanostructured Ni squares with an additional uniaxial anisotropy contribution, employed to simulate the contribution to the magnetic anisotropy arising from an applied strain. The grayscale bar indicates the direction of the magnetic contrast in the images, also indicated by the red arrows in one of the images. The green arrow indicates the direction of the uniaxial anisotropy axis used in the simulations.

zation was determined by SQUID magnetometry carried out on a continuous Ni film grown on an unpoled PMN-PT substrate. By substituting the determined values for the exchange stiffness and the saturation magnetization in Eq. (1.32), an exchange length of $l_{ex} \simeq 19$ nm was determined. The simulations were carried out with a discrete cell of 8×8 nm^2 in the xy plane and of 35 nm in the z direction, corresponding to the thickness of the Ni nanostructures (i.e. it is assumed that the magnetic configuration of the Ni nanostructures does not vary along the z direction).

The contribution of the magneto-elastic anisotropy term was included in the micromagnetic simulations by simulating the Ni nanostructures with the addition of an uniaxial anisotropy term of different magnitudes. As shown in Fig. 4.14, this additional uniaxial anisotropy term was applied along the y direction. This direction of the simulated uniaxial anisotropy axis allowed for the simulation of a compressive strain applied along the y direction. To simulate a compressive strain with its axis along the x direction, a negative value for the uniaxial anisotropy constant was employed. The simulated magnetic configurations of the Ni nanostructured squares were then compared, as will be shown in the next section, with the experimentally determined magnetization configuration of the Ni nanostructured squares.

4.4.2 Ni nanostructures fabricated on un-poled PMN-PT substrates

As shown in section 4.3.1, when nanostructured Ni squares are fabricated on an un-poled PMN-PT (011) substrate, their magnetic configuration will fall into a flux-closure state, which resembles the Landau flux-closure state.

By applying an electric field across the PMN-PT (011) substrate, thus inducing a strain to the Ni nanostructures, it is possible to give rise, as shown in Fig. 4.8, to a strain-induced uniaxial anisotropy pointing, in qualitative agreement with what is expected from the magnetostrictive properties of Ni, along the direction of the compressive strain axis. By measuring

the area of the magnetic domains pointing along or perpendicular to the compressive strain direction as shown in Fig. 4.9, it was found that the area of the aforementioned magnetic domains scales linearly with the applied electric field.

To verify whether not only a qualitative, but also a quantitative agreement between the experimental results and the theoretical model described in section 1.2.5 holds, the micromagnetic simulations with different contributions for the magneto-elastic anisotropy term were compared with the experimental results, as shown in Fig. 4.15. This comparison allows for the determination of the magnitude of the magneto-elastic anisotropy term as function of the electric field applied across the piezoelectric substrate, as shown in Fig. 4.16(a).

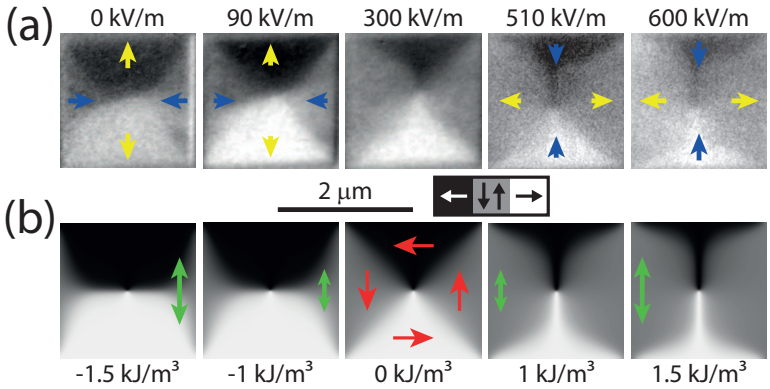

Figure 4.15: Comparison between XMCD-PEEM images and micromagnetic simulations of a 2 μm wide Ni nanostructured square as function of the applied piezoelectric strain (i.e. applied electric field across the piezoelectric substrate). (a) XMCD-PEEM images as function of the electric field applied across the piezoelectric substrate; (b) Micromagnetic simulations assuming different magnitudes of the applied uniaxial anisotropy (axis marked by the green arrows). The blue and yellow arrows indicate the direction of the compressive and tensile axes respectively, and the grayscale bar indicates the direction of the magnetic contrast, also marked by red arrows in the micromagnetic simulation images. Image adapted from Ref. [91].

As the response curve of the piezoelectric material is known (see Fig. 4.2 and [87]), it is possible to determine the magnitude of the magneto-elastic anisotropy term as function of the applied strain, as shown in Fig. 4.16(b). This curve can then be fitted with the relation for the magneto-elastic anisotropy term given in Eq. (1.21). For the fitting, a value of 220 GPa was assumed for the Young modulus of the Ni nanostructures [95], and the magnetostrictive constant λ_s of the Ni nanostructures has been employed as fitting parameter. The choice of λ_s as a fitting parameter was made based on the fact that the nanostructured Ni elements are fabricated on top of a 50 nm-thick Pt electrode, which could give rise to a different magnetic response of the nanostructured Ni if compared to the bulk case.

As shown in Fig. 4.16(b), where the result of the fit is shown by a continuous line, it is

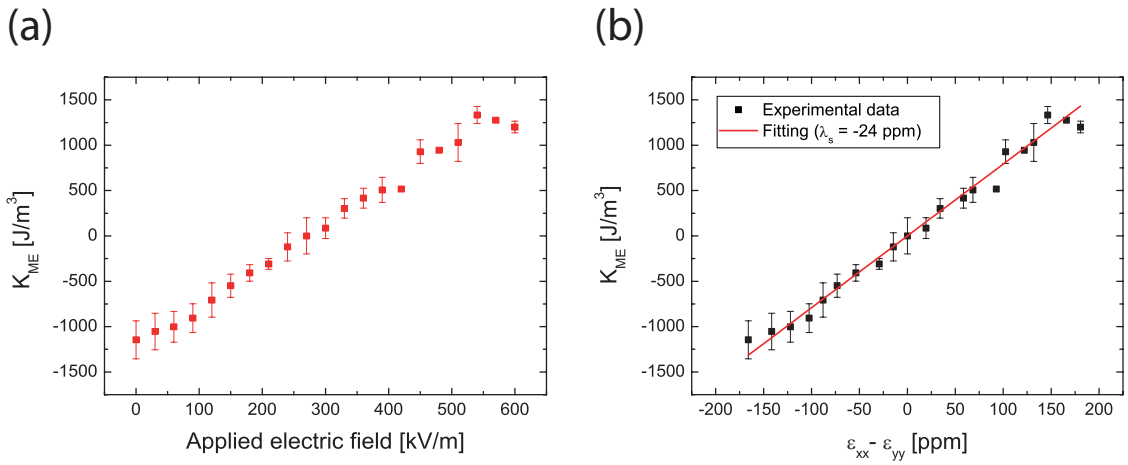

Figure 4.16: (a) Magnitude of the magneto-elastic anisotropy term induced to the Ni nanostructures as function of the electric field applied across the PMN-PT substrate; (b) Magnitude of the magneto-elastic anisotropy term as function of the in-plane strain difference $\varepsilon_{xx} - \varepsilon_{yy}$ generated by the PMN-PT substrate. The red curve indicates the values for the magneto-elastic anisotropy term calculated with Eq. (1.21). The magnitude of the uniaxial anisotropy (pointing along the y direction) was determined by comparing the experimental data with micromagnetic simulations. As further explained in the text, the "zero strain" condition has been moved to an applied field of about 270 kV m^{-1}.

possible to observe that the Ni nanostructures exhibit an "effective" magnetostrictive constant of $\lambda_s = -24 \pm 3$ ppm.

As it is possible to observe in Fig. 4.15, the 2 μm wide Ni squares exhibit a symmetric Landau magnetic flux-closure state at an applied electric field of about 270 kV m^{-1} across the piezoelectric substrate. This observation hints for the presence of an additional uniaxial anisotropy contribution at no applied strain. Different interpretations can be found for this additional anisotropy term, both of them related to the piezoelectric substrate: as the Ni nanostructures have been fabricated on top of an un-poled PMN-PT substrate, the substrate falls into a multi-domain state (i.e. multiple ferroelectric domains are present on the substrate), as shown e.g. in Ref. [41]. When the substrate is electrically poled, regions with different ferroelectric domains will give rise to regions with a different pre-strain, which can then influence the magnetization of the Ni nanostructures.

Due to a miscut of the substrates (the substrates employed for the experiments described in this chapter exhibited miscuts, measured by x-ray diffraction, in the range between 0.1° and 0.4°) giving rise to the formation of microscopic step-edges on the surface of the substrate, such additional anisotropy term can also be induced. Such additional, substrate-induced uniaxial anisotropy term was also observed for other materials, such as the Heusler alloys analyzed in

chapter 3.

Taking this additional anisotropy term into account for the analysis of the magneto-elastic anisotropy, the "zero-strain" condition was shifted to an applied electric field of about 270 kV m^{-1}.

The fitting of the experimental data (with the additional shifting of the "zero-strain" condition) allowed for the determination of an effective magnetostrictive constant for the nanostructured Ni of about -24±3 ppm. As the value of the magnetostrictive constant λ_s of bulk Ni is about -32 ppm [11,67], the value of the effective magnetostrictive constant of the Ni nanostructures determined by fitting the experimental data is only slightly smaller than the literature value for bulk Ni. This allows for the observation that the magnetostrictive properties of the nanostructured Ni do not differ significantly from what would be expected from a bulk-like description. Such a difference between the estimated magnetostrictive constant for the Ni nanostructures and the bulk Ni value can be due to a relaxation of the strain through the 50 nm thick Pt electrode between the piezoelectric substrate and the Ni nanostructures, giving rise to a lower strain applied to the nanostructures with respect to the literature values given in Ref. [87]. Another possible origin for the reduced value of the magnetostrictive constant could be due to the deposition of the Ni, which gives rise to polycrystalline films, where strain-relaxation at the grain boundaries might affect the magnetostrictive properties of the material.

It is also possible to notice that, as shown in Fig. 4.9, for larger electric fields applied across the piezoelectric substrate, corresponding to an increased value for $|\varepsilon_{xx} - \varepsilon_{yy}|$, the magnitude of the area of the magnetic domains pointing along the compressive axis starts to exhibit a saturating behavior. This saturating behavior, due to the contribution of shape-anisotropy, was confirmed by micromagnetic simulations carried out at higher simulated strains, not achievable experimentally due to cracking of the substrate that occurs at applied electric fields above about 600 kV m^{-1} [91].

As introduced at the beginning of this chapter, the combination of a piezoelectric and a magnetostrictive material can be employed to fabricate an artificial multiferroic system that exhibits, as a whole, a magneto-electric coupling. If the piezoelectric response of the substrate is taken into consideration, it is possible to determine the magnitude of the response of the magnetization due to the application of an electric field. This describes the strength of the magneto-electric coupling, defined as *magneto-elastic coupling coefficient*: $\alpha = \mu_0 \frac{\Delta M}{\Delta E}$ [96], where ΔM is the change in the magnetization of the material that occurs due to a change ΔE in the electric field applied to the material. If, similarly to what is reported in Ref. [97], ΔM is described as $\Delta M = M_s \Delta A$, being ΔA the variation of the area (normalized to the total area) where the magnetization is pointing along the compressive strain direction, it is possible to estimate a magneto-electric coupling coefficient of $\alpha \simeq 3 \times 10^{-7}$ s m^{-1}, comparable to

what was observed for other magneto-electric multiferroic systems [98, 99].

4.4.3 Results on the pre-poled PMN-PT substrates

In contrast to the experimental observations carried out on Ni nanostructures fabricated on un-poled PMN-PT (011) substrates, if the Ni nanostructures are fabricated on pre-poled PMN-PT substrates, their magnetic configuration exhibits a strong contribution arising from an uniaxial anisotropy term, as shown in Fig. 4.10, stronger than the one observed for the Ni nanostructures fabricated on un-poled PMN-PT substrates [90].

As already mentioned, for these samples, the Ni was deposited on top of a PMN-PT substrate that had been electrically poled prior to the deposition. PMN-PT is, however, a relaxor ferroelectric crystal [88], thus meaning that the piezoelectric strain generated after the poling will relax, in time, back to its "un-poled" configuration. The relaxation of the strain after the deposition deforms the Ni film, giving rise to the generation of an uniaxial anisotropy contribution due to the magneto-elastic coupling.

When, as shown in Fig. 4.11, an electric field is applied across the pre-poled substrate, a reduction of this uniaxial anisotropy term will be observed (compare Fig. 4.11(a) with Fig. 4.11(b)), in agreement to what has been observed also for the Ni nanostructures fabricated on un-poled PMN-PT substrates. However, in contrast to what has been observed on un-poled PMN-PT substrates, when an electric field higher than about 340 kV m^{-1} is applied across the piezoelectric substrate, strong (and sudden) changes of the magnetic configuration of the nanostructured Ni squares will be observed, as shown in Fig. 4.11(c). When an electric field higher than about 340 kV m^{-1} is applied, the magnetic configuration of the nanostructured Ni squares will exhibit magnetic domains pointing along the perpendicular direction with respect to the direction of the uniaxial anisotropy axis at no applied strain. These experimental observations were interpreted considering the fact that, at an applied electric field of about 340 kV m^{-1}, the strain condition at which the deposition of the Ni film occurred is recovered, thus giving rise to a magnetic configuration where the dominant contribution to the magnetic free energy is given by shape anisotropy. For higher fields, in agreement with what has been observed for the Ni nanostructures fabricated on un-poled PMN-PT substrates, the magneto-elastic anisotropy term favors the direction perpendicular to the one favored at no applied strain. The physical reason behind the sudden change of the magnetic configuration is however not yet clear, and further analyses of this "transition" will be required.

Also in agreement with the observed behavior for the Ni nanostructures fabricated on un-poled PMN-PT (011) substrates, the magnetic configuration of the nanostructured Ni squares was reversible with respect to the applied electric field, i.e. the original state could be recovered by relaxing the electric field applied across the piezoelectric substrate, as shown in Fig. 4.11(d).

As shown in Figs. 4.12 and 4.13, the magnetic configuration of nanostructured Ni rings fabricated on pre-poled PMN-PT substrates exhibits a different behavior with respect to what was observed for the nanostructured Ni squares, also as function of the applied electric field.

As it is possible to observe in Fig. 4.12(a), at no applied strain the Ni nanostructured elements exhibit a magnetic configuration strongly dominated by the contribution of an uniaxial anisotropy term (in contrast to the expected state, shown in Fig. 4.12(b)). When an electric field is applied across the piezoelectric substrate, as shown in Fig. 4.13, a nucleation of "reverse" domains is observed (i.e. of magnetic domains pointing along a direction opposite to the configuration they exhibited upon initialization). The nucleation of these magnetic domains occurred preferentially at sites oriented at 45° with respect to the direction of the applied compressive and tensile strain axes, as depicted in Fig. 4.13(e).

After systematically analyzing the switching behavior of the nanostructured Ni rings fabricated on pre-poled PMN-PT, it was possible to observe that the geometry of the Ni rings, in particular their local curvature, influences the probability of nucleating a reverse magnetic domain upon the application of an electric field across the piezoelectric substrate. It was observed, as shown in Table 4.1, that the narrower rings with a larger diameter exhibit a higher probability of nucleating an opposite magnetic domain (if compared with the wider, smaller diameter rings). Thus, a higher probability of nucleating an opposite magnetic domain was observed for the nanostructured rings exhibiting a lower local curvature (i.e. large diameter rings). The observed behavior was interpreted by considering the contribution of shape anisotropy, which is favoring domain wall motion for rings with a smaller curvature (i.e. with a larger diameter) [90].

The nucleation of these reverse magnetic domains is irreversible, as shown in Fig. 4.13: the relaxation of the applied electric field did not allow for the recovery of the original magnetic configuration. The original magnetic configuration could only be recovered upon the reapplication of the initialization field. Thus, a bi-stable magnetic state, accessible by the application of a piezoelectric strain, was observed for these nanostructured Ni rings.

4.5 Conclusions and summary

Different paths can be undertaken to achieve a current-less control of the magnetic configuration of a material, as shown in Fig. 4.1. In this chapter, the fabrication and characterization of a magneto-electric artificial multiferroic system was described. In particular, the artificial multiferroic system here analyzed is composed of the combination of a piezoelectric material and of a magnetostrictive material, thus allowing for a (indirect) control of the magnetic configuration of the magnetostrictive material by applying an electric field across the piezoelectric material.

Magnetostrictive Ni nanostructures of different geometries were fabricated by lithographical patterning onto piezoelectric PMN-PT (011) substrates, as described in further detail in section 4.2. By employing (011)-cut PMN-PT substrates, it was possible to generate an in-plane, volume-conserving, strain onto the Ni nanostructured elements. This in-plane strain was generated by the application of an electric field in the out-of-plane direction of the PMN-PT crystal, giving rise to the piezoelectric response curves shown in Fig. 4.2. By observing the piezoelectric response curves of the PMN-PT (011), it is possible to note that, once the PMN-PT crystal has been poled in one direction, the piezoelectric response of this material is linear with the applied electric field, thus providing good experimental conditions for investigating of the magneto-elastic anisotropy model introduced above. The Ni nanostructures were fabricated onto both un-poled and pre-poled piezoelectric substrates, which led, as shown in sections 4.4.2 and 4.4.3, to a different response of the magnetic configuration of the Ni with respect to the applied electric field. The magnetic configuration of the Ni nanostructures was analyzed by high-resolution XMCD-PEEM imaging, employing the experimental configuration shown in Fig. 4.5, which allowed for the imaging of the magnetic configuration of the Ni nanostructures both with and without an electric field applied across the PMN-PT substrate.

As shown in section 4.3.1 and discussed in section 4.4.2, when the Ni nanostructures are fabricated onto un-poled PMN-PT (011) substrates, the application of an electric field across the PMN-PT substrate leads to the generation of a uniaxial anisotropy (as shown e.g. in Fig. 4.8). This magneto-elastic anisotropy term exhibits, as shown in Fig. 4.8, an easy axis parallel to the direction of the applied compressive strain, in qualitative agreement with what is expected from Ni (i.e. a material with a negative magnetostrictive constant) [12]. This agreement was also confirmed quantitatively by comparing the experimentally-determined magnetic configuration of the Ni nanostructures with micromagnetic simulations, as shown in sections 4.4.1 and 4.4.2. This comparison, carried out as function of the magnitude of the strain applied to the magnetostrictive nanostructures, allowed for the conclusion that the experimentally observed magneto-elastic anisotropy contribution is well described by the model presented in section 1.2.5. Moreover, as shown in Fig. 4.16, it is possible to observe that, according to the theoretical model presented in section 1.2.5, the Ni nanostructures fabricated on un-poled PMN-PT exhibit an "effective" magnetostrictive constant of $\lambda_s = -24 \pm 3$ ppm, close to the value for bulk Ni (i.e. $\lambda_{s,\mathrm{bulk}} \simeq -32$ ppm [11, 94]). This observation allows for the conclusion that the strain generated by the piezoelectric substrate is fully transferred to the Ni nanostructures, and that shear-strain effects and strain relaxation effects at the edges of the Ni nanostructures do not appear to influence the response of the Ni nanostructures to an applied strain, confirming the validity of the model introduced in section 1.2.5 also for the description of nanostructured Ni elements.

As shown in section 4.3.2 and discussed in section 4.4.2, if Ni nanostructured elements

are fabricated onto pre-poled PMN-PT (011) substrates, the response of their magnetic configuration to an electric field applied across the PMN-PT substrate is substantially different compared to un-poled PMN-PT substrates. As shown in Fig. 4.10, the magnetic configuration of the Ni nanostructures fabricated on pre-poled PMN-PT (011) substrates exhibits at no applied piezoelectric strain a magnetic configuration dominated by an uniaxial anisotropy term with a significantly lower magnitude if the Ni nanostructures are fabricated on un-poled PMN-PT, as shown in Fig. 4.10. The response of the magnetic configuration of the Ni nanostructures upon the application of a piezoelectric strain is also dominated by this additional anisotropy term, as shown in Figs. 4.11 and 4.13. Considering that PMN-PT is a relaxor ferroelectric [88], it is possible to give an interpretation to the strong uniaxial anisotropy term observed for the Ni nanostructures fabricated on pre-poled PMN-PT substrates: this material, after it is poled, relaxes in time back to its original configuration. This means that, if the Ni nanostructures are fabricated on top of a pre-poled PMN-PT substrate, the relaxation of the substrate in time will lead to the application of a strain to the Ni nanostructures, giving rise to a magneto-elastic anisotropy contribution. It was nonetheless possible to observe that, for some geometries of the Ni nanostructures, this additional anisotropy term gives rise, as shown in Fig. 4.13, to the presence of a bi-stable magnetic state in the nanostructures at no applied strain, which is of interest for memory applications.

In conclusion, it was possible to observe that, by combining a piezoelectric material with a magnetostrictive material, it is possible to achieve a current-less control of the magnetization, where the application of an electric field leads to the generation of an uniaxial magnetic anisotropy term, which can be described with a simple model, where the uniaxial anisotropy is directly proportional to the electric field applied across the piezoelectric substrate (provided a linear dependence of the applied strain with respect to the voltage applied across the piezoelectric substrate).

The results on the behavior of the magnetic configuration for Ni nanostructures fabricated on pre-poled PMN-PT (011) substrates have been published in the journal *SPIN* [90], and the results on the control of the magnetic configuration for the nanostructures fabricated on un-poled PMN-PT (011) substrates have been published in the journal *Physical Review Applied* [91].

Chapter 5

Current-induced domain wall hopping in $La_{0.7}Sr_{0.3}MnO_3$ nanostructured elements

The *spin-transfer-torque* effect is a promising alternative approach for the manipulation of the magnetization in a magnetic material exhibiting both no mechanically-moving parts and a good scalability. This effect relies on the torque imprinted by a spin-polarized current on the local magnetization of a magnetic material (which, as described in further detail in section 1.6, can be described by an additional term to the LLG equation), which can be employed to physically displace magnetic domains [21] and to switch the magnetization [100]. Since its first discovery [20], a series of different possible devices based on the spin-transfer torque effect has been proposed [21, 101, 102]. However, there still are some applicability issues, such as the requirement of high current densities, in $3d$ ferromagnetic materials, to manipulate the magnetic configuration through the spin-transfer-torque effect, thus prompting a search for different materials where lower current densities allow for the manipulation of the magnetic configuration through the spin-transfer torque effect.

In this chapter, the response of the magnetic configuration of nanostructured elements fabricated out of the ferromagnetic oxide $La_{0.7}Sr_{0.3}MnO_3$ (LSMO) will be presented. The chapter is organized as follows: first, the motivations behind the choice of LSMO as a material for spin-torque applications will be given. Then, the fabrication process of the LSMO nanostructured elements will be described, followed by the presentation and discussion of the experimental results obtained by low-temperature transport measurements and by room-temperature x-ray magnetic microscopy.

5.1 Current-induced domain wall motion

As described in detail in section 1.6, the flow of a current in a magnetic material is affected by and can affect its magnetic configuration. The latter effect, known as spin torque effect, can be employed to influence the magnetic configuration of a material with the injection of spin-polarized currents.

As shown in Eq. (1.30), both the adiabatic and non-adiabatic spin-torque terms are proportional to $\mathbf{u}$, which, as shown in (1.31), is proportional to the ratio between the spin polarization P and the saturation magnetization M_s of the magnetic material. Thus, if the magnetic material exhibits a high spin polarization and a low saturation magnetization, the flow of spin-polarized electrons in the material will give rise to a higher variation of the local magnetization (i.e. a high *spin-transfer-torque efficiency* is expected for these materials).

From the definition of $\mathbf{u}$ given in (1.31), it is also possible to observe that both the adiabatic and non-adiabatic spin-torque contributions are proportional to the magnitude of the current density j. This implies that a higher current density will give rise to a larger spin-transfer-torque effect, and that a system based on this effect to manipulate the magnetic configuration of a material will not encounter the scalability issues of the Oersted-field approach (as the spin-torque effect is governed by the magnitude of the applied current density, and not of the applied current).

Spin-transfer-torque effects have been, in the last years, extensively studied in $3d$-based ferromagnetic materials [21]. In particular, the displacement of magnetic domain walls with spin-polarized currents (current-induced domain wall motion) has been extensively analyzed on these materials (see e.g. Refs. [21, 103, 104]). However, $3d$-based ferromagnetic materials exhibit, due to their high saturation magnetization and relatively low spin polarization, a relatively low spin-transfer-torque efficiency. This has thus prompted research on materials for spin-torque applications exhibiting a combination of high spin-polarization and low saturation magnetization.

Ferromagnetic oxides such as Fe_3O_4 and CrO_2 have thus been of interest for spin-transfer-torque applications [105, 106], thanks to the high spin-transfer-torque efficiency promised by the combination of high spin polarization and relatively low saturation magnetization offered by these materials. However, as pointed out in Refs. [105,106], the sole promise of a high spin-transfer-torque efficiency is not enough to guarantee the applicability of these materials for current-induced domain wall motion applications: also the possibility to reliably control the spin structure of the magnetic domain walls to be displaced by the spin-polarized currents is of critical importance for current-induced domain wall motion applications. Thus, a material exhibiting a low magneto-crystalline anisotropy (beyond the high spin polarization and low saturation magnetization) has to be sought, in order to achieve a good control of the spin structure of the magnetic domain walls.

LSMO is a ferromagnetic oxide material that, thanks to its high spin polarization (this material is fully spin-polarized) [107] and relatively low saturation magnetization at room temperature [108], is, like Fe_3O_4 and CrO_2, of interest for spin-torque applications. As confirmed by magnetometry [108] and x-ray microscopy experiments [28,109], the magnetic configuration of LSMO can be reliably controlled by shape anisotropy, thanks to the lower magneto-crystalline anisotropy and electrical resistivity of LSMO if compared to other oxide ferromagnets such as Fe_3O_4 and CrO_2. These reasons prompted the studies presented in this chapter, where the response of the magnetic domain walls in nanostructured LSMO elements to the application of spin-polarized currents will be analyzed.

5.2 Fabrication of nanostructured $La_{0.7}Sr_{0.3}MnO_3$ elements

The experiments described in this chapter were carried out on nanostructured elements fabricated out of 30 nm-thick LSMO films heteroepitaxially grown on $SrTiO_3$ (STO) (001) substrates. The LSMO films were grown by pulsed laser deposition and metalorganic aerosol deposition[1]. Due to an excessive charging of the insulating STO substrates upon XMCD-PEEM imaging, the LSMO films employed for the XMCD-PEEM imaging experiments described in section 5.4 were grown on semiconducting 0.01 wt.% Nb-doped STO (001) substrates. For these films, to avoid the shunting of the LMSO nanostructures through the Nb:STO substrate, an additional 45 nm-thick layer of insulating STO was homoepitaxially deposited on the Nb:STO substrate prior to the deposition of the LSMO thin films [111].

To study the manipulation of magnetic domain walls in LSMO induced by the application of a current, nanostructured LSMO elements were fabricated by a multi-step lithographical processing. The LSMO thin films were structured with a half-ring geometry (with a diameter of 10 μm and ring widths between 500 nm and 2 μm), as can be observed in the scanning electron micrograph shown in Fig. 5.1. By choosing a half-ring geometry, it was possible to nucleate magnetic domain walls at the center of the half-ring with the application of a magnetic field along the axis perpendicular to the half-ring structure (marked by the green arrow in Fig. 5.1).

The fabrication of the nanostructured LSMO half-rings was carried out with a multi-step lithographical processing: first, the as-deposited continuous LSMO thin films were coated with a negative tone resist (NLof 2070, MicroChem GmbH), exposed by electron-beam lithography, and subsequently developed, leaving the areas where the LSMO half-rings were fabricated protected by the exposed resist. The LSMO half-rings structures that were employed for the magneto-transport measurements described in section 5.3 were fabricated by Ar^+ ion milling,

[1]The pulsed laser deposition and metalorganic aerosol deposition of the LSMO thin films were respectively carried out by collaborating groups at the CRNS of Caen [28] and at the University of Göttingen [110].

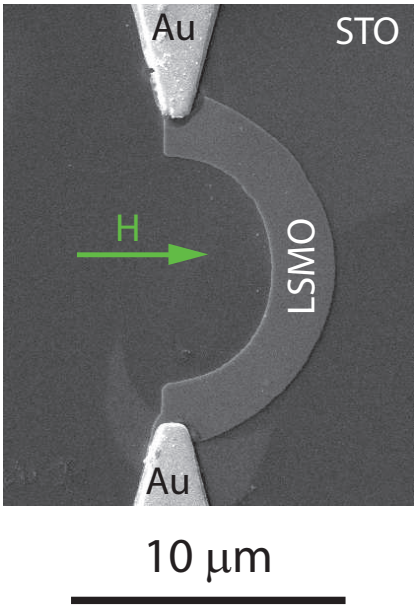

Figure 5.1: Scanning electron micrograph of a 2 μm wide LSMO half-ring nanostructure, showing also the Au electrodes employed to contact the nanostructure. The green arrows indicates the direction of the magnetic field applied to initialize the magnetic configuration of the half-ring elements.

as described in further detail in Ref. [112]. Instead, the LSMO half-ring structures that were employed for the XMCD-PEEM imaging experiments described in section 5.4 were fabricated by wet chemical etching, due to the presence of the 45 nm-thick insulating STO layer, whose integrity had to be preserved to avoid a shunting of the LSMO nanostructures through the semiconducting Nb:STO substrate. The etching of the unprotected LSMO areas was carried out with a solution of 0.25 % H_2O_2 and 0.25 % H_2SO_4 solved in deionized water. The etching process relies, in this case, on the reduction of the insoluble Mn(IV) oxide in the LSMO to the soluble Mn(II) oxide, according to the following chemical reaction:

$$MnO_2 + H_2O_2 + 2H_3O^+ \rightarrow Mn^{2+} + 4H_2O + O_2.$$

The unprotected LSMO was etched away after about 30 s of immersion in the etching solution (followed by an immediate rinsing in deionized water), indicating an etching rate of about 1 nm s^{-1}. Different etching solutions, all relying on the reduction of the Mn(IV) oxide to Mn(II) oxide [113], were tested. However, the best conditions for the chemical etching of the LSMO were found with the H_2O_2 and H_2SO_4 solution above mentioned. In all cases, the etching solutions were found to not attack the insulating STO layer between the LSMO film and the Nb:STO substrate (i.e. etching rates less than 1 nm min^{-1} were observed), thus guaranteeing the integrity of the STO insulating layer.

The LSMO half-ring structures were then contacted with 100 nm-thick Au electrodes fabricated by electron-beam lithography[2] followed by a lift-off step, employing a positive tone resist (PMMA and its co-polymer MMA, MicroChem GmbH).

5.3 Current-assisted depinning of domain walls in LSMO half-ring nanostructures

The movement of a magnetic domain wall in a magnetic nanostructure can be detected by magneto-transport measurements, where the resistance across the nanostructured element is measured. The magneto-resistance measurement technique has been employed to analyze the response of magnetic domain walls in LSMO half-ring structures upon the injection of current pulses across the nanostructured elements[3].

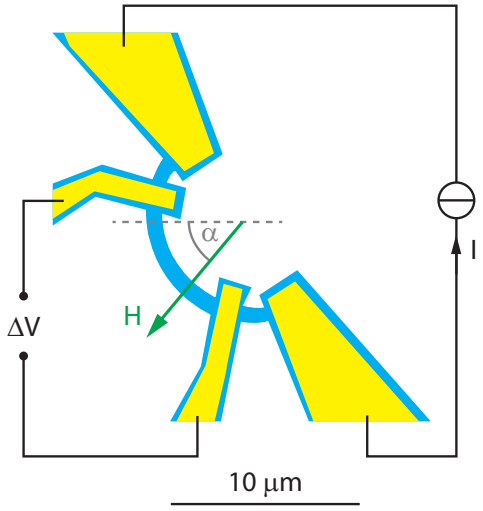

Figure 5.2: Sketch of the measurement system for the depinning measurements. The LSMO half-ring structure (depicted in cyan) was contacted with four Au electrodes (depicted in yellow). The top and bottom electrodes were employed for the injection of the current pulses and for the injection of the probing current for the magneto-resistance measurements, while the central contacts were employed to probe the voltage across the center of the half-ring structure for the magneto-resistance measurements. The angle convention for the applied external magnetic field is also defined in the picture (angle defined as α).

The LSMO half-rings were structured as schematically shown in Fig. 5.2 (i.e. with four electrical contacts, allowing for the possibility to carry out four-point resistance measurements). The magnetic configuration of the LSMO half-ring structures was initialized by the

[2]The exposure by electron-beam lithography were carried out at the Paul Scherrer Institut by F. Büttner.

[3]These measurements were carried out in cooperation with M. Foerster employing a Helium cryostat, where the nanostructured LSMO samples were inserted in a Helium bath, at a temperature of 4.2 K.

application of a magnetic field of 300 mT along the direction perpendicular to the axis of the half-ring element, as marked by the green arrow in Fig. 5.1. The successful nucleation of a magnetic domain wall at the center of the half-ring nanostructure was verified by measuring the resistance across the half-ring nanostructure as function of the direction of the initialization field (the angle convention employed for the initialization field is schematically shown in Fig. 5.2). As shown in Fig. 5.3, where the resistance across the LSMO half-ring element after the application of a 300 mT magnetic field along different angular directions is illustrated (all the resistive measurements were carried out at no applied fields), a distinct change of the resistance measured across the LSMO half-ring element is detected when the direction of the initialization field points to the area within the probing electrodes (see Fig. 5.2), thus demonstrating the successful nucleation of a (head-to-head) magnetic domain wall by the initialization field.

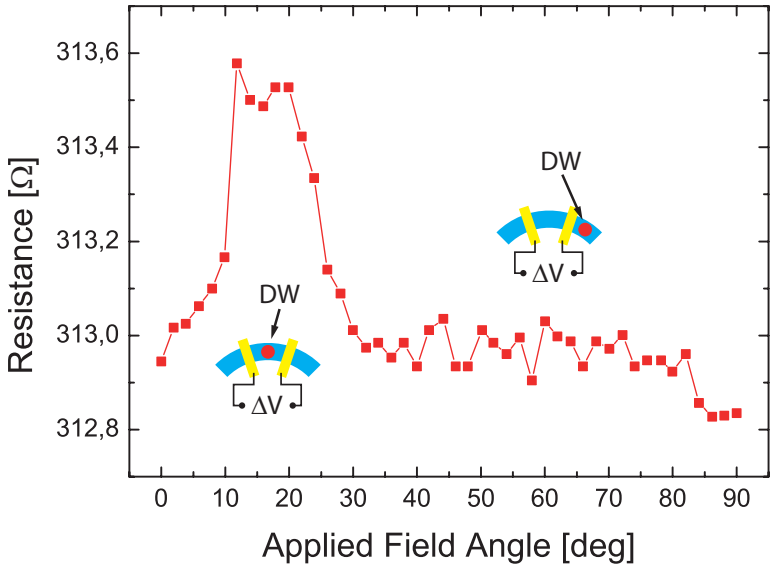

Figure 5.3: Resistance across a nanostructured LSMO half-ring as function of the direction of the applied initialization field (magnitude of 300 mT). It is possible to observe that, when a domain wall (DW) is nucleated between the four-point contacts, an increase of the resistance across the half-ring structure is observed. The two sketches of the half-ring structure depict the position of the domain wall with respect to the probing electrodes for the "high" and "low" resistance states. Image adapted from Ref. [112].

After the magnetic initialization of the LSMO nanostructures, the spin-transfer-torque assisted depinning of the nucleated magnetic domain walls was analyzed. Current pulses with a temporal width of 10 μs and current densities up to 4×10^{10} A m^{-2} were injected (in 3-pulse bursts) across the LSMO half-ring structures. While injecting the current pulses, a constant magnetic field of different magnitudes was applied along the half-ring structure. The

magnitude of the magnetic field required to depin the magnetic domain wall from the center of the half-ring structure was then determined as function of the current density of the injected current pulses.

The depinning of the magnetic domain wall from the center of the LSMO half-ring structure can be detected by monitoring the resistance across the LSMO half-ring structures after the injection of the current pulses (the resistive measurements were carried out, also in this case, at no externally-applied magnetic fields). As shown in Fig. 5.4, the depinning of the domain wall from the center of the half-ring structure gives rise to a clear reduction of the resistance across the LSMO half-rings, thus allowing for a clear determination of the depinning field.

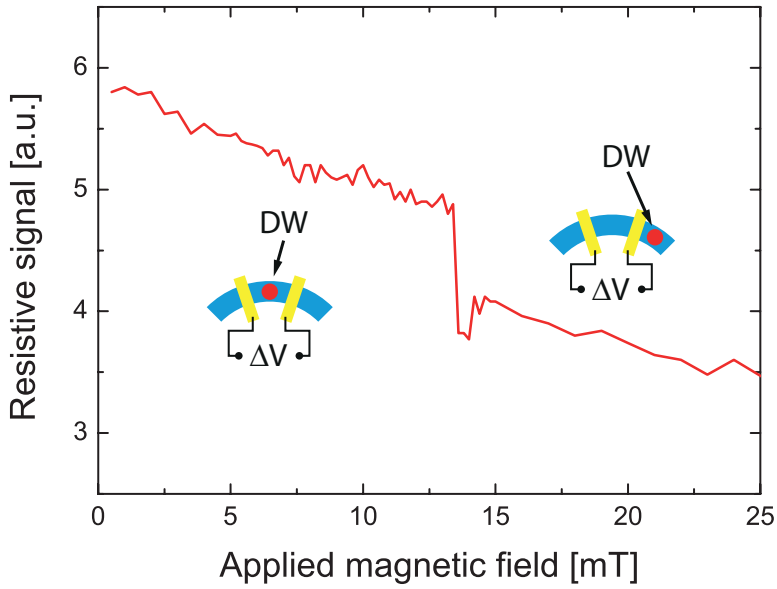

Figure 5.4: Example of a measurement of the depinning field in an LSMO half-ring nanostructure. It is possible to observe, at an applied magnetic field of about 13.5 mT, a sharp reduction in the resistance measured across the LSMO half-ring nanostructure, which is indicating a depinning of the magnetic domain wall. Image adapted from Ref. [112].

The depinning field as function of the current density of the injected pulses was determined, and it is shown, for an LSMO half-ring structure of 2 μm diameter, in Fig. 5.5. As can be observed in Fig. 5.5, the injection of current pulses across the LSMO half-ring structure causes a reduction of the depinning field, if compared with the pure-field depinning case, thus confirming a spin-torque contribution to the domain wall motion. As will be further explained in section 5.5, the depinning measurements described in this section allowed for the calculation of the spin-transfer-torque efficiency for this material, which is, at low temperatures, almost an order of magnitude higher than the spin-transfer-torque efficiency of $3d$ ferromagnetic materials such as Py [112, 114].

As shown in Fig. 5.5, the injection of pulses with a current density $j \leq 8{\times}10^9$ A m^{-2} leads

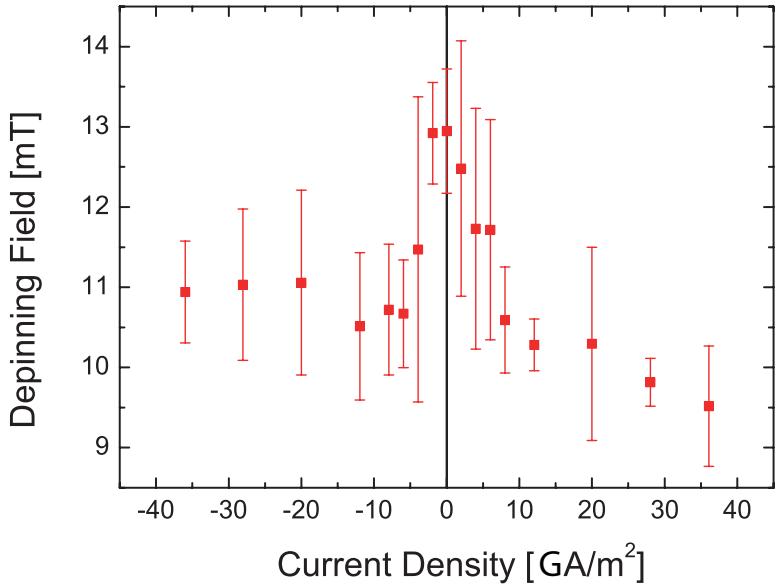

Figure 5.5: Depinning field as function of the current density of the pulses injected across an LSMO half-ring structure. It is possible to observe, for positive values of the current density (i.e. for pulses where the electron flow is anti-parallel to the applied magnetic field), a stronger reduction of the depinning field with respect to the case where the electrons flow along the applied magnetic field direction is observed. Image adapted from Ref. [112].

to a reduction of the depinning field for both polarities of the injected pulses (i.e. for both signs of the current density). As will be further discussed in section 5.5, this effect cannot, due to its symmetric behavior with respect to the sign of the current density, be linked with a contribution of spin-transfer-torque effects, but can rather be interpreted as a Joule-heating induced effect. The injection of current pulses with a current density $j \geq 8 \times 10^9$ A m^{-2} leads, instead, to an asymmetric behavior of the depinning field with respect to the sign of the current density, an effect which can be referred to the contribution of spin-transfer-torque effects.

The injection of current pulses with current densities higher than 2×10^{10} A m^{-2} across the half-ring structures caused, in some events, a sharp change of the resistance measured across the LSMO half-ring elements, not corresponding to the changes expected from a depinning of the magnetic domain wall. Both higher and lower resistance values with respect to the initialized state were measured, hinting that random changes in the magnetization occurred upon the injection of the current pulses across the half-ring structures. The original value of the resistance across the LSMO half-rings could, however, be recovered upon the re-application of the initialization field. The possibility to recover the original value of the resistance across the LSMO half-ring structures by re-applying the initialization field reveals that the changes in the resistance upon the injection of the current pulses are due to the changes in the magnetic con-

figuration of the LSMO, thus excluding other possible origins, such as for instance irreversible damage to the half-ring structure induced by electro-migration effects. The events that caused these sharp changes in the resistance measured across the LSMO half-ring structures were not considered for the calculation of the error bars shown in Fig. 5.5.

The interpretation of the results described in this section will be given, along with the interpretation of the results from the XMCD-PEEM imaging experiments, in section 5.5.

5.4 XMCD-PEEM imaging of LSMO nanostructures under application of a current

Another experimental method that can be employed for the detection of the displacement of a magnetic domain wall is XMCD-PEEM imaging, where the magnetic configuration of the nanostructured ferromagnetic elements can be fully resolved. In this section, the results of high resolution XMCD-PEEM imaging of the LSMO nanostructures fabricated on Nb:STO (001) substrates will be presented. The XMCD-PEEM imaging[4] of the nanostructured LSMO half-rings was carried out by tuning the circularly-polarized x-rays to an energy of 642 eV, corresponding to the L_3 absorption edge of Mn. As can be observed in Fig. 5.6(a), this leads to a strong XMCD contrast in the images.

The magnetic configuration of the LSMO half-ring structures was initialized to contain a magnetic domain wall at the center of the half-ring structure by the application of a magnetic field of about 50 mT along the direction perpendicular to the half-ring, as indicated by the green arrow in Fig. 5.1. The magnetic field was generated with an *in-situ* electromagnet, integrated on the PEEM sample holder [115].

Current pulses with a length of 1 ms and current densities up to 2×10^{11} A m^{-2} were injected in 3-pulse bursts across the LSMO half-ring structures, and the magnetic configuration of the LSMO half-ring elements was imaged prior and after the injection of the current pulses. To carry out the injection of the current pulses, a custom-built PEEM setup [115], similar in concept to the setup described in section 2.2.5, was employed.

The changes in the magnetic configuration of the nanostructured LSMO half-ring elements upon the injection of the current pulses were determined by calculating the differences between the XMCD-PEEM images prior and after the injection of the current pulses. As shown in Fig. 5.7, the calculation of the difference images was carried out by subtracting the XMCD-PEEM image acquired prior to the injection of the current pulses from the image acquired after the injection. The calculation of the difference images allows for a simpler determination of the

[4]These measurements were performed at room temperature at the SIM (X11MA) beamline at the Swiss Light Source [65, 66], and at the UE49-PGMa beamline at the synchrotron radiation facility (BESSY) of the Helmholtz Zentrum Berlin [93].

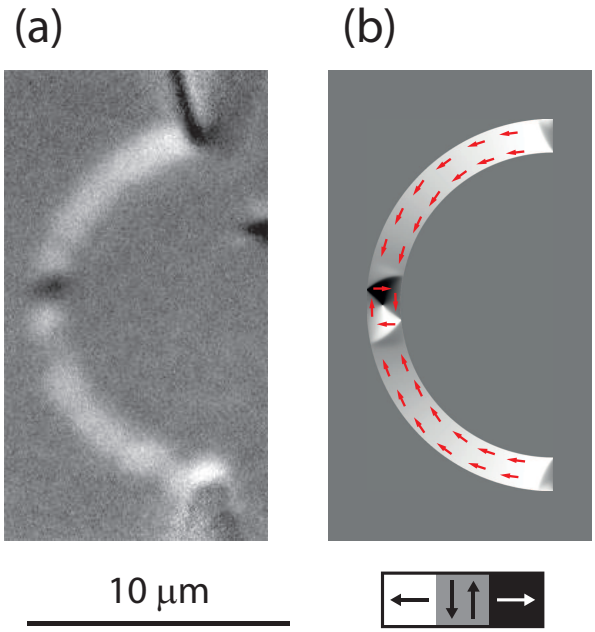

Figure 5.6: (a) XMCD-PEEM of a 1 μm wide LSMO half-ring structure, exhibiting a vortex domain wall at the center of the half-ring structure; (b) Micromagnetic simulation of a 1 μm wide LSMO half-ring structure with the parameters given in section 5.5, showing good agreement with the experimental image. The grayscale bar indicates the direction of the magnetic contrast in the images, and the red arrows indicate the direction of the magnetization in (b). Image adapted from Ref. [111].

changes in the magnetic configuration induced by the injection of a current pulse, but requires the registration of all the acquired images prior to the calculation. The registration of the single XMCD-PEEM images before the calculation of the difference images was carried out with the procedure described in section 2.2.4.

The response of the magnetic configuration of the nanostructured LSMO half-ring elements upon the injection of current pulses with different current densities across the LSMO half-ring structure was then systematically investigated by XMCD-PEEM imaging. In Fig. 5.8, an example of a series of difference images, calculated from the images acquired during a series of injections of current pulses with a density of 1.2×10^{11} A m^{-2} across a 2 μm wide LSMO half-ring structure, is shown. As can be observed in Fig. 5.8, the injection of the current pulses across the LSMO half-ring does not lead to a clear displacement of the domain wall in the nanostructure. Instead, a hopping of the domain wall between different pinning sites was observed. This current-induced hopping of the domain wall was also superimposed with nucleation and annihilation events, where magnetic domains (and domain walls) were nucleated and annihilated by the injection of the current pulses.

The angular position of the magnetic domain wall in the LSMO half-ring nanostructures

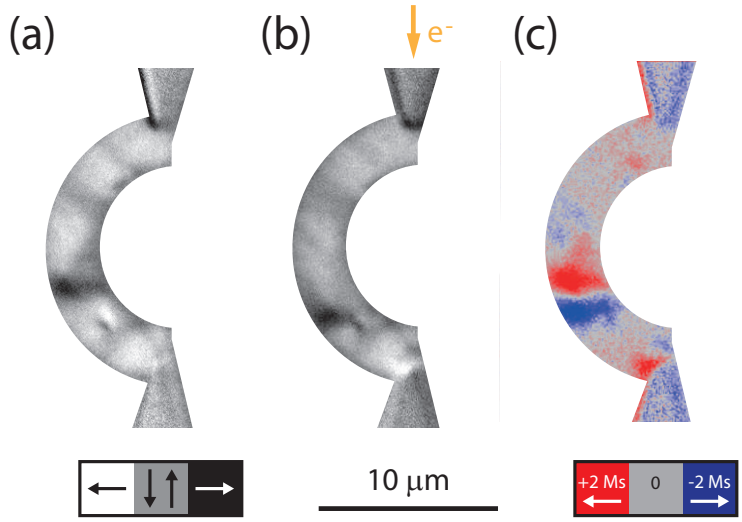

Figure 5.7: Example illustrating the calculation of an XMCD difference image. (a) XMCD-PEEM image of an LSMO half-ring structure; (b) XMCD-PEEM image of the half-ring structure shown in (a) after the injection of current pulses of 1×10^{11} A m^{-2} of current density; (c) Difference image calculated by substracting (a) from (b), allowing for a clear identification of the displacement of the magnetic domain wall after the injection of the current pulse. The orange arrow in (b) indicates the direction of the injected electrons. The grayscale bar indicates the direction of the magnetic contrast in (a) and (b), while the red/blue bar illustrates the interpretation of the color code in (c). Image adapted from Ref. [111].

was then determined from the analysis of the XMCD-PEEM images after each of the injection events, an example of which is shown in Fig. 5.9. As shown in Fig. 5.9, depicting the position of the magnetic domain wall in a 2 μm wide LSMO half-ring nanostructure, the injection of current pulses with a current density of 4×10^{10} A m^{-2}, leading to a detectable current-induced domain wall motion at lower temperatures as shown in section 5.3 and in Ref. [112], leads, in this case, to a displacement of the magnetic domain wall dominated by thermally activated hopping. The same response of the LSMO magnetic configuration was observed also for different widths of the half-ring structures.

As will be further explained in section 5.5, the observed response of the magnetic configuration of the LSMO half-ring structures at room temperature upon the injection of current pulses was interpreted as being due to Joule-heating effects, leading to a local heating of the LSMO half-ring structures to temperatures above the LSMO Curie temperature.

While the observed room-temperature hopping of the magnetic domain walls in the LSMO half-ring structures is detrimental for current-induced domain wall motion applications, these thermally-activated effects can be employed for the analysis of the energetics of the magnetic domain walls in LSMO. In fact, as can be observed in Fig. 5.10, the injection of current pulses

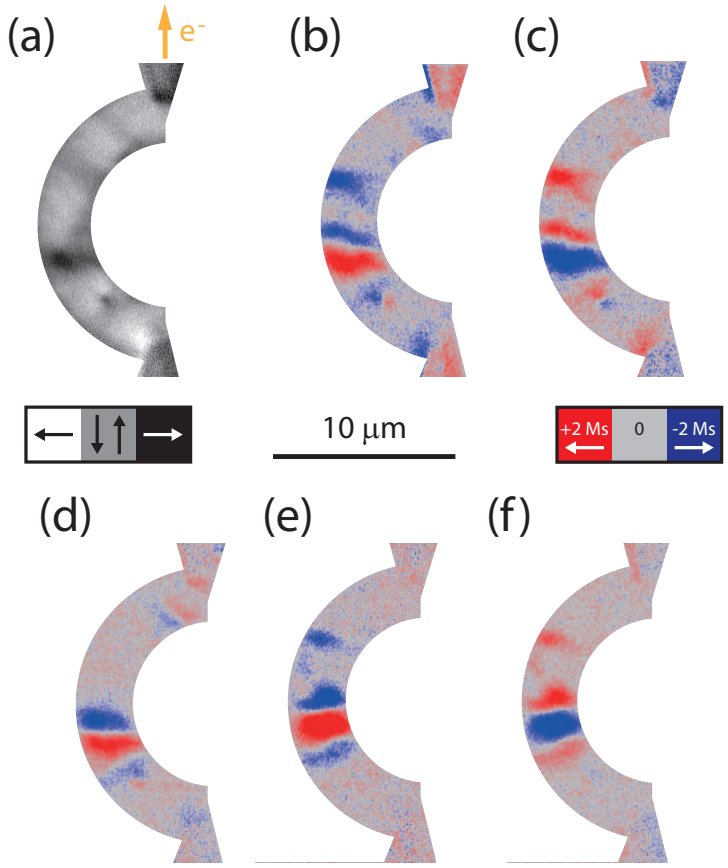

Figure 5.8: Hopping of a magnetic domain wall in a 2 μm wide LSMO half-ring structure following the injection of current pulses. The difference images, calculated according to the process described in the text and depicted in Fig. 5.7, are shown. (a) XMCD-PEEM image of the initialized half-ring structure; (b-f) Difference XMCD-PEEM images, each of which was calculated after the injection of a current pulse burst across the LSMO half-ring structure. It is possible to observe a hopping of the domain wall, superimposed with nucleation and annihilation of magnetic domains (top part of the half-ring structure). The grayscale bar indicates the direction of the magnetic contrast in (a), while the red/blue bar illustrates the interpretation of the color code in the difference images. Image adapted from Ref. [111].

across the LSMO half-ring structures leads to changes in the spin structure of the magnetic domain wall (a change of the domain wall configuration from the transverse to the vortex wall configuration is observed in the case shown in Fig. 5.10).

In general, the initialization of the magnetic configuration of the LSMO half-ring structures leads to the nucleation of a transverse magnetic domain wall, as shown in Fig. 5.10(a). The injection of current pulses across the LSMO half-ring structures leads, as shown in Fig. 5.10(b), to a transformation of the domain wall from the transverse to the vortex configuration

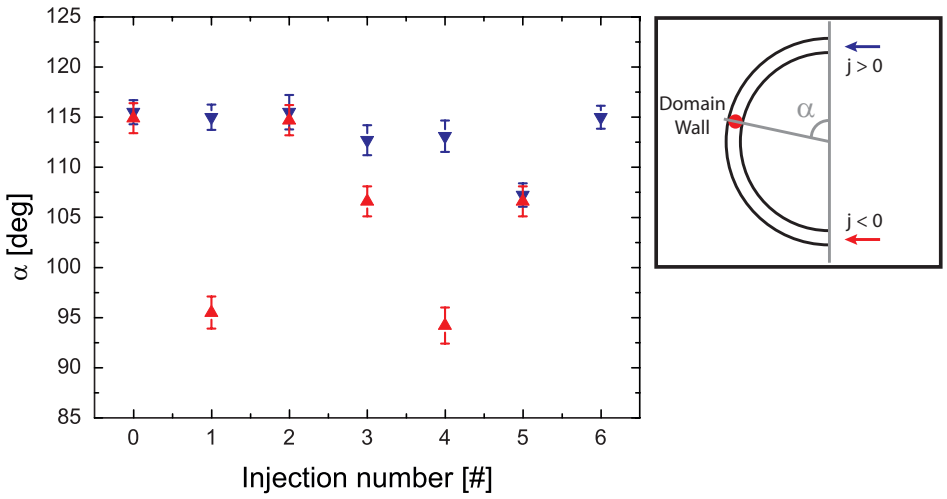

Figure 5.9: Position of the magnetic domain wall of an LSMO half-ring structure after the injection of current pulses of a current density of 4×10^{10} A m^{-2}. The inset indicates the convention for the position of the domain wall (indicated by the angle of the center of the domain wall) and of the sign of the current, where the red and blue arrows indicate the direction of the electron flow. Image adapted from Ref. [111].

[111, 116].

From the experimentally observed response of the domain wall configuration with respect to the injection of current pulses, it is found that the vortex domain wall is be energetically favored with respect to the transverse domain wall configuration (this response was observed for all of the analyzed LSMO half-ring widths): when a current pulse was injected across an LSMO half-ring structure exhibiting a vortex magnetic domain wall, a transformation of the domain wall spin structure from the vortex configuration to a different domain wall configuration was observed only in ca. 10% of the injection events (out of a total of ca. 20 pulse burst injection events). Instead, when a current pulse was injected across an LSMO half-ring structure exhibiting a transverse domain wall configuration, a transformation of the domain wall configuration from transverse to vortex was observed for all of the injection events. These observations provide, thus, another indication of the lower energy of the vortex wall configuration with respect to the transverse wall configuration.

In the few cases where the injection of a current pulse across the LSMO half-ring structures exhibiting a vortex domain wall caused a change of the domain wall configuration, it was observed that, in the vast majority of these events, the domain wall configuration transformed back into a transverse wall (with a couple of exceptions, where more complicated structures, such as double vortex walls were nucleated). This observation indicates that the vortex and transverse domain wall configurations are two meta-stable states for the analyzed LSMO half-ring structures. These empirical observations, as will be explained in further detail in section

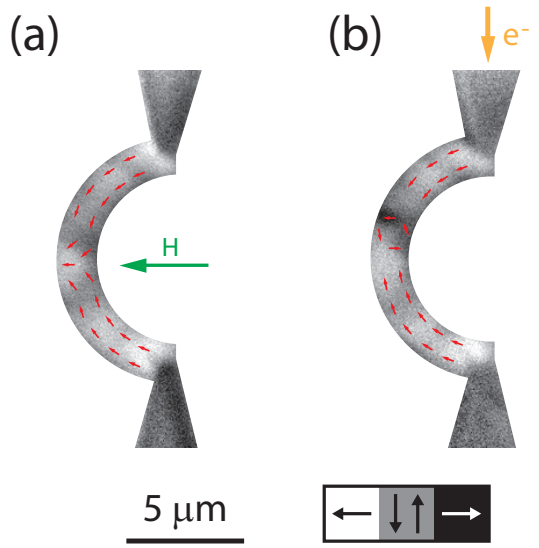

Figure 5.10: Transformation of the domain wall spin structure in LSMO half-ring structures following the injection of a current pulse across the nanostructure. (a) XMCD-PEEM image of an LSMO half-ring structure after initialization with an external magnetic field, showing a transverse domain wall; (b) XMCD-PEEM image of the same half-ring structure as in (a) after the injection of a current pulse burst with a current density of 3×10^{10} A m^{-2}, showing a vortex domain wall. The grayscale bar and the red arrows indicate the direction of the magnetic contrast in the images. The green arrow indicates the direction of the initialization field, and the orange arrow indicates the direction of the electron flow of the injected current pulses. Image adapted from Ref. [111].

5.5, are also confirmed by micromagnetic simulations of the LSMO half-ring nanostructures.

5.5 Results and discussion

The injection of current pulses across the LSMO half-ring structures initialized with a magnetic domain wall at the center of the half-ring structure leads, as shown by the experimental observations described in section 5.3, to a reduction of the depinning field (i.e. of the magnetic field required to depin the magnetic domain wall from the center of the half-ring structure). In particular, as shown in Fig. 5.5, the injection of current pulses with a low current density (i.e. $j \leq 8 \times 10^9$ A m^{-2}) across the LSMO half-ring structures gives rise to a reduction of the depinning field symmetric with respect to the polarity of the injected pulses. This response of the depinning field, also observed for other systems (such as Py [114]), is however not due to a contribution of the spin-transfer-torque effects, as it is symmetric with respect to the direction of the injected electrons with respect to the applied magnetic field. As in the case of Py [114], this reduction of the depinning field for low current densities can be explained

by the contribution of Joule-heating effects, which is independent from the direction of the injected electrons [112].

If current pulses with a high current density (i.e. $j > 8 \times 10^9$ A m^{-2}) are injected across the LSMO half-rings, it is possible to observe, as shown in Fig. 5.5, a reduction of the depinning field which is asymmetric with respect to the polarity of the injected pulses. In particular, the highest reduction of the depinning field was observed when the current pulses with a positive current density are injected across the half-ring structures (i.e. when the electrons flow antiparallel to the direction of the depinning field). If current pulses with a negative current density are injected (i.e. electrons flowing parallel to the direction of the depinning field), a constant value of the depinning field with respect to the current density was observed. Thus, in contrast with the observations carried out at lower current densities, the response of the depinning field to the injection of high current density pulses across the LSMO half-ring structure is a clear signal of a spin-transfer-torque contribution [112,114]. The constant value of the depinning field observed when electrons flowing parallel to the applied depinning field are injected in the LSMO is also expected (and was observed on other systems, such as Py [114]), as the measurements were carried out with a constant applied magnetic field, and the pulsed current is flowing across the LSMO half-ring structures only for a small fraction of the time when the magnetic field is applied. This implies that there cannot be an increase of the depinning field beyond the zero current case.

This asymmetric response of the depinning field with respect to the direction of the injected electrons can be employed for the estimation of the spin-transfer-torque efficiency of LSMO. This term describes the effect of the injected spin-polarized electrons on the magnetic configuration of the ferromagnetic material, and it can be estimated from the slope of the depinning field as function of the current density of the injected pulses. In the case of the LSMO half-ring structures analyzed in this chapter, it is possible, from the analysis of the data presented in Fig. 5.5, to determine a spin-transfer-torque efficiency of $\varepsilon \simeq 4 \times 10^{-14}$ T m^2 A^{-1} [112]. If this value is compared with the spin-transfer-torque efficiency of $3d$-based ferromagnetic materials such as Py [114], it is possible to observe that the spin-transfer-torque efficiency of LSMO is, as would be expected from its high spin-polarization and low saturation magnetization, about one order of magnitude larger than what observed for Py.

Besides allowing for a comparison of the effect of a spin-polarized electron on the magnetic configuration of different ferromagnetic materials, the spin-transfer-torque efficiency can be employed for the determination of the non-adiabaticity parameter β of the material. In particular, it is possible to express the spin-transfer-torque efficiency ε as function of the non-adiabaticity parameter β as follows [117]:

$$\varepsilon = \frac{\hbar \pi \beta P}{2 \mathrm{e} M_s \Delta}, \tag{5.1}$$

where β is the non-adiabaticity parameter, P the spin polarization and M_s the saturation

magnetization of the analyzed material, and Δ the width of the magnetic domain wall displaced by the spin-polarized current.

If a spin polarization $P \simeq 1$ [107], a saturation magnetization $M_s \simeq 3.2 \times 10^5$ A m^{-1} (determined from SQUID magnetometry measurements at 4 K of continuous LSMO thin films grown in the same conditions as the ones analyzed in section 5.3), and a width $\Delta \simeq 500$ nm (determined from XMCD-PEEM imaging of the LSMO nanostructures) are assumed for the LSMO nanostructures, it is possible to estimate, by inverting Eq. (5.1), a non-adiabaticity parameter of $\beta \simeq 5.8$ for the analyzed LSMO nanostructures [112] at a temperature of 4 K.

The calculated value of the non-adiabaticity parameter β for the LSMO is much higher than its damping constant α, which was determined, from ferromagnetic resonance measurements, to be $\alpha \leq 0.01$ [118]. Given this high difference between the damping constant α and the non-adiabaticity parameter β, it is possible to observe that spin relaxation is not the only contribution to the non-adiabaticity parameter, thus implying the existence of further mechanisms giving rise, due to their strong contribution to the non-adiabaticity parameter, to the observed difference between the α and β parameters of LSMO [21].

As already mentioned in section 5.3, upon the injection of current pulses with a current density higher than about 2×10^{10} A m^{-2} across the LSMO half-ring structures, abrupt changes in the resistance measured across the half-ring element were observed for some of the injection events. Such sudden and sharp changes in the measured resistance cannot, however, be explained by considering the sole contribution of spin-transfer-torque effects. Such events can, however, be explained by considering the contribution of resistive heating effects, which give rise to a local heating of the LSMO nanostructures to temperatures comparable (or above) its Curie temperature. As observed in the XMCD-PEEM measurements carried out at room temperature shown in section 5.4, such resistive heating effects lead to profound changes in the magnetic configuration of the LSMO half-ring structures (see e.g. Fig. 5.8), which can then affect the value of the magneto-resistance measured across the half-ring structure. It was possible to exclude contributions other than the changes in the magnetic configuration of the LSMO half-ring elements thanks to the possibility to recover the original value of the resistance by re-applying the initialization field to the LSMO half-ring structures. These Joule-heating effects are much stronger in LSMO if compared with $3d$ ferromagnetic materials due to the combination of a lower Curie temperature and a higher resistivity for the LSMO.

The response of the magnetic configuration of the nanostructured LSMO half-ring elements to high current-density pulses observed by transport measurements was confirmed by XMCD-PEEM imaging experiments carried out at room temperature, which results are described in section 5.4.

In particular, it was possible to observe that the initialization of the LSMO half-ring structures with the initialization field (see Fig. 5.1, where the direction of the initialization

field is indicated by a green arrow) leads to the nucleation of a transverse magnetic domain wall at the center of the half-ring structures, an example of which is shown in Fig. 5.10(a). In contrast to what observed at low temperatures, the room-temperature injection of current pulses where, at low temperatures, a clear spin-transfer-torque effect was observed, leads to strong changes in the magnetic configuration of the LSMO half-ring structure, dominated by Joule-heating effects. These Joule-heating effects, which at lower temperatures become relevant for current pulses of densities above about 2×10^{10} A m^{-2}, are also relevant, at room temperature, for lower current densities. This is due to the proximity of the Curie temperature ($T_c \simeq 360$ K for the LSMO thin films analyzed in this chapter [108]) to room temperature: the crossing of the Curie temperature of the LSMO due to the Joule-heating effects leads to profound changes in the magnetic configuration [109].

The room temperature XMCD-PEEM measurements evidenced a Joule-heating induced hopping of the magnetic domain walls in the LSMO half-ring structures, superimposed with annihilations and nucleations of magnetic domains and domain walls, as shown in Fig. 5.8. This errant behavior for the position of the magnetic domain wall upon the injection of current pulses, shown in Fig. 5.9, does not exhibit any clear signature of the contribution of spin-transfer-torque effects, in contrast with analogous observations carried out on $3d$ ferromagnetic materials such as Py [103].

The injection of current pulses across the LSMO half-ring structures leads, as shown in Fig. 5.10, to changes in the magnetic configuration of the magnetic domain wall nucleated at the center of the half-ring structure. The application of the initialization field to the LSMO half-ring structures leads to the nucleation of transverse magnetic domain walls, as shown in Fig. 5.10(a). However, as shown in Fig. 5.10(b), the injection of a current pulse across the LSMO half-ring structure leads to a transformation of the domain wall from the transverse to the vortex wall configuration. By injecting further pulses across the LSMO half-ring structures, it was possible to reach the qualitative conclusion that both the vortex and transverse domain wall configurations exhibit, for the analyzed LSMO half-ring structures, comparable domain wall energies, and they both constitute meta-stable states. Moreover, by injecting several series of current pulses across the LSMO half-ring structures, it was possible to observe that the vortex wall configuration appears to be energetically lower lying than the transverse wall configuration.

The empirical observation that the vortex domain wall exhibits a lower domain wall energy if compared to transverse walls for the analyzed geometries was verified by micromagnetic simulations, where the magnetic free energy of different LSMO half-ring geometries (i.e. a constant diameter of 10 μm with varying widths w was considered for the micromagnetic simulations) with a vortex and transverse domain wall was simulated.

The LSMO nanostructures were simulated[5] by solving numerically the LLG equation with the *MicroMagnum* framework [25] (more details about the micromagnetic simulations can be found in section 1.7). For the LSMO nanostructures, a saturation magnetization of $M_s \sim 2 \times 10^5$ A m^{-1} and an exchange stiffness of $A \sim 1.5 \times 10^{-12}$ A m^{-1} were employed in the calculations [111]. With these parameters, an exchange length of $l_{\mathrm{ex}} \sim 7.7$ nm results. The micromagnetic simulations were thus carried out with a discrete cell of 5×5 nm^2 in the xy plane, and of 30 nm in the z direction, corresponding to the thickness of the LSMO nanostructures (it is assumed that the magnetic configuration of the LSMO nanostructures does not vary within the z direction). As shown in Fig. 5.6(b), the micromagnetic simulations agree well with the measured magnetic states. By properly choosing the starting condition for the micromagnetic simulations, it was possible to simulate both vortex and transverse wall configurations, and to determine the energy of these two domain wall configurations.

The results of the micromagnetic simulations of the energy difference between the vortex and transverse wall configurations are shown in Fig. 5.11. These results confirm the experimental observations: as shown in Fig. 5.11, the transverse domain wall configuration is energetically lower-lying only for widths of the half-ring structure smaller than ca. 100 nm (for widths of the half-ring structure below 50 nm, only the transverse wall could be stabilized in the simulations: the vortex wall was expelled from the magnetic nanostructure, and the domain wall evolved to a transverse wall configuration).

It is also possible to employ a theoretical model for the description of the energy of the different domain wall configurations. In particular, it is possible to describe the energy of the transverse domain wall configuration using a 1D model, and a simplified model can be used for the description of the energy of the vortex domain wall configuration [111, 119, 120]. Using this simplified model, the energy of the transverse and vortex wall configurations (E_{TW} and E_{VW} respectively) can be written as follows:

$$E_{\mathrm{TW}} = 4wt\sqrt{AK}, \tag{5.2}$$

$$E_{\mathrm{VW}} = 2\pi At\,\log(w) + E_{\mathrm{VC}}, \tag{5.3}$$

where w and t are the width and thickness of the half-ring structure, respectively, A is the exchange stiffness, K is the magnetic anisotropy term, and E_{VC} is the energy of the vortex core. It is thus possible to calculate the energy difference between the two magnetic domain wall configurations as follows:

$$\mathrm{E}(w) = \mathrm{E}_{\mathrm{TW}}(w) - \mathrm{E}_{\mathrm{VW}}(w) = 4wt\sqrt{AK} - 2\pi At\log(w) - E_{\mathrm{VC}}. \tag{5.4}$$

This theoretical calculation can then be fitted to the simulated data, using the vortex core energy E_{VC} as fitting parameter.

[5] The micromagetic simulations presented in this chapter were carried out by B. Krüger at the University of Mainz.

In the case considered here, the anisotropy term in Eq. (5.2) is only given by the contribution of shape anisotropy [119]. This term is dependent on the aspect ratio of the half-ring structure. The dependence of the shape-anisotropy term K with respect to the geometry of the half-ring structure can be estimated from the model described in Ref. [121], where it may be expressed as follows:

$$K = 1 - \frac{1}{\pi}\left[\left(1 - \frac{w^2}{t^2}\right)\frac{t}{2w}\log\left(1 + \frac{w^2}{t^2}\right) + \frac{w}{t}\log\left(\frac{w}{t}\right) + 2\arctan\left(\frac{t}{w}\right)\right] \tag{5.5}$$

Thus, by combining Eqs. (5.4) and (5.5), and using the energy of the vortex core E_{VC} as fitting parameter, it is possible to find a good agreement between the description of the energy difference between the transverse and vortex wall configurations and the micromagnetic simulations, as shown by the black line in Fig. 5.11.

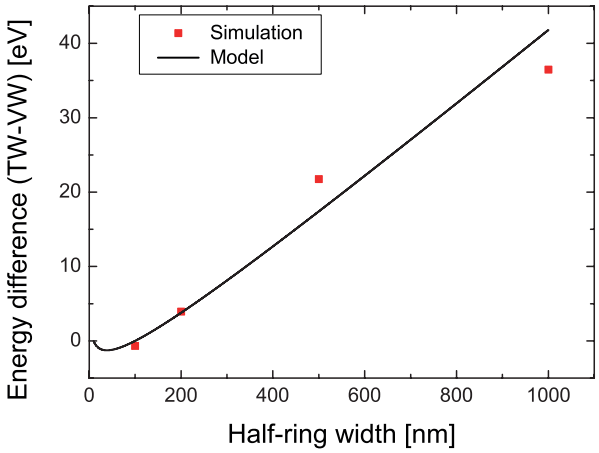

Figure 5.11: Difference between the domain wall energies for transverse and vortex wall configurations in LSMO nanostructured half-rings of 10 μm diameter at a temperature of 0 K. The data points illustrate the difference of the transverse and vortex wall energies determined using micromagnetic simulations, and the line illustrates the 1D model described in the text. Image adapted from Ref. [111].

From the theoretical description introduced above, it is possible to observe, as shown in Fig. 5.11, that the vortex domain wall configuration has a lower energy than the transverse wall configuration for LSMO half-ring structures wider than 100 nm, providing confirmation that the experimental observations are in line with the expectations from the theoretical models.

It should also be noted that both the micromagnetic simulations and the theoretical description given in (5.4) and in Fig. 5.11 were carried out at a sample temperature of 0 K. If the temperature of the sample is increased, both the saturation magnetization M_s and the exchange energy decrease (see e.g. Ref. [108], where the response of the saturation magnetization of a 30 nm-thick LSMO film is shown). The change of both the exchange energy and

the saturation magnetization will give rise to a different magnitude of the energy difference between the vortex and transverse wall configurations. However, it is expected that the qualitative dependence of the energy difference between the two domain wall configurations will hold also at higher temperatures [111].

5.6 Conclusions and summary

Thanks to its combination of low saturation magnetization at room temperature and its half-metallic behavior (i.e. full spin polarization at the Fermi energy) [107, 108], LSMO is interesting for spin-transfer-torque applications. In contrast to Fe_3O_4 and CrO_2, LSMO exhibits the additional advantage of a low magneto-crystalline anisotropy [108], which allows for the tailoring of the magnetic domain walls purely by shape anisotropy, as confirmed by XMCD-PEEM imaging of nanostructured LSMO elements [28, 109]. This provides a further incentive to analyze the response of this material to spin-polarized currents.

As shown in section 5.2, nanostructured LSMO half-ring elements were fabricated from LSMO thin films heteroepitaxially deposited on STO (001) substrates with a multi-step lithographical processing. A half-ring geometry was selected for the experiments presented in this chapter as it allows for a simple nucleation of a magnetic domain wall at the center of the nanostructured elements. The response of this magnetic domain walls to the application of a spin-polarized current was then analyzed by low-temperature transport measurements, described in section 5.3, and by room-temperature XMCD-PEEM imaging, described in section 5.4.

As described in section 5.3 and discussed in section 5.5, low-temperature transport measurements, aimed at the determination of the response of the depinning fields in LSMO to the application of a spin-polarized current, were carried out. After the initialization of the magnetic configuration of the LMSO half-ring structures with a magnetic field (which, as shown in Fig. 5.3, allows for the nucleation of a domain wall at the center of the half-ring structures), a constant magnetic field was applied along the axis of the half-ring structures, and the effect of the injection of spin-polarized current pulses on the magnitude of the depinning field was analyzed. As shown in Fig. 5.5, the injection of current pulses across the LSMO half-ring structures leads to a reduction of the magnitude of the depinning field. The observed reduction of the depinning field is, for large current densities, asymmetric with respect to the polarity of the injected pulses (i.e. with respect to the direction of the injected electrons), providing a clear signature of the contribution of spin-transfer-torque effects. By analyzing the slope of the depinning field with respect to the current density of the injected pulses, it is possible to calculate a spin-transfer-torque efficiency (at low temperatures) of $\varepsilon \simeq 4 \times 10^{-14}$ T m^2 A^{-1} [112], one order of magnitude higher than what was observed in Py [114]. The calculation

of the non-adiabaticity parameter from (5.1) also allowed for the observation that, for LSMO, the non-adiabaticity parameter is much larger than the damping constant (i.e. $\beta \simeq 5.4$, versus a Gilbert damping $\alpha \leq 0.01$), implying that mechanisms other than spin relaxation contribute substantially to the non-adiabaticity parameter for LSMO.

The injection of high current-density pulses (i.e. for $j \geq 2 \times 10^{10}$ A m^{-2}) across the LSMO half-ring structures (at a temperature of 4 K) led, in some of the injection events, to a strong change in the magnetic configuration of the half-ring structures, which could not be justified by considering the sole contribution of spin-transfer-torque effects. These strong changes in the magnetic configuration of the nanostructured LSMO elements were interpreted to be due to Joule-heating effects. These observations were confirmed, as shown in section 5.4 and discussed in section 5.5, by room-temperature XMCD-PEEM imaging measurements. As shown in Figs. 5.8 and 5.9, the injection of current pulses across the LSMO half-ring structures causes profound changes in the magnetic configuration of the LSMO nanostructures. In particular, a hopping of magnetic domain walls between different pinning sites in the LSMO half-ring structures, combined with nucleation and annihilation events of magnetic domains (and domain walls) was observed upon the injection of current pulses across the half-ring structures. Like in the case of the transport measurements, these strong changes of the magnetic configuration were interpreted as being due to Joule-heating effects arising from the injection of the higher current pulses.

The sudden Joule-heating induced changes of the magnetic configuration of the LSMO nanostructures observed at room temperature upon the injection of current pulses are detrimental for the applicability of this material in spin-torque-based devices, but these heating-induced changes of the magnetic configuration of the LSMO allowed for an in-depth analysis of the energetics of the magnetic domain walls. Experimentally, it was possible to observe that, for the analyzed half-ring geometries, the vortex wall configuration lies at a lower energy with respect to the transverse wall configuration. These qualitative observations were confirmed, as shown in Fig. 5.11, by an analysis of the energetics of the domain walls both with micromagnetic simulations and with a theoretical model.

In conclusion, it was possible to observe that LSMO exhibits, as expected from its material properties, a high spin-transfer-torque efficiency. However, due to its higher resistivity if compared to 3*d* ferromagnetic metals and to its lower Curie temperature, Joule-heating effects give rise to serious issues in the performance of this material upon the injection of current pulses. Thus, if this interesting material is to be employed for current-induced domain wall motion applications, it is necessary to reduce the influence of Joule-heating effects, allowing the material to not cross the Curie temperature upon the injection of the current pulses. The improvement of the quality of the LSMO could be carried out, for example by acting on the growth and patterning phases, where defects that increase the resistivity of the material

(and give rise to magnetic pinning sites) may form. Another possible approach aimed at the reduction of the Joule-heating effects could also be to inject multiple pulses of low time duration and high duty cycle, thus reducing the heating of the nanostructured elements caused by a single pulse, and allowing the nanostructure to dissipate the heat prior to the injection of the following pulse.

The results presented in this chapter regarding the study of the current induced magnetic domain wall motion at low temperatures in nanostructured LSMO elements have been published in the Journal *Applied Physics Letters* [112], and the results on the study of current induced domain wall hopping in nanostructured LSMO elements at room temperature have been published in the *Journal of Physics: Condensed Matter* [111].

Chapter 6

Conclusions and future outlooks

6.1 Conclusions

In this thesis, the effect of shape, strain and spin-polarized currents on the magnetic properties of nanostructured ferromagnetic materials has been investigated. As shown in the thermodynamical description of magnetism given in chapter 1, each of these mechanisms allows for the field-free control of different terms of the magnetic free energy. The effect of the manipulation of these single terms of the magnetic free energy was experimentally determined by high-resolution XMCD-PEEM imaging, as described in further detail in chapter 2.

As described in chapter 3, the fabrication of nanostructured elements of different geometries allows for the control of their magnetic configuration due to shape anisotropy, which is necessary to tailor their magnetic properties meet specific requirements necessary for their application in devices. This is carried out by influencing the stray field (and anisotropy) terms of the magnetic free energy through the selection of the geometry of the nanostructured elements. In this chapter, the magnetic properties of nanostructured Fe_2CrSi and Co_2MnGa Heusler compound elements were investigated, which is a first step for the application of Fe_2CrSi and Co_2MnGa both in additional experimental characterizations and in eventual spintronic devices.

As described in chapter 4, the search of current-free methods to manipulate the magnetization configuration of a magnetic material has motivated numerous investigations on multiferroic materials, i.e. materials exhibiting more than one ferroic order, where the single ferroic orders are coupled with each other. In this chapter, the possibility to control the magnetization in an artificial multiferroic material through the magneto-elastic coupling effect was demonstrated. The artificial multiferroic system investigated in this chapter was fabricated by combining a piezoelectric and a magnetostrictive material. In particular, the response of the magnetization of nanostructured Ni elements upon the application of a piezoelectric strain was quantitatively characterized. This allowed us to determine that the response of

these nanostructured elements is well described by a simple magneto-static model, where the magneto-elastic coupling is described as an additional magnetic anisotropy term to the magnetic free energy. Moreover, it was observed that the nanostructuring of the magnetostrictive material does not induce substantial modifications of its response to the application of a strain, as it was possible to describe its response with bulk-like parameters.

As described in chapter 5, the injection of a spin-polarized current in a magnetic material can influence its magnetic configuration through the spin-transfer-torque effect. In particular, spin-polarized currents can displace magnetic domain walls in nanostructured elements, providing a novel, highly-scalable approach to magnetic data storage. In this chapter, the effects of the injection of a spin-polarized current across nanostructured elements of the magnetic oxide $La_{0.7}Sr_{0.3}MnO_3$ have been investigated. At a temperature of 4 K, it was observed that this material exhibits a very high spin-transfer-torque efficiency, given by the combination of its relatively low saturation magnetization and high spin polarization. However, if the material is heated to room temperature, a different response of the magnetic configuration upon the injection of a spin-polarized current is observed: the changes in the magnetic configuration are dominated by Joule-heating effects, which cause the local heating of the LSMO to temperatures above its Curie temperature, hinting that a further optimization of the materials properties needs to be carried out if this material is to be employed for spintronic applications.

In conclusion, the results presented in this thesis are an overview of some of the approaches that can be employed to achieve the control of the magnetic configuration of a material without the application of a magnetic field in applications-relevant conditions.

6.2 Outlooks

In this section, a brief overview of some of the outlooks for this thesis will be presented. In particular, possible future experiments based on the results presented in the chapter 4 of this thesis will be described.

6.2.1 Magnetization dynamics in magnetostrictive materials

As further discussed in chapter 1, the dynamical response of the magnetization $\mathbf{M}$ of a material upon the application of an external field can be described with the LLG equation, given in Eq. (1.29) (see section 1.5). The first term on the right side of Eq. (1.29), given by $-\gamma\mathbf{M} \times \mathbf{H}_{\text{eff}}$, gives rise to a dependence of the time derivative of the magnetization $\dot{\mathbf{M}}$ from Brown's effective field $\mathbf{H}_{\text{eff}}$, whose analytical form is given in Eq. (1.22).

As shown in Eq. (1.22) and discussed in section 1.3, Brown's effective field depends on the exchange energy, the Zeeman field (i.e. on externally applied magnetic fields), the stray field generated by the magnetic moments in the material, and on the magnetic anisotropy energy.

Thus, as would be phenomenologically expected, a change in the magnetic anisotropy of a magnetic material modifies both the statical and the dynamical response of its magnetization upon an external stimulus.

As shown in chapter 4, the application of a strain to a magnetostrictive material gives rise to an additional magnetic anisotropy term K_{ME} that contributes to the magnetic free energy density. The experiments described in chapter 4 were carried out in the quasi-static regime, i.e. the changes in the strain applied to the magnetic structures were applied on a timescale much longer than the timescales involved in the magnetization dynamics (i.e. 10^{-9} - 10^{-12} s).

The dynamical processes involved in the magneto-elastic coupling have however not been yet fully clarified. In particular, the presence of a magnetic anisotropy energy which is dynamically varying at the same timescale of the magnetization dynamics is of interest. To ascertain the effects of strain variations on the magnetization dynamics, a strain variation on timescales comparable to those of the magnetization dynamics is necessary to obtain a non-quasi-static anisotropy term in the LLG equation. Piezoelectric materials where the strain is generated by applying a voltage across the material, such as the case described in chapter 4, do not allow for strain variations on the magnetization dynamic timescales, since fast variations of the applied strain will damage the piezoelectric material. Moreover, in order to experimentally analyze the influence of an applied strain to the magnetization dynamics, it is necessary to employ a *pump-probe* approach, schematically depicted in Fig. 6.1, where the excitation (in this case, the strain variation) is generated by a *pump* signal (on timescales comparable to those of the dynamical process), and the magnetization state is probed by a *probe* signal, with a defined and controllable time delay from the pump signal. The pump-probe experiment is then repeated for different delays between the pump and probe signals and, by combining the acquired data, the dynamics can be resolved.

Experiments carried out with the pump-probe approach need to guarantee a complete reproducibility of the dynamics of the analyzed samples, as many repetitions of the excitations need to be carried out to determine the state of the sample at the different time-delays between the pump and probe signals. This implies that the pump-probe experiments have to be designed in order to guarantee the exact recovery of the initial state after each excitation, which also has to occur within the repetition time of the pump-probe experiment (i.e. before the sample is once again excited by the pump signal).

Different possible experiments involving the analysis of the dynamics of the magneto-elastic coupling can be carried out by employing the pump-probe mechanism, two of which will be described in the upcoming sections. The first proposed experiment determines the magnetization dynamics (such as the gyration frequency of magnetic vortex cores) of a magnetostrictive material as function of the strain applied to the material. The second proposed experiment pertains to the study of the magnetization dynamics of a nanostructured magnetostrictive

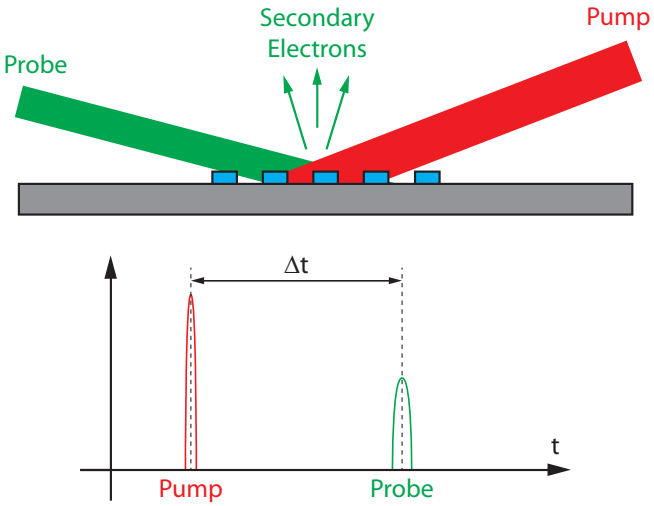

Figure 6.1: Sketch of a pump-probe experimental concept, employed for the analysis of dynamical processes. The material is excited with a pump signal (e.g. a fs-laser pulse) at a given time, and the material properties (e.g. the magnetization configuration) is probed by a probing signal (e.g. x-ray photons) at a given time difference Δt from the pump signal. By probing the material properties at different time delays Δt, it is possible to determine the dynamics of the analyzed processes.

material upon the application of a strain at timescales comparable with the magnetization dynamics.

6.2.2 Magnetization dynamics as function of an applied static strain

As shown in Eqs. (1.29) and (1.22) and discussed in chapter 1, the dependence of the time evolution of the magnetization $\mathbf{M}$ on the anisotropy energy implies that the dynamical response of the magnetization will be affected by the anisotropy of the material, as has been theoretically predicted [122]. As shown in chapter 4, the anisotropy energy of a magnetostrictive material can be reliably and reproducibly controlled by growing the magnetostrictive material on top of a piezoelectric substrate, which is then employed to deform the magnetostrictive material by the application of an electric field.

As shown e.g. in Fig. 4.16, large variations of the anisotropy energy of nanostructured magnetostrictive elements fabricated on top of a piezoelectric substrate can be obtained by the application of an electric field. Such changes in the anisotropy energy imply also a change in the dynamical response of the magnetization of such nanostructured elements, which then reflects in the modification of measurable properties such as e.g. the gyration frequency of the magnetic material.

The dynamical response of a magnetostrictive material upon different applied strains (i.e.

different magneto-elastic anisotropies) has been analyzed with the help of micromagnetic simulation (see Ref. [122] for the micromagnetic simulations carried out on Galfenol nanostructures), which determined, by solving numerically the LLG equation for different magnetic anisotropies, that strong changes in the dynamical response of these materials can be attained by the application of a piezoelectric strain. The different dynamical response of the magnetization configuration of a 2 μm Ni square (with the same parameters as the Ni nanostructures analyzed in chapter 4 and a damping constant $\alpha = 0.045$ [123]) as function of the different anisotropy (induced by the magneto-elastic coupling) has been simulated with the help of the *MicroMagnum* framework [25], and the results of some of these simulations are shown in Fig. 6.2.

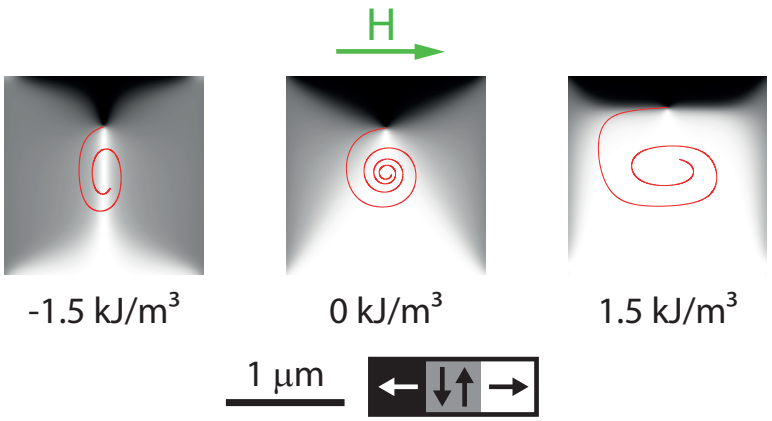

Figure 6.2: Micromagnetic simulations of the relaxation process of a nanostructured Ni square after the application of a magnetic field of 2 mT along the x direction for different magnitudes of the (magneto-elastic) uniaxial anisotropy. The path of the vortex core in the first 100 ns of the simulation is indicated by the red lines in the images. Clear changes in the trajectory of the vortex core induced by the different magnitudes of the uniaxial anisotropy can be observed.

In Fig. 6.2, the dynamical response of a nanostructured Ni square with different applied (quasi-static) strains (inducing a different magneto-elastic anisotropy) after the application of a magnetic field of 2 mT in the x direction has been simulated. From the simulations, the position of the vortex core (i.e. the center of the magnetic flux-closure state) can be determined as function of time, as shown in Fig. 6.3.

As shown in Fig. 6.3, the different deformation of the Ni nanostructure leads to a different dynamical response of the vortex core. These differences in the dynamical response of the magnetization can also be observed in the different eigenfrequency of the precession of the vortex core around its equilibrium position, as shown in Fig. 6.4. From the dynamical response of the magnetization configuration (in this particular case, of the vortex core), it is possible to describe the dynamical movement of the vortex core with the following damped spring-like

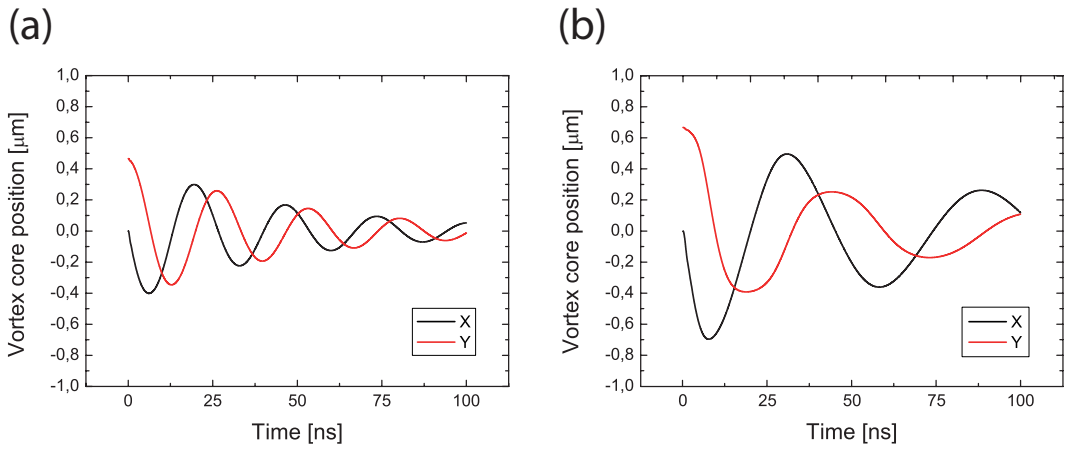

Figure 6.3: Simulated position of the vortex core as function of time at an applied uniaxial anisotropy of (a) 0 kJ m^{-3} and (b) 1.5 kJ m^{-3} along the x direction after the application of a magnetic field of 2 mT along the x direction. A clear difference in the gyration dynamics can be observed for the different applied anisotropies.

equation of motion, with an additional term describing the vortex core gyration [124]:

$$\underline{\underline{M}}\ddot{\mathbf{r}} - \mathbf{G} \times \dot{\mathbf{r}} - D\dot{\mathbf{r}} + \nabla U(\mathbf{r}) = 0, \tag{6.1}$$

where $\mathbf{r}$ is the position of the vortex core, $\underline{\underline{M}}$ the effective mass tensor of the vortex core, $\mathbf{G}$ the gyrovector describing the gyroforce experienced by the moving vortex core [125], D a damping term proportional to the Gilbert damping α, and $U(\mathbf{r})$ the potential energy for the vortex core. The potential energy $U(\mathbf{r})$ has to be estimated for the different magnitudes of the magneto-elastic anisotropies, and will give rise to a different potential well, which will affect the dynamical response of the excited vortex core. Thus, by analyzing the dynamical response of a magnetostrictive material as function of the applied strain, it would be possible to determine the effect of the magneto-elastic anisotropy term on the potential energy $U(\mathbf{r})$ and on the mass tensor $\underline{\underline{M}}$ of the vortex core, which governs the dynamics.

It is possible to access the magnetization dynamics experimentally with a pump-probe approach. An in-plane magnetic field pulse on the nanosecond timescale, which would lead to a dynamical response similar to the one simulated in [122] and to the one described above, can be generated by the injection of a fast current pulse across a planar strip-line as described e.g. in Ref. [126]. Thus, a fast magnetic field pulse can be applied to magnetic nanostructures fabricated on top of a strip-line.

In order to control the anisotropy condition of the magnetic nanostructures, the strip-line has to be fabricated on top of a piezoelectric substrate, with the magnetostrictive nanostructures fabricated on top of the strip-line itself, as schematically shown in Fig. 6.5.

The field-induced dynamics of the magnetization configuration of the magnetostrictive

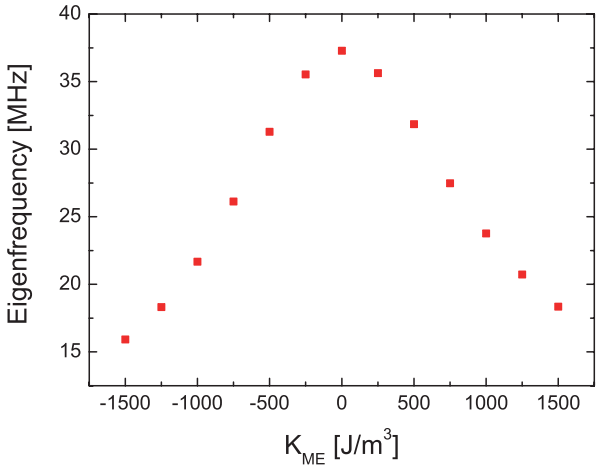

Figure 6.4: Simulated eigenfrequency of the magnetic vortex core in a 2 μm wide Ni square along the x direction as function of the magnitude of an uniaxial anisotropy with its axis along the x direction. The asymmetric response with respect to the sign of the anisotropy is caused by the excitation of the Ni structure with a magnetic field along the x direction.

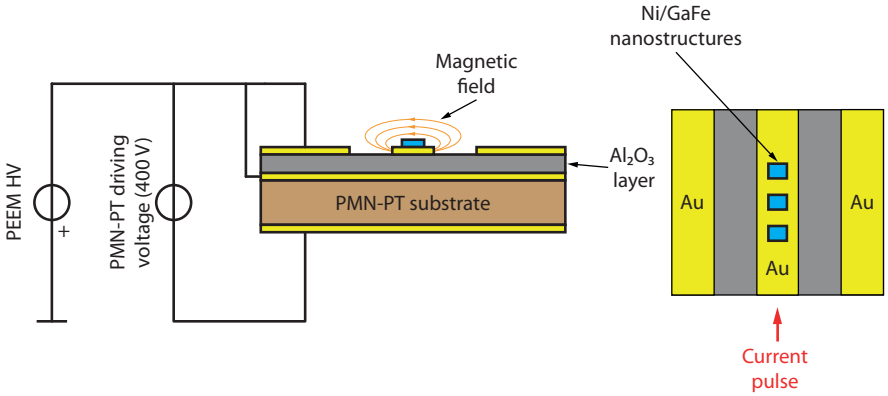

Figure 6.5: Schematic overview of the sample proposed for the control of vortex core dynamics with the magneto-elastic coupling. The magnetic nanostructures are fabricated on top of a strip-line, which generates, through the injection of a current pulse, a magnetic field pulse that excites the dynamics of the nanostructures. The strip-line (and the magnetostrictive nanostructures) are fabricated on top of a piezoelectric substrate, employed to generate a magneto-elastic anisotropy in the nanostructures.

nanostructures can then be imaged by time-resolved XMCD-PEEM, in a similar fashion as described in Ref. [126]. The current pulse that generates the pulsed magnetic field can be achieved either using a fast photodiode illuminated by a laser pulse [126], or with a pulse generator. To guarantee that the fast current pulse is correctly injected across the strip-line (thus generating the magnetic field pulse), it is necessary to fabricate an impedance-matched

strip-line, as a mismatch in the impedance of the strip-line with respect to the rest of the electrical circuit (conventionally matched to an impedance of 50 Ω) will lead to a reflection of the electrical pulse at the connection with the strip-line.

The fabrication of an impedance-matched strip-line on top of a piezoelectric material, as schematically shown in Fig. 6.5, is, thus, the first step to be undertaken. Test samples, with different geometrical structures for the strip-line have been fabricated, and their electrical performances have been characterized. As shown in Fig. 6.6, it is possible to fabricate strip-line structures with a good electrical performance. Further optimizations of the strip-line geometry are currently being carried out, in order to reduce the influence of the over- and undershoot of the short pulse transmitted across the structure, and obtain a better impedance matching.

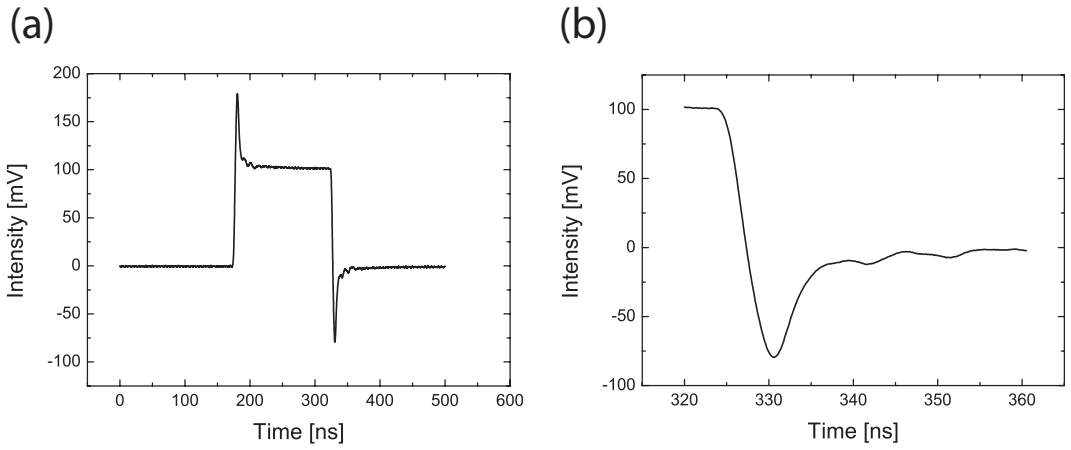

Figure 6.6: (a) Oscilloscope trace of a current pulse injected across an Au strip-line fabricated on a PMN-PT substrate (width of 10 μm, thickness of 20 nm and a distance of 10 μm from the ground plane). (b) Detail of the oscilloscope trace shown in (a) for the falling edge, showing a fall time of ca. 5 ns, followed by an undershoot of the signal of about 75 mV. The injected current pulse had an amplitude of 1 V, a 150 ns width, and a rising/falling time of 5 ns.

Once the geometry of the strip-line has been optimized, magnetostrictive nanostructured elements of different geometries will be fabricated on top of the strip-line, and the magnetization dynamics of these elements will be analyzed by time-resolved XMCD-PEEM imaging. In the case that the dynamics of the relaxation process of the vortex core cannot be resolved due to the effect of the unavoidable pinning sites on the nanostructured elements, an alternative approach could be the resonant excitation of the magnetic nanostructures by the injection of an alternating current across the strip-line (i.e. by an alternating magnetic field). These experiments are scheduled to take place in one of the upcoming beamtimes in the second semester of 2015.

6.2.3 Magnetization dynamics of a magnetostrictive material upon strain variations at the sub-ns timescale

The experiments proposed in section 6.2.2 will allow for the analysis of the influence of the magneto-elastic effect on the dynamical response of magnetostrictive nanostructured elements, e.g. by determining the effective mass of a magnetic vortex core as function of the static strain applied to the nanostructured elements. For these experiments, the dynamical response of the magnetization **M** can be described by the LLG equation, where the effect of the applied strain is included in the Brown's effective field as an additional magnetic anisotropy term. As the applied strain static (i.e. it can be considered constant with respect to the timescale of the magnetization dynamics), the additional magnetic anisotropy term included in the Brown's effective field can be assumed as constant, thus hindering the possibility of analyzing the effects of a dynamically varying magneto-elastic anisotropy term with the experiments proposed in section 6.2.2.

To study the dynamical processes involved in the magneto-elastic coupling, it is necessary to generate a strain variation in the magnetostrictive material on a timescale comparable with the one of the magneto-dynamical processes. It is, however, not possible to employ a piezoelectric material such as PMN-PT to generate such strain variation, due to the damages (such as cracking) that occur in the substrate when the electric field applied across the substrate changes on a short timescale. Fortunately, it is also possible to generate fast strain variations with non-piezoelectric materials [127–129]. In particular, in this section, the use of the Mott insulator VO_2 to generate an ultra-fast strain variation will be discussed.

VO_2 is a Mott insulator which exhibits a metal-to-insulator phase transition (MIT) at a temperature of ca. 330 K, where a change of the resistivity of ca. four orders of magnitude from a low temperature insulating phase to a high temperature conductive phase has been observed [130]. Along with the resistivity changes, the material undergoes a structural phase transition, where the crystalline lattice changes from a low temperature monoclinic to a high temperature rutile phase [131]. Across the phase transition, surface strains comparable to the ones achievable with piezoelectric substrates are generated [131, 132]. Those strains can then be employed to influence the magnetic properties of a magnetostrictive material fabricated on top of the VO_2 [133].

A preliminary observation of the effect of the MIT of the VO_2 onto the magnetic properties of a magnetostrictive material is described in Ref. [133], where strong changes of the coercive field of a continuous Ni film were observed upon the thermal excitation of the MIT. A similar result was also observed in a recent PEEM beamtime[1], where nanostructured Ni elements

[1]These measurements were carried out at the SIM (X11MA) beamline at the Swiss Light Source [65, 66] and at the CIRCE beamline at ALBA [69].

(with a thickness of 20 nm) fabricated[2] on top of a 15 nm thick VO_2 thin film grown on a TiO_2 (100) substrate (for the growth details, see Ref. [134]). As shown in Fig. 6.7, where the magnetic configuration of a 2 μm wide Ni square fabricated on top of a VO_2 thin film grown on a TiO_2 (100) substrate are shown, the excitation of the MIT leads to changes in the magnetic configuration of the magnetostrictive elements. In particular, the excitation of the MIT leads to a change in the uniaxial anisotropy of the Ni nanostructured element of about 1.5 kJ m^{-3}, value obtained by comparing the magnetic configuration of the Ni structure with micromagnetic simulations.

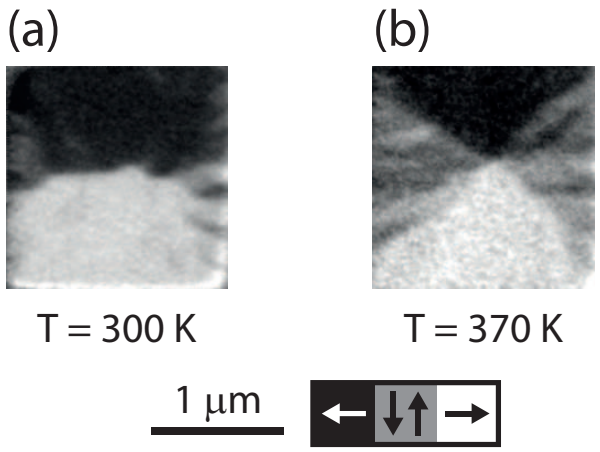

Figure 6.7: XMCD-PEEM images of a 2 μm wide Ni square fabricated on top of a VO_2 thin film (a) at room temperature and (b) at a temperature of 370 K. A clear change in the magnetic configuration of the nanostructured Ni element, induced by the crossing of the MIT of the VO_2 and the resulting strain change can be observed.

As shown in Fig. 6.7 it is possible, by exciting the MIT of the VO_2, to control, at least in a quasi-static regime, the magnetic configuration of a magnetostrictive nanostructured element.

As mentioned above, the MIT of the VO_2 can also be employed to generate strain variations at timescales comparable with those of the magnetization dynamics. As described in Refs. [127–129], it is possible to excite the MIT of the VO_2 at nanosecond timescales by illuminating the material with a fs-laser pulse at a wavelength of about 800 nm. Thus, an experiment that can be attempted is the time-resolved investigation of the magnetization dynamics of magnetostrictive nanostructures fabricated on top of a VO_2 thin film excited by a fs-laser pulse. A possible experimental geometry for the time-resolved analysis of the magneto-elastic effect is shown in Fig. 6.8(a).

As shown in Fig. 6.8(a), the VO_2 thin film on top of which magnetostrictive nanostructures are fabricated, is illuminated with a fs-laser pulse (exciting the MIT), and the magnetic

[2]The VO_2 thin films were fabricated at the IBM Almaden Research Laboratories by a collaborating group.

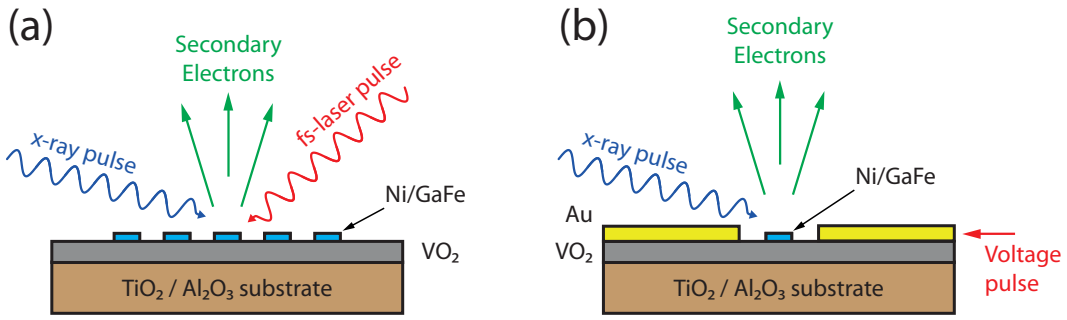

Figure 6.8: Proposed sample setup for the investigation of the dynamics of the magneto-elastic coupling by exciting the MIT of VO_2 at the timescales of the magnetization dynamics. (a) Optical excitation of the MIT of the VO_2 by illuminating the material with a fs-laser pulse; (b) Electrical excitation of the MIT of the VO_2 by injecting a current pulse across the VO_2.

configuration of the magnetostrictive nanostructures is probed at a variable delay by an x-ray pulse. Preliminary test measurements with the experimental setup proposed in Fig. 6.8(a) have been attempted, uncovering however issues related to the dissipation of the heat deposited by the fs-laser pulses, which give rise to permanent, heat-induced, changes of the magnetization of the nanostructured magnetostrictive elements.

Such issues with the dissipation of the laser-induced heating will have to be addressed, if the dynamics of the magnetization of the magnetostrictive nanostructures fabricated on top of the VO_2 thin films are going to be investigated. An alternative solution, not involving the illumination of the VO_2 thin film with the fs-laser, but still allowing for the excitation of the MIT at the timescales of the magnetization dynamics, would be to excite the MIT with an electric pulse, as shown in Refs. [135, 136]. In this case, electrode structures should be fabricated on top of the VO_2 thin films, with the nanostructured magnetostrictive elements positioned between the electrodes, as shown in Fig. 6.8(b). These experiments are scheduled to take place in one of the upcoming beamtimes in the second semester of 2015.

Appendix A

Image registration algorithms

In this appendix, the algorithm employed to correct the drift between successive PEEM images will be presented in detail.

An x-ray PEEM image is digitally stored as a matrix of $R \times R$ integer elements, being R the image resolution, where each element of the matrix is a pixel in the image, and where the typical x-ray PEEM image has a resolution of 512×512 or 1024×1024 pixels. As mentioned in Section 2.2.4, the drift correction between two x-ray PEEM images can be determined by calculating the discrete cross-correlation between the two images, given by the following relation [38]:

$$(f \star g_n)[l, m] = \sum_{j,k=0}^{R} f^*(j, k) g_n(j + l, k + m), \tag{A.1}$$

where $f(j, k)$ denotes the first, or *master* image, $g_n(j, k)$ the n-th drifted image, and $f^*(j, k)$ the complex conjugate of $f(j, k)$.

If one considers the discrete Fourier transforms $F(\nu, \omega)$ and $G_n(\nu, \omega)$ of the master and drifted images respectively, it is possible, by applying the cross-correlation theorem, to express Eq. (A.1) as follows:

$$(f \star g_n)[l, m] = \sum_{\nu,\omega} F^*(\nu, \omega) G(\nu, \omega) \exp\left(2\pi \mathrm{i} \frac{\nu l + \omega m}{R}\right), \tag{A.2}$$

where the discrete Fourier transform $F(\nu, \omega)$ of the function $f(j, k)$ is defined as follows:

$$F(\nu, \omega) = \sum_{j,k} \frac{f(j, k)}{R} \exp\left(-2\pi \mathrm{i} \frac{\nu j + \omega k}{R}\right). \tag{A.3}$$

The cross-correlation function defined in Eq. (A.1) only allows, due to the discretization, for the determination of drifts with a resolution down to a single pixel in the image. However, the magnitude of the drift between two consecutive images is generally not an integer multiple of a single pixel. Therefore, the drift correction using the cross-correlation calculated in Eq.

(A.1) is not completely precise, leading to a reduction of the image resolution if compared to a perfect drift correction.

It is, however, possible to carry out a sub-pixel drift correction by embedding the $R \times R$ image into a matrix of $kR \times kR$ elements, being k an integer number, where the single elements are determined by linear interpolation from the elements in the original image. The calculation of the cross-correlation function with Eq. (A.1) or Eq. (A.2) will then allow for the determination of the drift correction vector in expressed in $1/k$ pixel.

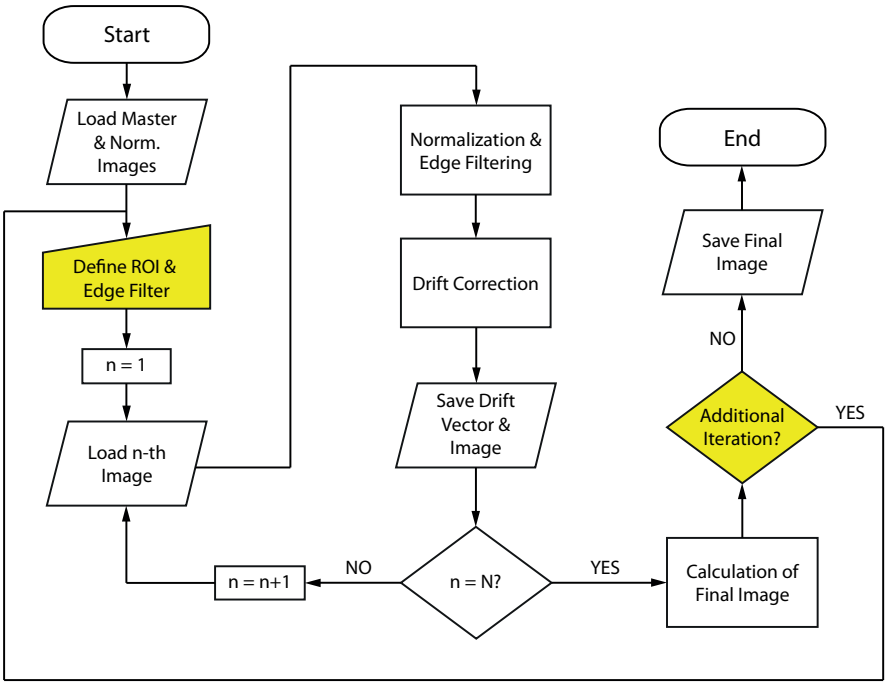

Figure A.1: Flowchart illustrating the operating principle of the Matlab script developed for the drift correction of $N + 1$ x-ray PEEM images.

While the approach described in the previous paragraph allows one to obtain a sub-pixel drift correction, it has been shown that this approach is computationally expensive, as it requires a non-efficient oversampling of the drifted $g_n(j,k)$ images. As calculated in Ref. [38], the computational complexity of the approach described in the previous paragraph is $\mathcal{O}\{R^2k(1+k)\log_2(Rk)\}$ that, due to the $k(1+k)$ dependence, becomes unfeasible as soon as the required sub-pixel accuracy k becomes large.

It is, however, possible to implement algorithms that allow for a more efficient computation of sub-pixel drift corrections. In particular, for the work presented in this thesis, the algorithm described in Ref. [38] has been implemented. The algorithm presented in Ref. [38] consists of a two step approach: in the first step of the algorithm, the cross-correlation between the master image $f(j,k)$ and the n-th drifted image $g_n(j,k)$ is calculated without any sub-pixel accuracy (i.e. $k = 1$). This first step allows for the estimation of the translation vector $\mathbf{v}_n$

within a one-pixel accuracy. At this point, being the value of the translation vector $\mathbf{v}_n$ known within a pixel of accuracy, the second step of the algorithm takes place. Here, the Fourier transform of the master and n-th drifted image is calculated and embedded into a matrix of $kR \times kR$ elements. Then, the cross-correlation of the two images is calculated according to Eq. (A.2), but the summation is carried out only for the (m, n) values within a 1.5×1.5 pixel region from the estimated values for $\mathbf{v}_n$. This process skips, therefore, the computationally expensive calculation of the sub-pixel cross-correlation in the entire $2kR + 1 \times 2kR + 1$ plane, thus reducing the computational complexity to $\mathcal{O}\{R^2 k^{1/2}\}$ [38].

The optimized image correction algorithm here described was implemented by the authors of Ref. [38] as a function for the commercial software Matlab. This function was implemented in a Matlab script (optimized for the reduction of RAM usage), which operates as schematically shown in Fig. A.1. This script was written as a user-friendly Matlab GUI (employing the GUIDE environment of the commercial Matlab software).

Appendix B

Electronic schematics of the PEEM voltage generator

In this appendix, the electronic schematics of the voltage generator unit employed for the experiments described in Chapter 4 will be presented.

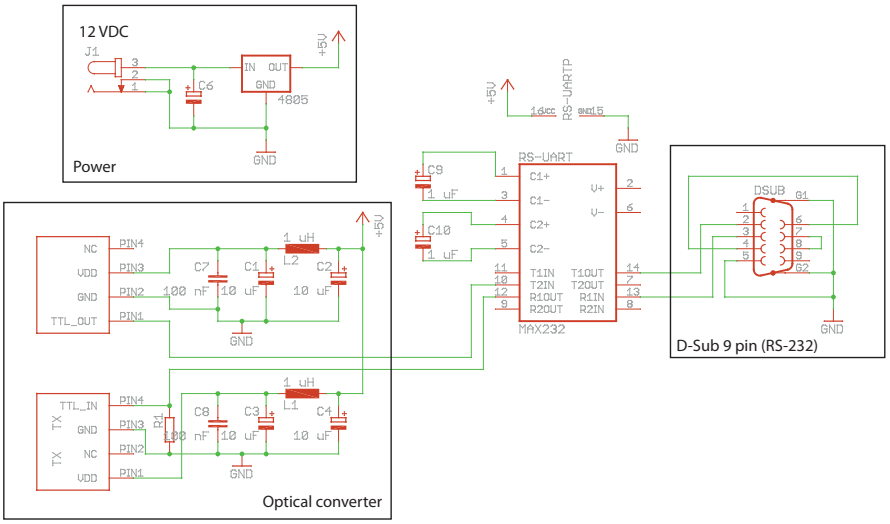

Figure B.1: Schematic of the RS-232 to optical converter used to communicate with the main unit inside the PEEM HV rack.

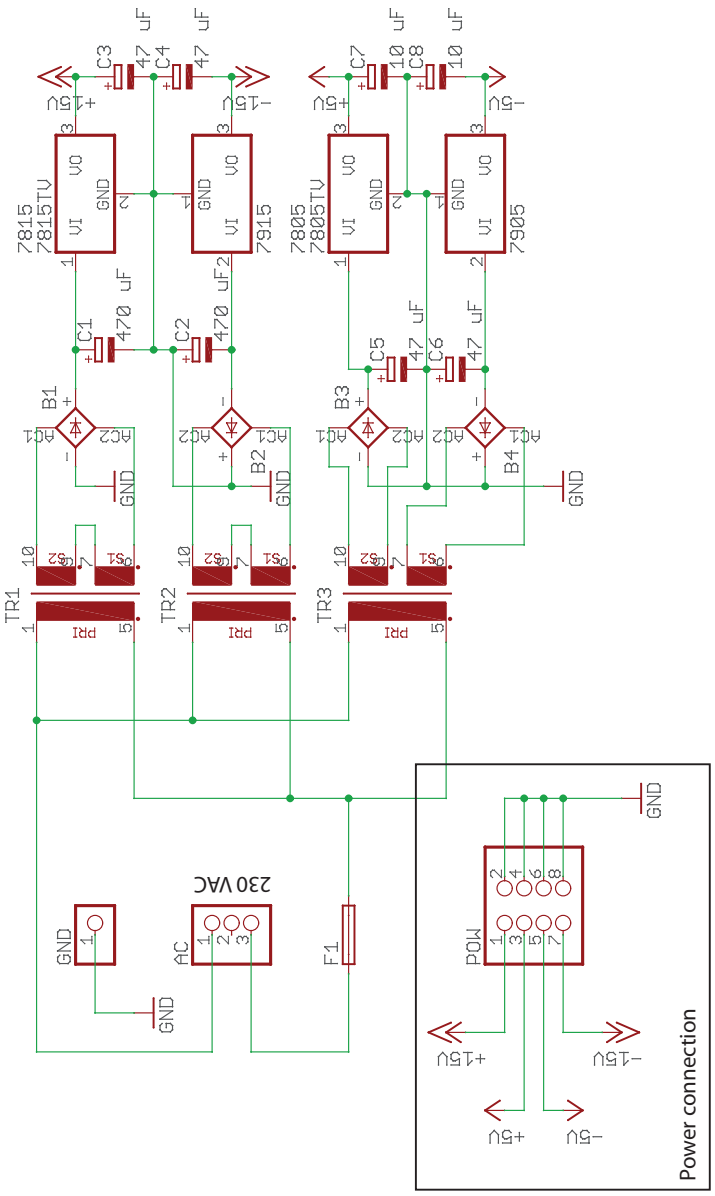

Figure B.2: Schematic of the power supply that powers the main unit.

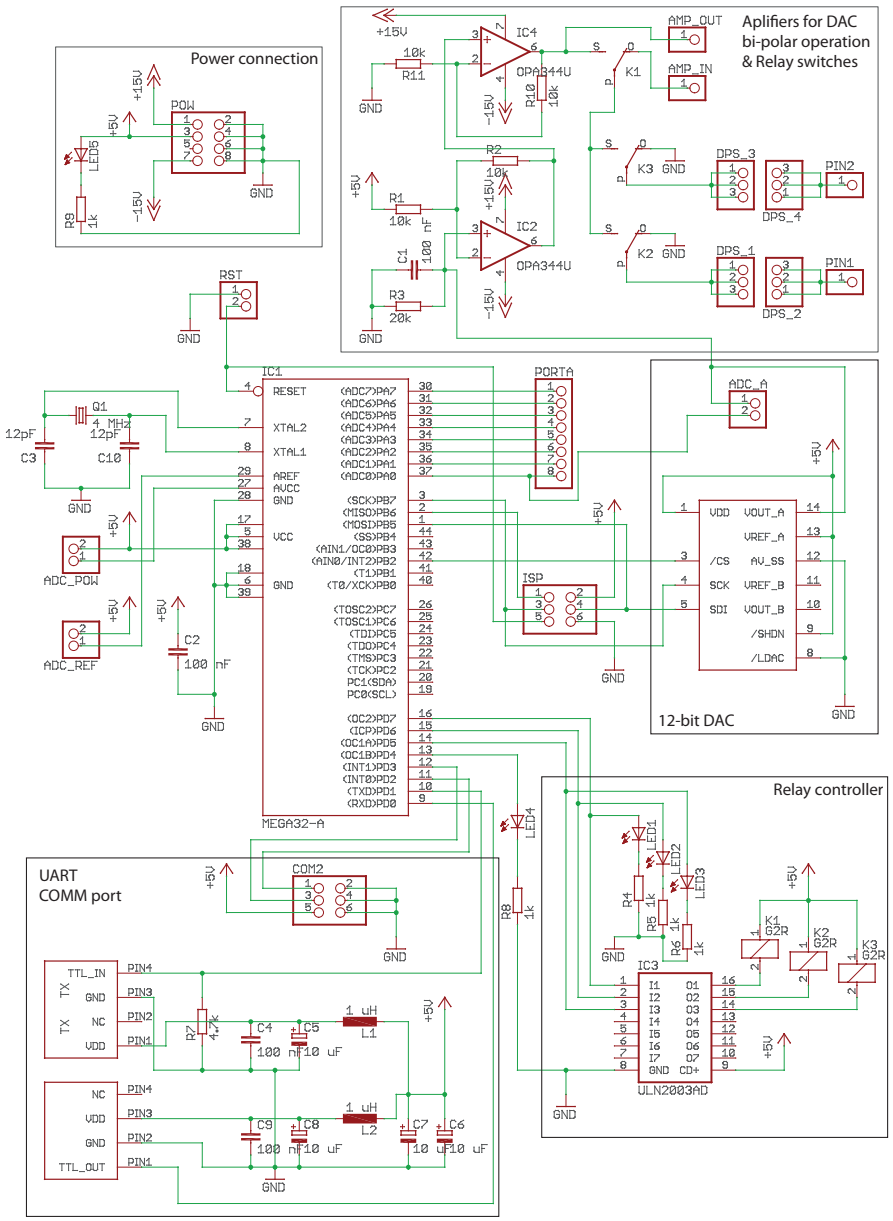

Figure B.3: Schematic of the main unit of the voltage generator. The microcontroller handles the communications with the support computer (via UART) and controls (via SPI) a 12-bit DAC.

Bibliography

[1] A. Moser et al., Journal of Physics D: Applied Physics **35**, R157 (2002).

[2] US Environmental Protection Agency, Report to Congress on Server and Data Center Energy Efficiency, 2007.

[3] S. Blundell, *Magnetism in Condensed Matter*, Oxford University Press, 2001.

[4] A. Aharoni, *Introduction to the Theory of Ferromagnetism*, Clarendon Press, 2000.

[5] J. M. D. Coey, *Magnetism and Magnetic Materials*, Cambridge University Press, 2010.

[6] W. Nolting and A. Ramakanth, *Quantum Theory of Magnetism*, Springer-Verlag, Berlin Heidelberg, 2009.

[7] H. A. Kramers, Physica **1**, 191 (1934).

[8] C. Zener, Physical Review **82**, 403 (1951).

[9] J. W. F. Brown, *Micromagnetism*, Krieger, New York, 1978.

[10] A. Brandlmaier et al., Physical Review B **77**, 104445 (2008).

[11] E. W. Lee, Reports on Progress in Physics **18**, 184 (1955).

[12] M. Weiler et al., New Journal of Physics **11**, 013021 (2009).

[13] A. Bur et al., Journal of Applied Physics **109**, 123903 (2011).

[14] E. Stoner and E. Wohlfarth, Philosophical Transactions of the Royal Society of London A **240**, 599 (1948).

[15] M. Gabor, T. Petrisor, Jr, C. Tiusan, M. Hehn, and T. Petrisor, Physical Review B **84**, 134413 (2011).

[16] T. Miyawaki et al., Journal of Applied Physics **114**, 073905 (2013).

[17] L. Landau and E. Lifshitz, Physikalische Zeitschrift der Sowjetunion **8**, 153 (1935).

[18] T. L. Gilbert, Physical Review **100**, 1243 (1955).

[19] G. Binasch, P. Grünberg, F. Sauernbach, and W. Zinn, Physical Review B **39**, 4828 (1989).

[20] L. Berger, Journal of Applied Physics **55**, 1954 (1984).

[21] O. Boulle, G. Malinowski, and M. Kläui, Materials Science and Engineering R **72**, 159 (2011).

[22] A. Thiaville, Y. Nakatani, J. Miltat, and Y. Suzuki, Europhysics Letters **69**, 990 (2005).

[23] A. Thiaville, Y. Nakatani, J. Miltat, and N. Vernier, Journal of Applied Physics **95**, 7049 (2004).

[24] Object Oriented Micromagnetic Framework (OOMMF), http://math.nist.gov/oommf.

[25] MicroMagnum, http://micromagnum.informatik.uni-hamburg.de.

[26] M. J. Donahue, Journal of Applied Physics **83**, 6491 (1998).

[27] M. Geissler and Y. Xia, Advanced Materials **16**, 1249 (2004).

[28] J. Rhensius et al., Applied Physics Letters **99**, 062508 (2011).

[29] R. Eisberg and R. Resnick, *Quantum Physics of Atoms, Molecules, Solids, Nuclei, and Particles*, John Wiley and Sons, 1985.

[30] M. Sacchi and J. Volgel, *Dichroism in x-ray Absorption in Magnetism and Synchrotron Radiation*, Springer-Verlag, Berlin Heidelberg, 2001.

[31] M. Eriksson, *Synchrotron Radiation*, Springer-Verlag, Berlin Heidelberg, 2006.

[32] G. B. Rybicki and A. P. Lightman, *Radiative Processes in Astrophysics*, John Wiely and Sons, 1979.

[33] F. A. Jenkins and H. E. White, *Fundamentals of Optics*, McGraw-Hill, 2001.

[34] H. Winick, G. Brown, K. Halbach, and J. Harris, Physics Today **34**, 50 (1981).

[35] E. Bauer, Journal of Electron Spectroscopy and Related Phenomena **185**, 314 (2012).

[36] R. M. Tromp et al., Ultramicroscopy **110**, 852 (2010).

[37] W. Telieps and E. Bauer, Ultramicroscopy **17**, 57 (1985).

[38] M. Guizar-Sicarios, S. T. Thurman, and J. R. Fienup, Optics Letters **33**, 156 (2008).

[39] R. Duda and P. Hart, *Pattern Classification and Scene Analysis*, John Wiley and Sons, 1973.

[40] J. F. Canny, IEEE Transactions on Pattern Analysis and Machine Intelligence **8**, 679 (1986).

[41] M. Buzzi et al., Physical Review Letters **111**, 027204 (2013).

[42] J. Kerr, The London, Edinburgh and Dublin Philosophical Magazine and Journal of Science **3**, 321 (1877).

[43] A. Hubert and R. Schäfer, *Magnetic Domains: The Analysis of Magnetic Microstructures*, Springer-Verlag, Berlin Heidelberg, 1998.

[44] P. Q. J. Nederpel and J. W. D. Martens, Review of Scientific Instruments **56**, 687 (1985).

[45] R. P. Feynman, *The Feynman Lectures on Physics*, Addison-Wesley, 1964.

[46] C. C. Robinson, Journal of the Optical Society of America **53**, 681 (1963).

[47] T. Graf, C. Felser, and S. S. P. Parkin, Progress in Solid State Chemistry **39**, 1 (2011).

[48] F. Heusler, W. Starck, and E. Haupt, Verhandlungen der DPG **5**, 220 (1903).

[49] F. Heusler, Verhandlungen der DPG **5**, 219 (1903).

[50] P. J. Webster and K. R. A. Ziebeck, *Landolt-Börnstein - group III condensed matter*, volume 19C, pages 75–184, Springer-Verlag, Berlin Heidelberg, 1988.

[51] C. Felser, G. H. Fecher, and B. Balke, Angewandte Chemie International Edition **46**, 668 (2007).

[52] K. Endo, H. Matsuda, K. Ooiwa, and K. Itoh, Journal of the Physical Society of Japan **64**, 2329 (1995).

[53] M. Jourdan et al., Nature Communications **5**, 3974 (2014).

[54] S. Trudel, O. Gaier, J. Hamrle, and B. Hillebrands, Journal of Physics D: Applied Physics **43**, 193001 (2010).

[55] K. Yamauchi, B. Sanyal, and S. Picozzi, Applied Physics Letters **91**, 062506 (2007).

[56] S. Ishida, S. Mizutani, S. Fujii, and S. Asano, Materials Transactions **47**, 31 (2006).

[57] S. Yoshimura et al., Journal of Applied Physics **103**, 07D716 (2008).

[58] A. Thiaville, Y. Nakatani, J. Miltat, and Y. Suzuki, Europhysics Letters **69**, 990 (2005).

[59] M. Kolbe et al., Physical Review B **86**, 024422 (2012).

[60] M. Hahn, G. Schönhense, E. A. Jorge, and M. Jourdan, Applied Physics Letters **98**, 232503 (2011).

[61] E. A. Jorge, *Band structure of Heusler Compounds studied by Photoemission and Tunneling Spectroscopy*, PhD thesis, Johannes-Gutenberg Universität Mainz, 2011.

[62] N. Fukatani, C. Shishikura, Y. Takeda, and H. Asano, Applied Physics Express **2**, 053001 (2009).

[63] O. Gaier et al., Journal of Applied Physics **103**, 103910 (2008).

[64] A. Ruiz-Calaforra et al., Journal of Physics D: Applied Physics **46**, 475001 (2013).

[65] U. Flechsig et al., AIP Conference Proceedings **1234**, 319 (2010).

[66] L. Le Guyader et al., Journal of Electron Spectroscopy and Related Phenomena **185**, 371 (2012).

[67] R. Cullity and C. D. Graham, *Introduction to Magnetic Materials*, Wiley-IEEE Press, New York, 2008.

[68] A. Locatelli, L. Aballe, T. Menteş, M. Kiskinova, and E. Bauer, Surface and Interface Analysis **38**, 1554 (2006).

[69] L. Aballe, M. Foerster, E. Pellegrin, J. Nicolas, and S. Ferrer, Journal of Synchrotron Radiation **22**, 745 (2015).

[70] J. Rothman et al., Physical Review Letters **86**, 1098 (2001).

[71] R. Yilgin et al., Japanese Journal of Applied Physics - Part 2 **46**, L205 (2007).

[72] S. S. P. Parkin, M. Hayashi, and L. Thomas, Science **320**, 190 (2008).

[73] C. A. F. Vaz et al., Applied Physics Letters **99**, 182510 (2011).

[74] I. Galankis, P. Mavropoulos, and P. H. Dederichs, Journal of Physics D: Applied Physics **39**, 765 (2006).

[75] M. Kläui et al., Applied Physics Letters **85**, 5637 (2004).

[76] M. Laufenberg et al., Applied Physics Letters **88**, 052507 (2006).

[77] S. Finizio et al., New Journal of Physics (2015), accepted for publication.

[78] N. A. Spaldin and M. Fiebig, Science **309**, 391 (2005).

[79] N. Hur et al., Nature **429**, 392 (2004).

[80] Y.-H. Chu, L. W. Martin, M. B. Holcomb, and R. Ramesh, Materials Today **10**, 16 (2007).

[81] Z. J. Huang, Y. Cao, Y. Y. Sun, Y. Y. Xue, and C. W. Chu, Physical Review B **56**, 2623 (1997).

[82] J. P. Joule, The London, Edinburgh and Dublin Philosophical Magazine and Journal of Science **30**, 76 (1847).

[83] E. M. Summers, T. A. Lograsso, and M. Wun-Fogle, Journal of Materials Science **42**, 9582 (2007).

[84] D. C. Jiles, Acta Materialia **51**, 5907 (2003).

[85] M. Fiebig, Journal of Physics D: Applied Physics **38**, R123 (2005).

[86] B. Noheda, D. E. Cox, G. Schirane, J. Gao, and Z.-G. Ye, Physical Review B **66**, 054104 (2002).

[87] T. Wu et al., Journal of Applied Physics **109**, 124101 (2011).

[88] K. Uchino, Ferroelectrics **151**, 321 (1994).

[89] K. Rabe, C. H. Ahn, and J.-M. Triscone, *Physics of Ferroelectrics: A Modern Perspective*, Springer-Verlag, Berlin Heidelberg, 2007.

[90] S. Finizio et al., SPIN **3**, 1340008 (2013).

[91] S. Finizio et al., Physical Review Applied **1**, 021001 (2014).

[92] J. L. Hockel, A. Bur, T. Wu, K. P. Wetzlar, and G. P. Carman, Applied Physics Letters **100**, 022401 (2012).

[93] F. Kronast et al., Surface and Interface Analysis **42**, 1532 (2010).

[94] J. E. Goldman, Physical Review **72**, 529 (1947).

[95] H. M. Ledbetter and R. P. Reed, Journal of Physical and Chemical Reference Data **2**, 531 (1973).

[96] W. Eerenstein, N. D. Mathur, and J. F. Scott, Nature **442**, 759 (2006).

[97] T. H. E. Lahtinen, K. J. A. Franke, and S. van Dijken, Scientific Reports **2**, 258 (2012).

[98] W. Eerenstein, M. Wiora, J. L. Prieto, J. F. Scott, and N. D. Mathur, Nature Materials **6**, 348 (2007).

[99] Y. Chen, T. Fitchorov, C. Vittoria, and V. G. Harris, Applied Physics Letters **97**, 052502 (2010).

[100] J. A. Katine, F. J. Albert, R. A. Buhrman, E. B. Myers, and D. C. Ralph, Physical Review Letters **84**, 3149 (2000).

[101] S. S. P. Parkin, M. Hayashi, and L. Thomas, Science **320**, 190 (2008).

[102] S. Fukami et al., Applied Physics Letters **95**, 232504 (2009).

[103] L. Heyne et al., Applied Physics Letters **96**, 032504 (2010).

[104] L. Heyne, *Manipulation of Magnetic Domain Walls and Vortices by Current Injection*, PhD thesis, Universität Konstanz, 2010.

[105] A. Biehler et al., Physical Review B **75**, 184427 (2007).

[106] M. Fonin et al., Journal of Applied Physics **109**, 07D315 (2011).

[107] J.-H. Park et al., Nature **320**, 794 (1998).

[108] R. Reeve et al., Applied Physics Letters **102**, 122407 (2013).

[109] J. Heidler et al., Journal of Applied Physics **112**, 103921 (2012).

[110] V. Moschnyaga et al., Applied Physics Letters **74**, 2842 (1999).

[111] S. Finizio et al., Journal of Physics: Condensed Matter **26**, 456003 (2014).

[112] M. Foerster et al., Applied Physics Letters **104**, 072410 (2014).

[113] D. Weber, R. Vofely, Y. Chen, Y. Mourzina, and U. Poppe, Thin Solid Films **30**, 43 (2013).

[114] M. Laufenberg et al., Physical Review Letters **97**, 046602 (2006).

[115] L. Heyne, M. Kläui, J. Rhensius, L. Le Guyader, and F. Nolting, Review of Scientific Instruments **81**, 113707 (2010).

[116] M. Kläui, Journal of Physics: Condensed Matter **20**, 313001 (2008).

[117] O. Boulle et al., Physical Review Letters **101**, 216601 (2008).

[118] A. Monsen, *On the properties of $La_{0.7}Sr_{0.3}MnO_3$ thin films on (001) $SrTiO_3$ substrates*, PhD thesis, Norwegian University of Science and Technology, 2013.

[119] R. M. Michael and M. Donahuhe, IEEE Transactions on Magnetism **33**, 4167 (1997).

[120] Y. Nakatani, A. Thiaville, and J. Miltat, Journal of Magnetism and Magnetic Materials **290**, 750 (2005).

[121] A. Aharoni, Journal of Applied Physics **83**, 3432 (1998).

[122] D. E. Parkes et al., Applied Physics Letters **105**, 062405 (2014).

[123] J. Walowski et al., Journal of Physics D: Applied Physics **41**, 164016 (2008).

[124] G. M. Wysin, Physical Review B **54**, 15156 (1996).

[125] D. L. Huber, Physical Review B **26**, 3758 (1982).

[126] J. Rhensius et al., Physical Review Letters **104**, 067201 (2010).

[127] A. Cavalleri et al., Physical Review Letters **87**, 237401 (2001).

[128] H. Wen et al., Physical Review B **88**, 165424 (2013).

[129] P. Baum, D. S. Yang, and A. H. Zewail, Science **318**, 788 (2007).

[130] M. M. Quazilbash et al., Science **318**, 1750 (2007).

[131] M. Imada, A. Fujimori, and Y. Tokura, Reviews of Modern Physics **70**, 1039 (1998).

[132] B. Viswanath, C. Ko, and S. Ramanathan, Scripta Materialia **64**, 490 (2011).

[133] J. de la Venta, S. Wang, J. Ramirez, and I. Schuller, Applied Physics Letters **102**, 122404 (2013).

[134] N. B. Aetukuri et al., Nature Physics **9**, 661 (2013).

[135] Z. Yang, C. Ko, and S. Ramanathan, Annual Review of Materials Research **41**, 337 (2011).

[136] B. G. Chae, H. T. Kim, D. H. Youn, and K. Y. Kang, Physica B **369**, 76 (2005).

Acknowledgments

Aus Datenschutzgründen entfernt / Removed for means of data privacy.

Aus Datenschutzgründen entfernt / Removed for means of data privacy.

Curriculum Vitae

Aus Datenschutzgründen entfernt / Removed due to data privacy.

Aus Datenschutzgründen entfernt / Removed due to data privacy.

Publications List

- **S. Finizio**, A. Kronenberg, M. Vafaee, M. Foerster, K. Litzius, T. O. Menteş, L. Aballe, M. Jourdan, and M. Kläui, *Magnetic configurations in nanostructured Co_2MnGa thin film elements*, New Journal of Physics, *accepted for publication*, (2015)

- **S. Finizio**, M. Foerster, B. Krüger, C. A. F. Vaz, T. Miyawaki, M.-A. Mawass, L. Peña, L. Méchin, S. Hühn, V. Moshnyaga, F. Büttner, A. Bisig, L. Le Guyader, S. El Moussaoui, S. Valencia, F. Kronast, S. Eisebitt, and M. Kläui, *Domain wall transformations and hopping in $La_{0.7}Sr_{0.3}MnO_3$ nanostructures imaged with high resolution x-ray magnetic microscopy*, Journal of Physics: Condensed Matter **26**, 456003 (2014)

- C. Mix, **S. Finizio**, M. Kläui, and G. Jakob, *Conductance control at the $LaAlO_3$/ $SrTiO_3$-interface by a multiferroic $BiFeO_3$ ad-layer*, Applied Physics Letters **104**, 262903 (2014)

- C. Mix, **S. Finizio**, M. Buzzi, F. Kronast, F. Nolting, G. Jakob, and M. Kläui, *Direct observation of temperature dependent magnetic domain structure of the multiferroic $La_{0.66}Sr_{0.34}MnO_3/BiFeO_3$ bilayer system by x-ray linear dichroism- and x-ray magnetic circular dichroism photoemission electron microscopy*, Journal of Applied Physics **115**, 193901 (2014)

- **S. Finizio**, M. Foerster, M. Buzzi, B. Krüger, M. Jourdan, C. A. F. Vaz, J. Hockel, T. Miyawaki, A. Tkach, S. Valencia, F. Kronast, G. P. Carman, F. Nolting, and M. Kläui, *Magnetic anisotropy engineering in thin film Ni nanostructures by magnetoelastic coupling*, Physical Review Applied **1**, 021001 (2014)

- M. Foerster, L. Peña, C. A. F. Vaz, J. Heinen, **S. Finizio**, T. Schulz, A. Bisig, F. Büttner, S. Eisebitt, L. Méchin, S. Hühn, V. Moshnyaga, and M. Kläui, *Efficient spin transfer torque in $La_{2/3}Sr_{1/3}MnO_3$ nanostructures*, Applied Physics Letters **104**, 072410 (2014)

- **S. Finizio**, M. Foerster, C. A. F. Vaz, M. Buzzi, J. Hockel, T. Miyawaki, C. Mix, M.-A. Mawass, A. Tkach, S. Valencia, F. Kronast, F. Nolting, G. P. Carman and M. Kläui,

Electrical-field control of magnetism mediated by strain in Ni nanostructures fabricated on pre-poled PMN-PT (011), SPIN **3**, 1340008 (2013)

- T. Miyawaki, M. Foerster, **S. Finizio**, C. A. F. Vaz, M.-A. Mawass, K. Inagaki, N. Fukatami, L. Le Guyader, F. Nolting, K. Ueda, H. Asano, and M. Kläui, *The effect of magnetocrystalline anisotropy on the domain structure of patterned Fe_2CrSi Heusler alloy thin films*, Journal of Applied Physics **114**, 073905 (2013)

- F. Büttner, C. Moutafis, A. Bisig, P. Wohlhüter, C. M. Günther, J. Mohanty, J. Geilhufe, M. Schneider, C. v. Korff Schmising, S. Schaffert, B. Pfau, M. Hantschmann, M. Riemeier, M. Emmel, **S. Finizio**, G. Jakob, M. Weigand, J. Rhensius, J. H. Franken, R. Lavrijisen, H. J. M. Swagten, H. Stoll, S. Eisebitt, and M. Kläui, *Magnetic states in low-pinning high-anisotropy material nanostructures suitable for dynamic imaging*, Physical Review B **87**, 134422 (2013)

Eidesstattliche Erklärung

Hiermit erkläre ich an Eides statt, dass ich meine Dissertation selbständig und ohne fremde Hilfe verfasst und keine anderen als die von mir angegebenen Quellen und Hilfsmittel zur Erstellung meiner Dissertation verwendet habe. Die Arbeit ist in vorliegender oder ähnlicher Form bei keiner anderen Prüfungsbehörde zur Erlangung eines Doktorgrades eingereicht worden.

Mainz, den

Simone Finizio